Karlsruhe Institute of Technology

Andreas Wickberg

On Second-Harmonic Generation in Nanolaminates and 3D Nanolaminated Photonic Crystals

2019
Dissertation

On Second-Harmonic Generation in Nanolaminates and 3D Nanolaminated Photonic Crystals

Zur Erlangung des akademischen Grades eines
DOKTORS DER NATURWISSENSCHAFTEN
von der KIT-Fakultät für Physik des
Karlsruher Instituts für Technologie (KIT)

genehmigte

DISSERTATION

von

M.Sc. Andreas Wickberg
geboren in Sosnowoborsk (Russland)

Tag der mündlichen Prüfung: 01.02.2019
Referent: Prof. Dr. Martin Wegener
Korreferent: Prof. Dr. Carsten Rockstuhl

Contents

Publications

Scientific Journals

Parts of the content of this thesis have already been published in peer-reviewed scientific journals:

- A. Wickberg*, C. Kieninger*, C. Sürgers, S. Schlabach, X. Mu, C. Koos, and M. Wegener, "Second-Harmonic Generation from ZnO/Al_2O_3 Nanolaminate Optical Metamaterials Grown by Atomic-Layer Deposition", *Adv. Opt. Mater.* **4**, 1203 (2016)
- A. Wickberg, A. Abass, H.-H. Hsiao, C. Rockstuhl, and M. Wegener, "Second-Harmonic Generation by 3D Laminate Metacrystals" (invited article), *Adv. Opt. Mater.*, submitted

Presentations

Parts of the content of this thesis have already been presented at scientific conferences (only own presentations):

- A. Wickberg*, C. Kieninger*, C. Sürgers, C. Koos, and M. Wegener, "Second-Harmonic Generation from ZnO/Al_2O_3 Laminate Optical Metamaterials Grown by Atomic-Layer Deposition", CLEO 2016, San José, CA, USA, June 2016

* The authors contributed equally to this work.

Other Publications and Presentations

Scientific publications by the author that are not part ot this thesis:

- A. Wickberg, J. B. Mueller, Y. J. Mange, J. Fischer, T. Nann, and M. Wegener, "Three-Dimensional Micro-Printing of Temperature Sensors Based on Up-Conversion Luminescence", *Appl. Phys. Lett.* **106**, 133103 (2015)
- H.-H. Hsiao, A. Abass, J. Fischer, R. Alaee, A. Wickberg, M. Wegener, and C. Rockstuhl, "Enhancement of Second-Harmonic Generation in Nonlinear Nanolaminate Metamaterials by Nanophotonic Resonances", *Opt. Express* **24**, 9651 (2016)
- A. Hermans, C. Kieninger, K. Koskinen, A. Wickberg, E. Solano, J. Dendooven, M. Kauranen, S. Clemmen, M. Wegener, C. Koos, and R. Baets, "On the Determination of $\chi^{(2)}$ in Thin Films: A Comparison of One-Beam Second-Harmonic Generation Measurement Methodologies", *Sci. Rep.* **7**, 44581 (2017)
- V. S. Asadchy*, A. Wickberg*, A. Díaz-Rubio, and M. Wegener, "Eliminating Scattering Loss in Anomalously Reflecting Optical Metasurfaces", *ACS Photonics* **4**, 1264 (2017)
- D. Gräfe, A. Wickberg, M. M. Zieger, M. Wegener, E. Blasco, and C. Barner-Kowollik, "Adding Chemically Selective Subtraction to Multi-Material 3D Additive Manufacturing", *Nat. Commun.* **9**, 2788 (2018)

Presentations at scientific conferences that cover topics not part ot this thesis (only own presentations):

- A. Wickberg, J. B. Mueller, Y. J. Mange, T. Nann, and M. Wegener, "3D Micro-Printing of Optical Temperature Probes", SPIE Photonics West, San Francisco, CA, USA, February 2015
- V. S. Asadchy*, A. Wickberg*, A. Díaz-Rubio, M. Wegener, and S. A. Tretyakov, "Nonlocal Metasurfaces Enable Perfect Anomalous Reflection", SPIE Optics+Photonics, San Diego, CA, USA, August 2017

Chapter 1

1 Introduction

The interactions between light and matter are crucial for the existence of life. Afterall, these interactions are fundamental to photosynthesis, the arguably most important biological process on earth [1]. The way we perceive the world through our eyes is another example for the interplay of light and matter. Light is emitted from luminous objects as a superposition of electromagnetic waves at different frequencies. These light waves interact with matter and can be transmitted, reflected or absorbed. Eventually, the remnants of the initially emitted light reach our eyes and are absorbed by spectrally-sensitive retinal cells that initiate a series of steps resulting in a signal to our brain. The majority of the aforementioned light-matter interactions are reasonably described by what is called linear optics. It describes most of the optical phenomena we observe in every day life and is based on the assumption of a material response, given in terms of its polarization, that is linear in the interacting electric field strength.

The regime covering the higher order correction terms to this linear approximation is consequently called nonlinear optics. Due to the typically high electrical field strength necessary to observe nonlinear optical phenomena, these kind of light-matter interactions were not observed until the first experimental realization of a laser in 1960 [2, 3]. Nowadays, the use of nonlinear optical effects is manifold reaching from the generation of short laser pulses, over laser machining and medical applications, to telecommunications [4]. The focus in this thesis lies on second-order nonlinear effects that are a key ingredient of optical parametric oscillators and fast electro-optic modulators used for the generation of frequencies that are not accessible by other

methods and at the interface between electrical and optical data transfer, respectively. Another prominent example of a second-order nonlinear effect is second-harmonic generation used, for example, to convert infrared to visible radiation in green laser pointers. Throughout this thesis, we will measure the generated second-harmonic signal to characterize the second-order nonlinear response of our samples.

It is quite common to use bulk single crystals to enable a high efficiency of nonlinear effects. Unfortunately, they lack the flexibility necessary for compact optical integration, *e.g.*, on nanophotonic chips. Here, thin films deposited by techniques that are compatible with complementary metal-oxide-semiconductor processing are a promising alternative and have been demonstrated to give good results in terms of both their linear and nonlinear optical properties. Among the available fabrication methods, the focus in this work will lie on atomic-layer deposition as it allows for the conformal deposition of a variety of materials with a precise control of the thickness down to an atomic monolayer. The effective film properties depend strongly on the growth mode and circumstances. This is especially relevant for second-order nonlinear films that rely on a lack of inversion symmetry to show a non-vanishing effect. Based on these considerations it becomes clear that it is necessary to control the structure of the thin films in order to optimize their effective optical performance. For fixed deposition conditions one can use thin, alternating layers made from different materials to achieve this goal. These so-called nanolaminate have been demonstrated to allow for tuning of the effective optical and mechanical material properties. In this work, our goal is to apply this concept to ZnO/Al_2O_3 stacks grown by atomic-layer deposition and, thereby, tailor the structural properties of ZnO for an optimized effective second-order nonlinear response.

The overall efficiency of nonlinear interactions is often limited by the short interaction length or a non-zero phase mismatch at the involved frequencies. In nonlinear single crystals these issues are, usually, tackled by increasing the intensity of the interacting waves and exploiting birefringence in the used material. Nevertheless, there are situations where these approaches fail due to a low damage threshold or a lack of birefringence, respectively.

Conformally deposited thin films open a new route to deal with these limitations due to the fact that they grow with equal thickness on all exposed surfaces independent of their orientation. Therefore, depositing second-order nonlinear nanolaminates on scaffolds or templates, gives an additional degree of freedom in terms of the spatial arrangement and orientation of the nonlinear properties in the resulting structure. In principle, one can choose arbitrary templates tailored to meet the needs of the specific process and application. We will demonstrate the approach by using 3D photonic crystals as they allow for an unprecedented control over the flow of light and, hence, can also be utilized to enhance nonlinear processes by reinforcing light-matter interactions or providing novel pathways for phase matching [5]. The templates are "printed"using 3D direct laser writing allowing for a fast and easy fabrication of nearly arbitrary 3D structures with a resolution of a few-hundreds of nanometers.

The conformal deposition of second-order nonlinear nanolaminates on 3D photonic crystals allows us to make use of the best from the two worlds. The nanolaminate provides the second-order nonlinearity that is usually not available in structures fabricated by means of 3D direct laser writing and, thereby, enables a variety of new applications. The 3D photonic crystal template enforces a spatial distribution of the nanolaminate properties and, therefore, allows for tuning of nonlinear interactions to result in efficiencies that are not achievable in plain films. Additionally, one benefits from the increased amount of deposited material due to the simultaneous growth on all surfaces. In the scope of this work we will fabricate and study these so-called 3D nanolaminated photonic crystals. The goal is to demonstrate the interplay of the two systems that results in an enhancement of second-order nonlinear light-matter interactions.

Outline of This Thesis

In Chapter 2 the fundamentals necessary for a thorough understanding of the results obtained in the scope of this thesis are presented. After introducing the inhomogeneous wave equation, the interaction of light and matter will be introduced in terms of the material response. A general overview over the effects that arise when this response becomes nonlinear is given and the inhomogeneous equation is solved for examples in both the linear and nonlinear regime. Chapter 2 is concluded by introducing the most important concepts and characteristics of photonic crystals, dielectric waveguides, and metamaterials. Where applicable special attention will be given to nonlinear properties and interactions in these structures.

Following this introduction, the methods used for both fabrication and analysis of the novel second-order nonlinear materials and structures will be described in Chapter 3. First, the basic mechanisms and setups used for the fabrication by means of atomic-layer deposition and 3D direct laser writing will be presented. Additionally, the features that deviate from the standard approaches and are of special interest are highlighted. Next, the methods and setups used to study both the linear and nonlinear optical properties of the fabricated samples are introduced. Finally, the basics of X-ray diffraction and the finite element method with their respective implementation are illustrated as these methods are used to supplement the results from optical measurements.

Chapter 4 covers design, fabrication, and results on both second-order nonlinear nanolaminates and 3D nanolaminated photonic crystals. The effects and mechanism leading to the observed behavior are described and the developed understanding serves as a starting point to discuss possible improvements. The thesis is summarized and concluded in Chapter 5.

Chapter 2

2 Fundamentals

In this chapter, the basics necessary to understand the calculations and analogies used in the remainder of this thesis are summarized. Starting from Maxwell's equations, the inhomogeneous wave equation governing the generation and propagation of electromagnetic waves is derived. To solve this equation in matter, the material response that becomes nonlinear for strong electromagnetic fields has to be discussed. A summary of important second- and third-order nonlinear effects, some of them exploited extensively in the remainder of this thesis, follows. Subsequently, the inhomogeneous wave equation is solved for two exemplary cases that serve to illustrate the linear and nonlinear interaction of light and matter. The derivations follow the text book by Butcher and Cotter [6]. Finally, the fundamentals of photonic crystals, dielectric waveguides, and metamaterials are discussed. Special attention is payed to the peculiarities of nonlinear interactions in both photonic crystals and metamaterials.

2.1 The Inhomogeneous Wave Equation

Studying the interaction of light and matter one usually starts at Maxwell's equations. In their microscopic form, they describe how the electric field strength, $\boldsymbol{E}$, is generated from the total charge density, ρ_{tot}, and variations of the magnetic flux density, $\boldsymbol{B}$, in time (boldface is used for vectors and tensors) [7]. The magnetic flux density, $\boldsymbol{B}$, in turn, depends on the total current density, $\boldsymbol{J}_{\mathrm{tot}}$, and variations of, $\boldsymbol{E}$, in time. To avoid having to consider each charge and current individually, one introduces auxiliary fields in the macroscopic formulation of Maxwell's equations that incorporate material contributions by means of the electric displacement, $\boldsymbol{D}$, and the magnetic field strength, $\boldsymbol{H}$. Using the international system of units (SI) these equations read:

$$\begin{aligned} \nabla \cdot \boldsymbol{D}(\boldsymbol{r},t) &= \rho_{\mathrm{f}}(\boldsymbol{r},t) \\ \nabla \cdot \boldsymbol{B}(\boldsymbol{r},t) &= 0 \\ \nabla \times \boldsymbol{E}(\boldsymbol{r},t) &= -\tfrac{\partial}{\partial t}\boldsymbol{B}(\boldsymbol{r},t) \\ \nabla \times \boldsymbol{H}(\boldsymbol{r},t) &= \boldsymbol{J}_{\mathrm{f}}(\boldsymbol{r},t) + \tfrac{\partial}{\partial t}\boldsymbol{D}(\boldsymbol{r},t) \end{aligned} \tag{2.1}$$

with the free charge and current density, ρ_{f} and $\boldsymbol{J}_{\mathrm{f}}$, respectively [8]. The information on the distribution of bound charges and both bound and polarization currents is averaged over a suitable region that is usually larger than the inter-atomic distance but smaller than the wavelength [9]. The constituent equations relate the individual electric quantities through the polarization, $\boldsymbol{P}$, and the magnetic quantities through the magnetization, $\boldsymbol{M}$,

$$\begin{aligned} \boldsymbol{D}(\boldsymbol{r},t) &= \varepsilon_0 \boldsymbol{E}(\boldsymbol{r},t) + \boldsymbol{P}(\boldsymbol{r},t) \\ \boldsymbol{B}(\boldsymbol{r},t) &= \mu_0 \boldsymbol{H}(\boldsymbol{r},t) + \boldsymbol{M}(\boldsymbol{r},t) \end{aligned} \tag{2.2}$$

with the vacuum permittivity ε_0 and the vacuum permeability μ_0. In general, the material response described by polarization, $\boldsymbol{P}$, and magnetization, $\boldsymbol{M}$, is a function of both the electric field strength, $\boldsymbol{E}$, and the magnetic flux density, $\boldsymbol{B}$. Nevertheless, for the material systems studied in the scope of this work it is sufficient to look at a purely electric dependency of the polarization: $\boldsymbol{P}(\boldsymbol{r},t) = \boldsymbol{P}[\boldsymbol{E}]$ [10]. Furthermore, all materials are considered to be nonmagnetic and to contain no free charges leading to $\boldsymbol{M} = 0$ and

$\rho_f = 0$, respectively [6]. Under these assumptions the inhomogeneous wave equation governing the electric field strength, $\boldsymbol{E}$, can be derived by combining Equations 2.1 and 2.2. Using the fact that $c_0^2 = 1/(\varepsilon_0 \mu_0)$ it reads

$$\nabla \times \nabla \times \boldsymbol{E}(\boldsymbol{r}, t) + \frac{1}{c^2} \frac{\partial^2}{\partial t^2} \boldsymbol{E}(\boldsymbol{r}, t) = -\mu_0 \frac{\partial}{\partial t} \left(\boldsymbol{J}_f(\boldsymbol{r}, t) + \frac{\partial}{\partial t} \boldsymbol{P}(\boldsymbol{r}, t) \right). \tag{2.3}$$

The solution to the homogeneous part of Equation 2.3 gives waves propagating at the vacuum speed of light, c_0. The source term on the right-hand side of the equation represents the modifications to this propagation caused by the interaction between light and matter. It is instructive to note that the driving term is defined by the sum of the time derivatives of both the time derivative of the polarization, $\boldsymbol{P}$, and the free current density, $\boldsymbol{J}_f$. For practical reasons this aspect will be exploited in the numerical calculations to define the nonlinear polarization at the second-harmonic frequency. For all other purposes $\boldsymbol{J}_f$ is equal to zero in the studied systems.

For many problems, *e. g.*, when considering dispersive media or monochromatic waves, it is beneficial to solve the wave equation in frequency domain. Introducing the Fourier transform for $\boldsymbol{E}(\boldsymbol{r}, t)$ and $\boldsymbol{P}(\boldsymbol{r}, t)$ in Equation 2.3 and looking at an individual frequency, ω, one obtains:

$$\nabla \times \nabla \times \tilde{\boldsymbol{E}}(\boldsymbol{r}, \omega) - \frac{\omega^2}{c_0^2} \tilde{\boldsymbol{E}}(\boldsymbol{r}, \omega) = \mu_0 \omega^2 \tilde{\boldsymbol{P}}(\boldsymbol{r}, \omega). \tag{2.4}$$

A tilde is used to denote the Fourier transform of the corresponding quantity, *e. g.*, $\tilde{\boldsymbol{E}}(\boldsymbol{r}, \omega)$ is the Fourier transform of the vector field $\boldsymbol{E}(\boldsymbol{r}, t)$.

2.2 The Material Response

Having derived the inhomogeneous wave equation in the previous section, the form of the driving term on the right-hand side has to be specified to be able to solve this equation in time or frequency domain. The constitutive relation that will be introduced in the following establishes the missing link between the polarization, $\boldsymbol{P}$, and the electric field strength, $\boldsymbol{E}$.

The origin of the constitutive relation can be understood by considering a simple model of a dielectric built of electrons and atoms with a restoring

force binding them together. When an oscillating electric field is applied negatively charged electrons and positively charged atoms are displaced in opposite directions from their equilibrium position. They form oscillating electric dipole moments that manifest themselves in the polarization, $\boldsymbol{P}$. For a weak electric field the displacement is small and the potential energy is harmonic leading to a linear restoring force and a polarization that is proportional to the applied electric field strength. This is no longer true for applied fields approaching the atomic electric field strength that result in large displacements from equilibrium [11]. Anharmonic effects come into play and both the restoring force and the relation between the polarization, $\boldsymbol{P}$, and the electric field strength, $\boldsymbol{E}$, become nonlinear. The necessity for large electric field strengths is also the reason that nonlinear optical effects cannot be observed that easily in every day life and that the observation of the majority of these effects occurred only after the experimental realization of the first laser in 1960 [2, 3].

The exact dependence of the polarization on the electric field strength is usually unknown. Therefore, a widely used approach is to expand the polarization in a power series of the electric field strength. In time domain this expansion reads [6]:

$$\boldsymbol{P}(\boldsymbol{r},t) = \boldsymbol{P}^{(0)}(\boldsymbol{r},t) + \boldsymbol{P}^{(1)}(\boldsymbol{r},t) + \boldsymbol{P}^{(2)}(\boldsymbol{r},t) + \ldots + \boldsymbol{P}^{(n)}(\boldsymbol{r},t) + \ldots, \tag{2.5}$$

were $\boldsymbol{P}^{(n)}(\boldsymbol{r},t)$ is proportional to the n-th power of the electric field strength. The first term in the expansion gives a constant field-independent polarization and will be neglected in the remainder of this thesis. The linear polarization, $\boldsymbol{P}^{(1)}(\boldsymbol{r},t)$, is the basis for linear optics and covers most of the optical phenomena encountered in everyday life. The further discussion will be limited to a homogeneous medium with a purely local response, neglecting interactions between individual polarizable entities [12]. With this assumption the polarization at a given point is completely determined by the electric field strength at the same point. Additionally, the medium is supposed to be time-invariant so that the response does not depend on the absolute value of the time, t. Using the Einstein summation convention the

μ-component of the linear polarization in time domain can be written as

$$P_\mu^{(1)}(\boldsymbol{r},t) = \varepsilon_0 \int_{-\infty}^{+\infty} \mathrm{d}\tau \; R_{\mu\alpha}^{(1)}(\tau) E_\alpha(\boldsymbol{r}, t-\tau). \tag{2.6}$$

The way the components of the electric field strength, $\boldsymbol{E}$, couple to different components of the induced polarization, $\boldsymbol{P}$, is described by the linear polarization response function, $\boldsymbol{R}^{(1)}$. To ensure causality, this rank two tensor is zero for negative arguments. Additionally it has to be real due to the fact that both electric field strength, $\boldsymbol{E}$, and polarization, $\boldsymbol{P}$, are real. The frequency domain counterpart to the linear response function is the linear susceptibility that is, in general, complex and defined as

$$\chi_{\mu\alpha}^{(1)}(-\omega_\sigma;\omega) = \int_{-\infty}^{+\infty} \mathrm{d}\tau \; R_{\mu\alpha}^{(1)}(\tau) e^{i\omega\tau}. \tag{2.7}$$

The arguments in the brackets describe an additional requirement imposed on the interacting frequencies, that is, that the sum of all frequencies to the right of the semicolon has to be equal to ω_σ. In the simple linear case this leads to $\omega_\sigma = \omega$. The Fourier transform of the linear polarization is determined by rewriting the electric field strength and the polarization in Equation 2.6 in terms of their Fourier transforms in combination with Equation 2.7:

$$\tilde{P}_\mu^{(1)}(\boldsymbol{r},\omega) = \varepsilon_0 \chi_{\mu\alpha}^{(1)}(-\omega_\sigma;\omega) \tilde{E}_\alpha(\boldsymbol{r},\omega). \tag{2.8}$$

At this point the inhomogeneous wave equation in frequency domain can be solved given a specific linear susceptibility (see Section 2.4).

Following the same approach for the higher order terms in the polarization power series (see Equation 2.5), the respective response functions and susceptibilities can be derived. The Fourier transform of the n-th order polarization is given by [6]

$$\begin{aligned}\tilde{P}_\mu^{(n)}(\boldsymbol{r},\omega) = \varepsilon_0 \int_{-\infty}^{\infty} \mathrm{d}\omega_1 \ldots \int_{-\infty}^{\infty} \mathrm{d}\omega_n \; \chi_{\mu\alpha_1\ldots\alpha_n}^{(n)}(-\omega_\sigma;\omega_1,\ldots,\omega_n) \\ \times \tilde{E}_{\alpha_1}(\boldsymbol{r},\omega_1)\ldots\tilde{E}_{\alpha_n}(\boldsymbol{r},\omega_n)\,\delta(\omega-\omega_\sigma).\end{aligned} \tag{2.9}$$

The tensor $\chi^{(n)}$ of rank $n+1$ is the complex n-th order susceptibility and as before the individual frequencies, ω_j, must fulfill

$$\omega_\sigma = \sum_{j=1}^{n} \omega_j. \tag{2.10}$$

For most of the applications monochromatic waves at specific frequencies, ω', are used. In that case, the electric field strength can be expressed as

$$\boldsymbol{E}(\boldsymbol{r},t) = \tfrac{1}{2} \sum_{\omega' \geq 0} \left(\tilde{\boldsymbol{E}}_{\omega'}(\boldsymbol{r}) e^{-i\omega' t} + \text{c.c.} \right), \tag{2.11}$$

where $\tilde{\boldsymbol{E}}_{\omega'}$ is the monochromatic-wave amplitude at frequency ω'.

The focus in this work lies on materials and structures that have a non-zero second-order susceptibility and, more specifically, on second-harmonic generation in these systems. Contributions of higher orders will be neglected as they tend to be small for a proper choice of excitation conditions [11]. The monochromatic-wave amplitude of the second-order polarization at frequency $\omega_\sigma = 2\omega$ in the degenerate case of $\omega = \omega_1 = \omega_2$ is

$$\left[\tilde{P}^{(2)}_{2\omega}(\boldsymbol{r}) \right]_\mu = \tfrac{1}{2} \varepsilon_0 \chi^{(2)}_{\mu\alpha_1\alpha_2}(-2\omega;\omega,\omega) \left[\tilde{E}_\omega(\boldsymbol{r}) \right]_{\alpha_1} \left[\tilde{E}_\omega(\boldsymbol{r}) \right]_{\alpha_2}. \tag{2.12}$$

To determine $\tilde{\boldsymbol{P}}^{(2)}_{2\omega}$ all one has to know is the monochromatic-wave amplitude of the electric field strength at the fundamental frequency, $\tilde{\boldsymbol{E}}_\omega$, and the second-order susceptibility tensor, $\chi^{(2)}$.

2.3 A Brief Overview of Nonlinear Optical Effects

The general form of the susceptibility tensor was derived in the previous section. There is a great variety of effects that arise from $\chi^{(n)}$ for the different orders, n. Before going on to solve the inhomogeneous wave equation for specific cases of $n = 1$ and 2, some important nonlinear effects connected to the second order and third order susceptibility, $\chi^{(2)}$ and $\chi^{(3)}$, respectively, will be discussed in general. Additionally, the prerequisites in terms of

material symmetries will be addressed briefly. A more thorough description of nonlinear optical effects can be found in most text books on nonlinear optics [6, 11, 13].

Second-order susceptibility $\chi^{(2)}$

The second-order susceptibility describes the first correction term to the linear optical regime. Materials showing a non-zero $\chi^{(2)}$ have to be non-centrosymmetric, *i. e.*, posses no inversion symmetry. Therefore, $\chi^{(2)}$ vanishes for 11 out of the 32 crystal classes. The form of the second-order tensor for all crystal classes is given in Reference [14]. The reason for this symmetry restriction can be easily demonstrated for the case of applied monochromatic fields and an isotropic second-order susceptibility, $\chi^{(2)}_{\mu\alpha_1\alpha_2}(-\omega_\sigma;\omega_1,\omega_2) = \chi^{(2)}(-\omega_\sigma;\omega_1,\omega_2)\delta_{\mu\alpha_1}\delta_{\mu\alpha_2}$. The Fourier transform of the second-order polarization for a specific process at frequency ω_σ becomes

$$\tilde{\boldsymbol{P}}^{(2)}_{\omega_\sigma}(\boldsymbol{r}) = K(-\omega_\sigma;\omega_1,\omega_2)\varepsilon_0\chi^{(2)}(-\omega_\sigma;\omega_1,\omega_2)\tilde{\boldsymbol{E}}_{\omega_1}(\boldsymbol{r})\tilde{\boldsymbol{E}}_{\omega_2}(\boldsymbol{r}), \tag{2.13}$$

where $K(-\omega_\sigma;\omega_1,\omega_2)$ is a scalar prefactor associated with the considered nonlinear process. Applying the inversion symmetry operator $\boldsymbol{r} \to -\boldsymbol{r}$ for a material possessing inversion symmetry leads to

$$-\tilde{\boldsymbol{P}}^{(2)}_{\omega_\sigma}(\boldsymbol{r}) = K(-\omega_\sigma;\omega_1,\omega_2)\varepsilon_0\chi^{(2)}(-\omega_\sigma;\omega_1,\omega_2)\left(-\tilde{\boldsymbol{E}}_{\omega_1}(\boldsymbol{r})\right)\left(-\tilde{\boldsymbol{E}}_{\omega_2}(\boldsymbol{r})\right). \tag{2.14}$$

For applied electric fields that are non-zero, this equation can only hold if $\chi^{(2)}(-2\omega;\omega,\omega) = 0$ in accordance with the statement made above.

The effects enabled by the second-order polarization describe the mixing of two waves and have to fulfill $\omega_\sigma = \omega_1 + \omega_2$. Therefore, both sum-frequency and difference frequency generation with $\omega_\sigma = \omega_1 + \omega_2$ and $\omega_\sigma = \omega_1 - \omega_2$, respectively, are second-order nonlinear processes. Difference-frequency generation is the key effect used in optical parametric amplifiers and optical parametric oscillators. They allow for the generation and amplification of laser radiation at nearly arbitrary frequencies that are smaller than ω_1.

Energy is transfered from the pump frequency, ω_1, to the two smaller frequencies with $\omega_1 > \omega_2$ and ω_σ given from energy conservation considerations [4]. For the special case of degenerate frequencies, $\omega = \omega_1 = \omega_2$, wave mixing leads to a polarization at $\omega_\sigma = 2\omega$ and $\omega_\sigma = 0$. The former case is known as second-harmonic generation and was first observed by Franken *et al.* in 1961 [15]. It will be discussed in more detail in Section 2.4. The case of $\omega_\sigma = 0$ is optical rectification and leads to a constant polarization of the material. In combination with short laser pulses optical rectification is used for terahertz generation [16].

The Pockels effect or, equivalently, linear electro-optic effect, is closely related to optical rectification and is described by the real part of $\chi^{(2)}(-\omega; 0, \omega)$. It leads to a change of the refractive index for a wave propagating at frequency ω. This change is proportional to the applied static electric field and is widely used to build electro-optic modulators for optical telecommunications [17].

Third-order susceptibility $\chi^{(3)}$

Unlike the second-order susceptibility, $\chi^{(2)}$, relying on the lack of inversion symmetry in a material, there is no symmetry argument leading to a vanishing third-order susceptibility. Therefore, all materials show a third-order contribution to the nonlinear polarization.

The effects enabled by $\chi^{(3)}$ cover the generation of new frequencies through four-wave mixing with the degenerate case of third-harmonic generation. Similar to the second-order susceptibility, the third-order susceptibility allows for a change of the optical properties through an applied electric field. In the case of a static control field the real part of $\chi^{(3)}(-\omega; 0, 0, \omega)$ describes the quadratic electro-optic effect also known as DC Kerr effect. It gives rise to a change of the refractive index that is proportional to the square of the applied static electric field. Replacing the static field by an oscillating optical field at frequency ω_p results in what is called the AC Kerr effect. A special case of the AC Kerr effect results in an intensity dependent refractive index associated with $\mathrm{Re}\{\chi^{(3)}(-\omega; \omega, -\omega, \omega)\}$. It leads to a modulation of the

optical properties at frequency ω proportional to the intensity of the optical field itself. Self-phase modulation and self-focusing are temporal and spatial manifestations of this effect that play an important role in pulse propagation, *e. g.*, in optical fibers.

The same way the real part of the third-order susceptibility is responsible for a nonlinear contribution to the refractive index, the imaginary part of $\chi^{(3)}(-\omega;\omega_p,-\omega_p,\omega)$ contributes to the absorption coefficient in what is called two-photon absorption (2PA) [18]. Again looking at the degenerate case of a single incident frequency ($\omega_p = \omega$), the nonlinear part of the absorption coefficient scales as the beam intensity, I_ω. Therefore, the absorption probability for a plane wave propagating in z-direction with a negligible linear absorption coefficient (see Section 2.4) and an isotropic third-order susceptibility scales as the square of the intensity

$$\frac{\mathrm{d}I_\omega(z)}{\mathrm{d}z} = -\alpha_{2PA}(-\omega;\omega,-\omega,\omega)I_\omega^2(z) \tag{2.15}$$

with the nonlinear absorption coefficient, $\alpha_{2PA}(-\omega;\omega,-\omega,\omega)$, that is proportional to $\mathrm{Im}\{\chi^{(3)}(-\omega;\omega,-\omega,\omega)\}$ [19]. The process of 2PA describes an excitation to a higher energy state through the absorption of two photons with frequency, ω, each carrying an energy of $E_\gamma = \hbar\omega$. As the linear absorption coefficient is assumed to be close to zero, there is no real state for a resonant absorption of a photon with energy E_γ. Instead, a virtual state with a finite lifetime, Δt, can be excited in accordance with the uncertainty principle, $\Delta E \Delta t \sim \hbar$ [20]. If a second photon is absorbed within the time frame given by Δt the combined energy of the two photons allows for a transition to the excited state with an energy $E_{exc} = 2E_\gamma$. 2PA plays a crucial role in 3D direct laser writing that is described in more detail in Section 3.2. Furthermore, it leads to two-photon excited fluorescence that is used in nonlinear laser scanning microscopy and is a valuable tool in the nonlinear characterization presented in Section 4.2.3 [21].

2.4 Solving the Inhomogeneous Wave Equation

A variety of nonlinear optical effects has been discussed in the previous section. In this section the form of the source term and the solution of the inhomogeneous wave equation in frequency domain will be given for specific cases in both the linear and second-order nonlinear regime. The discussion is supposed to provide basics on wave propagation and facilitate an intuitive approach to some of the effects occurring in the investigated samples.

Linear Regime

The regime of linear optics covers most of the optical phenomena observed in every day life. The polarization is linear in the driving electric field strength and the material response in frequency domain is described by the linear susceptibility tensor, $\chi^{(1)}$. For the sake of simplicity an isotropic medium will be assumed with $\chi^{(1)}_{\mu\alpha}(-\omega;\omega) = \chi^{(1)}(-\omega;\omega)\delta_{\mu\alpha}$. Together with Equation 2.8 this results in a simple relation for the Fourier transform of the linear polarization

$$\tilde{\boldsymbol{P}}^{(1)}(\boldsymbol{r},\omega) = \varepsilon_0\chi^{(1)}(-\omega;\omega)\tilde{\boldsymbol{E}}(\boldsymbol{r},\omega). \tag{2.16}$$

Using this linear dependence as the source term, the inhomogeneous wave equation (see Equation 2.4) becomes

$$\nabla\times\nabla\times\tilde{\boldsymbol{E}}(\boldsymbol{r},\omega) - \frac{\omega^2}{c_0^2}\varepsilon(\omega)\tilde{\boldsymbol{E}}(\boldsymbol{r},\omega) = 0. \tag{2.17}$$

Here the scalar dielectric function, $\varepsilon(\omega) = 1 + \chi^{(1)}(-\omega;\omega)$, was introduced. This equation is the starting point for the numerical calculations describing both the linear and nonlinear response of 3D nanolaminated photonic crystals using a perturbative approach in Section 3.6. Keeping in mind that $\rho_\mathrm{f} = 0$ in dielectrics, it can be shown that $\nabla\cdot\tilde{\boldsymbol{E}} = 0$ for the considered case. Equation 2.17 can be rewritten into a simpler form:

$$\nabla^2\tilde{\boldsymbol{E}}(\boldsymbol{r},\omega) + \frac{\omega^2}{c_0^2}\varepsilon(\omega)\tilde{\boldsymbol{E}}(\boldsymbol{r},\omega) = 0. \tag{2.18}$$

A set of solutions for this equation are plane harmonic waves of the form

$$\tilde{\boldsymbol{E}}(\boldsymbol{r},\omega) = \tilde{\boldsymbol{E}}_{\boldsymbol{k}}(\omega)e^{i\boldsymbol{k}\boldsymbol{r}} \tag{2.19}$$

with the Fourier amplitude of the electric field for wave vector $\boldsymbol{k}$ denoted by $\boldsymbol{E}_{\boldsymbol{k}}(\omega)$. From $\nabla \cdot \tilde{\boldsymbol{E}}(\boldsymbol{r},\omega) = 0$ together with Equation 2.19 one can directly derive the requirement of perpendicularity that has to hold for $\boldsymbol{k}$ and $\boldsymbol{E}_{\boldsymbol{k}}(\omega)$. The wave vector, $\boldsymbol{k}$, can be further specified by introducing the plane wave solution in Equation 2.18

$$k^2 = \frac{\omega^2}{c_0^2}\varepsilon(\omega), \tag{2.20}$$

where $k = |\boldsymbol{k}|$. This is the so-called dispersion relation for a plane wave in a dispersive medium illustrating the fact that modes only exist at specific frequencies $\omega(\boldsymbol{k})$ for a given wave vector $\boldsymbol{k}$.

The wave vector also defines the propagation direction of the plane wave. For the case of isotropic media, as it is discussed here, it coincides with the direction of energy flow determined by the Poynting vector $\boldsymbol{S}(\boldsymbol{r},t) = \boldsymbol{E}(\boldsymbol{r},t) \times \boldsymbol{H}(\boldsymbol{r},t)$. In terms of monochromatic-wave amplitudes (see Equation 2.11) the optical intensity, I_ω, of a monochromatic wave at frequency, ω, is given by the magnitude of the time averaged Poynting vector [22]

$$\langle \boldsymbol{S}(\boldsymbol{r},t)\rangle = \mathrm{Re}\left\{\tfrac{1}{2}\tilde{\boldsymbol{E}}_\omega(\boldsymbol{r}) \times \tilde{\boldsymbol{H}}^*_\omega(\boldsymbol{r})\right\}. \tag{2.21}$$

Therefore, the optical intensity can be easily calculated from monochromatic-wave amplitudes derived in numerical frequency-domain calculations (see Section 3.6).

By introducing the complex refractive index $\bar{n}(\omega) = n(\omega) + i\kappa(\omega) = \sqrt{\varepsilon(\omega)}$, Equation 2.20 can be rewritten as $k = \omega/c_0 \cdot \bar{n} = 2\pi/\lambda$, where λ is the wavelength in the respective medium. In general, k, is a complex quantity describing the effect the induced linear polarization has on the propagating electromagnetic wave [23]. Compared to the propagation in vacuum, where $n(\omega) = 1$, a plane wave in a material propagates at a phase velocity that is

altered by the inverse of the corresponding refractive index

$$v_{\mathrm{ph}} = c = \frac{\omega}{\mathrm{Re}\{k\}} = \frac{c_0}{n(\omega)}. \tag{2.22}$$

For the case of a wave packet comprising waves at different frequencies given by the respective wave vectors, one can describe the movement of the packet as a whole by the group velocity $v_{\mathrm{g}} = \mathrm{d}\omega/\mathrm{d}k$. Group and phase velocity are equal in cases where $\omega \propto k$.

Whereas the real part of the complex refractive index alters the propagation velocity, a non-vanishing imaginary part of the complex refractive index leads to damping of the wave. Given the linear absorption coefficient $\alpha(\omega) = 2\omega/c_0 \cdot \kappa(\omega)$, that is directly connected to the imaginary part of the linear susceptibility, the change in the intensity of a monochromatic plane wave propagating in a homogeneous, absorbing medium follows the Beer-Lambert law [24]

$$\frac{\mathrm{d}I_\omega(z)}{\mathrm{d}z} = -\alpha(\omega) I_\omega(z). \tag{2.23}$$

Nonlinear Regime

The assumption of a material response that is linear in the driving electric field is a good and reasonable approximation. Nevertheless, it is just an approximation and, naturally, fails at a certain point. Introducing higher order contributions from the power series in Equation 2.5 leads to a polarization containing frequencies arising from the mixing of the driving electric fields. Through the wave equation it is coupled back to the electric field strength and gives rise to new effects both at the driving and at the newly generated frequencies. Usually, one has to deal with a set of coupled equations at the interacting frequencies that often have to be solved numerically.

An analytical solution may be obtained for specific cases by introducing some approximations. Similar to the linear regime it can be shown that $\nabla(\nabla \cdot \tilde{\boldsymbol{E}}(\boldsymbol{r}, \omega))$ is negligible or equal to zero, *e. g.*, for a transverse, infinite plane wave [11]. Therefore, $\nabla \times \nabla \times \tilde{\boldsymbol{E}}(\boldsymbol{r}, \omega) \approx -\nabla^2 \tilde{\boldsymbol{E}}(\boldsymbol{r}, \omega)$ and the wave

equation in frequency domain becomes

$$\nabla^2\tilde{\boldsymbol{E}}(\boldsymbol{r},\omega)+\frac{\omega^2}{c_0^2}\varepsilon(\omega)\tilde{\boldsymbol{E}}(\boldsymbol{r},\omega)=-\mu_0\omega^2\tilde{\boldsymbol{P}}^{\mathrm{NL}}(\boldsymbol{r},\omega) \tag{2.24}$$

with an isotropic linear susceptibility and the Fourier amplitude of the nonlinear polarization $\tilde{\boldsymbol{P}}^{\mathrm{NL}}(\boldsymbol{r},\omega)=\sum_{n=2}^{\infty}\tilde{\boldsymbol{P}}^{(\mathrm{n})}(\boldsymbol{r},\omega)$. A possible solution to the homogeneous part of Equation 2.24 is again in the form of plane harmonic waves (see Equation 2.19). Treating the source term as a perturbation to the homogeneous problem, it is reasonable to assume that the solution will basically retain its form with the prefactor, $\tilde{\boldsymbol{E}}_{\boldsymbol{k}}(\omega)$, becoming a function of the propagation distance due to the energy transfer between individual waves. For variations of this prefactor that are small on the scale of the considered wavelength the slowly-varying envelope approximation can be used to arrive at [6]

$$\tfrac{\partial}{\partial z}\tilde{\boldsymbol{E}}_{\boldsymbol{k}}(z,\omega)=\frac{i\omega^2\mu_0}{2k}\tilde{\boldsymbol{P}}^{\mathrm{NL}}(z,\omega)e^{-ikz}, \tag{2.25}$$

where a wave traveling in the $+z$-direction is assumed. It is worth noting that by making use of the SVEA, generated waves traveling backwards *i. e.*, in the $-z$-direction, are neglected [13].

Among the multitude of effects that can arise from the nonlinear source term the focus will be on second-harmonic generation due to its relevance for the remainder of this thesis. Therefore, the discussion will be limited to $\tilde{\boldsymbol{P}}^{(2)}$. Equation 2.25 has to hold individually for each of the contributing frequencies, *i. e.*, ω and 2ω. With an isotropic second-order susceptibility, $\chi^{(2)}_{\mu\alpha_1\alpha_2}(-2\omega;\omega,\omega)=\chi^{(2)}(-2\omega;\omega,\omega)\delta_{\mu\alpha_1}\delta_{\mu\alpha_2}$, a negligible imaginary part of the complex refractive index, and implying the validity of Kleinman symmetry the coupled equations in scalar form read [25]

$$\begin{aligned}
\tfrac{\partial}{\partial z}\tilde{\boldsymbol{E}}_{k_\omega\omega}(z)&=\frac{i\omega}{2n_\omega c_0}\chi^{(2)}(-2\omega;\omega,\omega)\tilde{\boldsymbol{E}}^{*}_{k_\omega\omega}(z)\tilde{\boldsymbol{E}}_{k_{2\omega}2\omega}(z)e^{-i\Delta kz},\\
\tfrac{\partial}{\partial z}\tilde{\boldsymbol{E}}_{k_{2\omega}2\omega}(z)&=\frac{i2\omega}{2n_{2\omega}c_0}\frac{1}{2}\chi^{(2)}(-2\omega;\omega,\omega)\tilde{\boldsymbol{E}}^{2}_{k_\omega\omega}(z)e^{i\Delta kz}
\end{aligned} \tag{2.26}$$

with the monochromatic-wave amplitudes $\tilde{\boldsymbol{E}}_{k_\omega\omega}(z)$ and the phase mismatch $\Delta k=2k_\omega-k_{2\omega}=2\omega/c_0\cdot(n_\omega-n_{2\omega})$. The refractive index and the wave

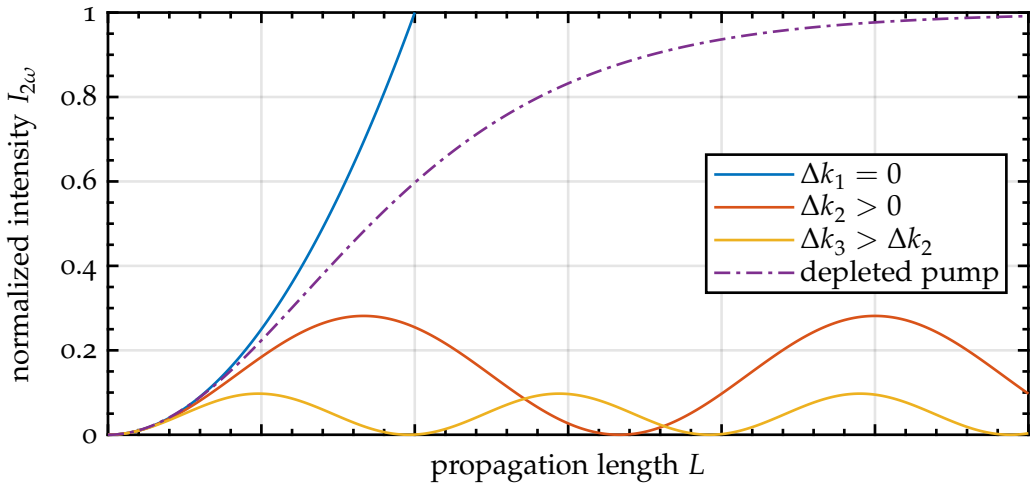

Figure 2.1: Second-harmonic intensity $I_{2\omega}(L)$ normalized to the squared initial intensity of the fundamental beam $I_{\omega}^{2}(0)$. The solid curves show the intensity $I_{2\omega}(L)$ for various values of the phase mismatch Δk according to Equation 2.27 derived using the undepleted pump approximation. A larger value of Δk results in faster oscillations and a reduced maximal second-harmonic conversion efficiency. Obviously, the undepleted pump approximation leads to unphysical behavior for a phase mismatch that tends to zero (see blue curve). In this case, the set of coupled Equations 2.26 has to be solved exactly (see dashed curve).

vector at frequency i are denoted by n_i and k_i, respectively.

For a non-vanishing phase mismatch, Δk, the overall conversion efficiency from fundamental to second-harmonic frequency is usually small. The reason is that the "polarization wave"caused by the field at frequency ω spreads with a phase velocity of ω/k_{ω}, whereas the newly generated signal at frequency 2ω has a phase velocity of $2\omega/k_{2\omega}$. These velocities tend to be different due to material dispersion and the waves at frequency ω and 2ω get out of phase. The individual intensities show an oscillatory behavior in the direction of propagation with the direction of energy flow between second-harmonic and fundamental wave being reversed after the coherence length $L_c = |\pi/\Delta k|$. Hence, for $\Delta k \neq 0$ Equations 2.26 can be decoupled using the undepleted pump approximation implying that $\tilde{\boldsymbol{E}}_{k_{\omega}\omega}(z) = \tilde{\boldsymbol{E}}_{k_{\omega}\omega}(0) = \text{const}$. In this case

the intensity of the second-harmonic wave as a function of propagation length, L, given $\tilde{\boldsymbol{E}}_{k_{2\omega}2\omega}(0) = 0$, is

$$I_{2\omega}(L) = \frac{(2\omega)^2}{8\varepsilon_0 c_0^3} \frac{|\chi^{(2)}(-2\omega;\omega,\omega)|^2}{n_\omega^2 n_{2\omega}} I_\omega^2 L^2 \mathrm{sinc}^2\left(\frac{\Delta k L}{2}\right) \tag{2.27}$$

with the sinc function defined as $\mathrm{sinc}(x) = \sin(x)/x$. The oscillation of the second-harmonic intensity with varying propagation length, L, for $\Delta k \neq 0$ (see Figure 2.1) was first demonstrated by Maker *et al.* [26]. Nowadays, these kind of oscillations are called Maker fringes and they will be utilized to calibrate the setup used for the nonlinear characterization of second-order nonlinear thin films that is described in Section 3.4. Furthermore, the effective-material hypothesis for the tailored nanolaminate metamaterials (see Section 4.1.4) will be experimentally verified based on Equation 2.27.

To achieve a considerable conversion efficiency one has to fulfill the phase matching condition, that is $\Delta k = 0$. Probably the most common approach is to make use of birefringence, *i. e.*, the dependence of the refractive index on the polarization of light, in anisotropic crystals [27]. Other approaches are quasi-phase-matching, dispersion tailoring in waveguides, and the use of anomalous dispersion regimes as they are also found in photonic crystals [28–31].

In the case of perfect phase matching ($\Delta k = 0$) the intensity at frequency 2ω grows as L^2 (see Equation 2.27). Therefore, at a certain point the assumption of an undepleted pump is no longer valid and the coupled set of Equations 2.26 has to be solved exactly. The solution describes a continuous transfer of energy from the fundamental to the second-harmonic wave that saturates due to the decreasing fundamental intensity [28]. This behavior is depicted by the dashed curve in Figure 2.1.

2.5 Photonic Crystals

Having covered the basics on electromagnetic wave propagation and nonlinear optical effects, the focus in this section will lie on the properties of photonic crystals. The idea behind photonic crystals will be briefly motivated by making use of analogies found in the field of solid-state crystals. Subsequently, fundamental concepts like the dispersion relation, bandgaps, and the first Brillouin zone will be introduced. Finally, the unique properties of photonic crystals, and how these can benefit nonlinear optical interactions, will be discussed.

The revolution in information and communication technology in modern days is founded in the ability to understand and manipulate the electrical properties of materials, and especially conducting crystals, at will. Crystals are made up from a basic building block, called the basis that is positioned at periodically arranged lattice points. A basis can consists of one or multiple atoms in a fixed arrangement. The properties of electrons in solid-state crystals are described by their energies and wave functions that are determined by solving the Schrödinger equation for a potential that shows the same periodicity as the crystal lattice [23]. The solutions to this eigenvalue problem describe an interesting behavior: In contrast to the continuous energy values found in a free electron gas, the electron energies in crystals are restricted and form "bands". Especially, there are energy intervals, known as bandgaps, where there are no electronic eigenstates and propagation is forbidden altogether.

It is assumed that another technological leap would follow if one would be able to extend the control that is nowadays given for the electrical properties of a material to also cover its optical properties [5, 32]. Fortunately, one can benefit from the experience and knowledge in the field of electronics that was gathered over many years, to develop the necessary materials and devices for optics. The reason is that a lot of the principles that govern the motion of electrons in a solid-state crystal can be analogously applied to the propagation of photons in artificial periodic dielectric structures with a

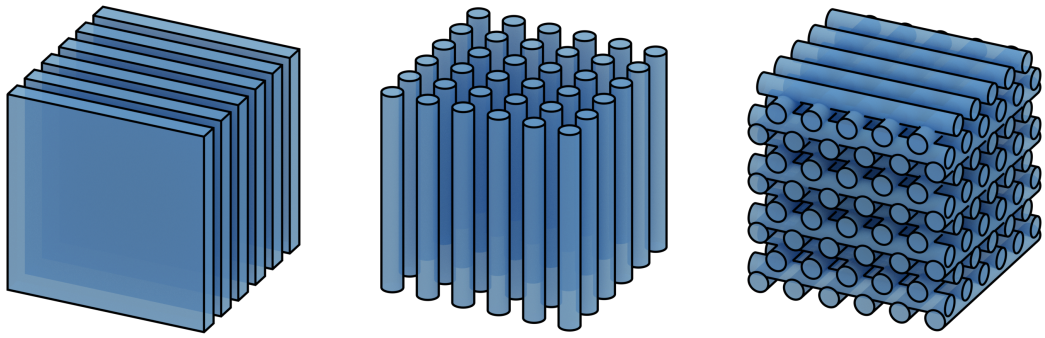

1D 2D 3D

Figure 2.2: Scheme of photonic crystals with a periodic modulation of the dielectric function in one, two, and three dimensions, 1D, 2D, and 3D, respectively. The shown 3D example is a so-called woodpile photonic crystal.

periodicity on the order of the interacting photon wavelength. In analogy to solid-state crystals, these structures are called photonic crystals, and are classified as one-, two, or three-dimensional (1D, 2D, or 3D, respectively) depending on the dimensionality of the periodic variation of optical properties (see Figure 2.2) [33, 34]. A simple and very common example of what is sometimes called a 1D photonic crystal is just a laminated medium and was already described by Lord Rayleigh in 1887 [35].

In the description of a photonic crystal, dielectric elements constitute the basic building blocks. These are placed at lattice points described by the lattice vectors $\boldsymbol{R} = m_1\boldsymbol{a}_1 + m_2\boldsymbol{a}_2 + m_3\boldsymbol{a}_3$, where m_i are integers and $\boldsymbol{a}_i$ denote the fundamental translation vectors. The latter span a unit cell that, when repeated, fills the whole space. An example of a 2D hexagonal lattice with a possible choice of translation vectors and unit cell is illustrated in Figure 2.3a. The eigenvalue problem for photons in a photonic crystal is given by the inhomogeneous wave equation with periodically varied optical properties (see Equation 2.17) [36]. Usually, one studies linear photonic crystals that are characterized by a spatial modulation of the linear susceptibility, $\chi^{(1)}$, and, hence, posses a periodic dielectric function. Another example are quadratic nonlinear photonic crystals that show a periodically varied second-order susceptibility, $\chi^{(2)}$, and a spatially constant dielectric function [37]. The focus

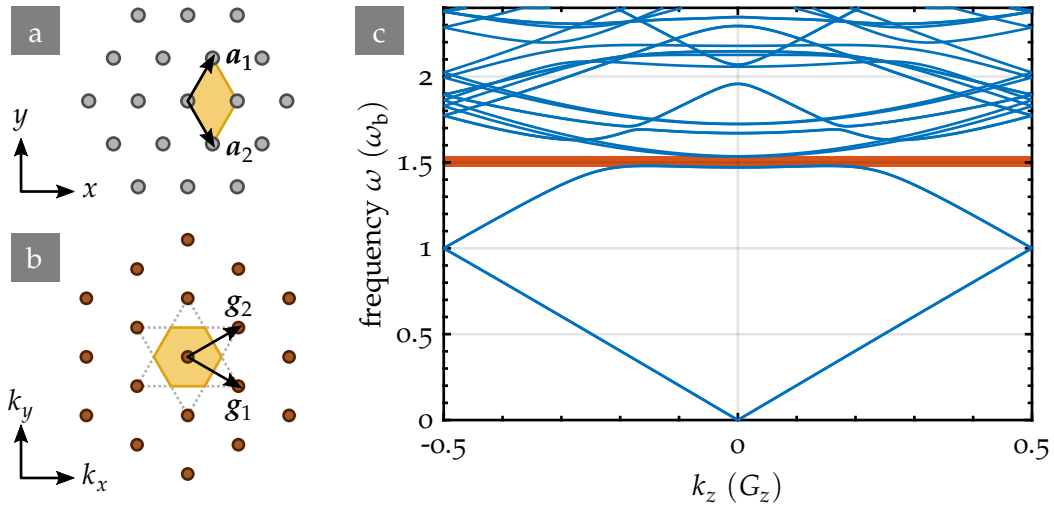

Figure 2.3: a) 2D example of a crystal lattice. The fundamental translation vectors, $\boldsymbol{a}_i$, of the hexagonal lattice and a possible choice of the unit cell (yellow area) are indicated. b) Reciprocal lattice of the crystal lattice shown in a). The fundamental reciprocal lattice vectors are denoted by $\boldsymbol{g}_i$. The first Brillouin zone is highlighted in yellow and given by the area of the k-space that is closer to one reciprocal lattice point than to all the others. c) Band structure of a 3D photonic crystal calculated for $k_x = k_y = 0$. The frequency is given in units of the stop band frequency, $\omega_b = \pi c_0/(n_{\text{eff}} a_z)$, with the lattice constant in z-direction, a_z, and the effective refractive index, n_{eff}. The latter is calculated from the slope of the lowest band.

in the following will be on linear photonic crystals unless stated otherwise.

To get a better understanding of the behavior of photons in a photonic crystal, it is instructive to have a look at the form of the solutions to the eigenvalue problem. For the sake of simplicity, the dielectric function is assumed to be scalar. The periodicity of the structure implies that

$$\varepsilon(\boldsymbol{r} + \boldsymbol{R}, \omega) = \varepsilon(\boldsymbol{r}, \omega) \tag{2.28}$$

has to hold for arbitrary lattice vectors, $\boldsymbol{R}$. The periodic dielectric function can be expanded as a Fourier series

$$\varepsilon(\boldsymbol{r}, \omega) = \sum_{\boldsymbol{G}} \tilde{\varepsilon}_{\boldsymbol{G}}(\omega) e^{i\boldsymbol{G}\boldsymbol{r}} \tag{2.29}$$

with the Fourier components $\tilde{\varepsilon}_G$ and the reciprocal lattice vectors $\boldsymbol{G} = l_1\boldsymbol{g}_1 + l_2\boldsymbol{g}_2 + l_3\boldsymbol{g}_3$, where l_i are integers. The fundamental reciprocal lattice vectors, $\boldsymbol{g}_i$, are defined through Equation 2.28 and a given set of fundamental translation vectors, $\boldsymbol{a}_i$, (see Figure 2.3b).

The eigenmodes of the photonic crystal eigenvalue problem describe the electromagnetic fields and take the form of Bloch modes. Therefore, the Fourier amplitude of the electric field for a given Bloch wave vector, $\boldsymbol{k}$, can be expressed as

$$\tilde{\boldsymbol{E}}_{k\omega}(\boldsymbol{r}) = \boldsymbol{u}_{k\omega}(\boldsymbol{r})e^{i\boldsymbol{k}\boldsymbol{r}}. \tag{2.30}$$

Here, $\boldsymbol{k}$ is restricted to the so-called first Brillouin zone that is defined as the k-space that is closer to one specific reciprocal lattice point than to any other (see Figure 2.3b). An expression similar to Equation 2.30 can also be found for the magnetic field strength. In contrast to the case of a spatially constant dielectric function, where a set of solutions was given by plane waves (see Section 2.4), the eigenmodes in a periodic structure are plane waves that are, additionally, modulated by the lattice periodic function $\boldsymbol{u}_{k\omega}(\boldsymbol{r})$ with $\boldsymbol{u}_{k\omega}(\boldsymbol{r}) = \boldsymbol{u}_{k\omega}(\boldsymbol{r} + \boldsymbol{R})$. The corresponding eigenvalues are directly associated with the frequencies, $\omega(\boldsymbol{k})$, of the respective photonic crystal modes. The characteristic dependence of $\omega(\boldsymbol{k})$ on $\boldsymbol{k}$ describes the photonic crystal dispersion relation that is also known as the band structure. An example of $\omega(\boldsymbol{k})$ for a 3D woodpile photonic crystal assuming $k_x = k_y = 0$ is depicted in Figure 2.3c. The stop band is indicated in red and located between the second and third band for this specific case.

In a homogeneous material, continuous translation symmetry demands the conservation of the wave vector, or, equivalently, the momentum $\boldsymbol{p} = \hbar\boldsymbol{k}$. This is no longer given for periodically varied material properties like they are found in photonic crystals. The periodicity leads to a discrete translational symmetry and the wave vector, $\boldsymbol{k}$, is only conserved modulo a reciprocal lattice vectors, $\boldsymbol{G}$. Therefore, solutions of the eigenvalue problem for a given $\boldsymbol{k}$ are identical to solutions for all $\boldsymbol{k}' = \boldsymbol{k} + \boldsymbol{G}$ with arbitrary reciprocal lattice vectors, $\boldsymbol{G}$. Hence, each solution can be "shifted"such that its resulting wave vector, $\boldsymbol{k}$, lies in the first Brillouin zone. Consequently, it

suffices to look at the solutions in this part of the k-space.

Due to the analogy to solid-state crystals, it is not surprising that the periodic variation of optical properties in a photonic crystals often results in frequency regions where there are no photonic modes. Photons at these frequencies cannot propagate inside the photonic crystal and are reflected. Unlike in the electronic case, in photonics a complete bandgap, *i. e.*, an overlapping forbidden frequency region for arbitrary propagation directions and polarizations, is not achieved easily. It usually requires a high refractive index contrast of the used dielectrics and is exclusively reserved to 3D photonic crystals [22]. In order to avoid misunderstandings the term stopband will be used in this thesis to denote a frequency gap that exists only for certain directions or polarizations. Nevertheless, it is possible to create states in this forbidden frequency region by deliberately introducing defects into the photonic crystal. These defects usually come in the form of a local increase or decrease of the dielectric function and can be classified as point, line, or plane defects [38]. They lead to the localization of modes and find use in many photonic devices, like for example, photonic cavities and low-loss waveguides [39, 40].

Nonlinear Interactions in Photonic Crystals

Photonic crystals are designed and used to tailor the optical properties and control the flow of light at will. This degree of control leads to a variety of functionalities and applications in the linear regime. Obviously, the unique properties of photonic crystals can also be used in nonlinear optical processes. In this section, two basic approaches that lead to greatly enhanced nonlinear interactions in photonic crystals will be discussed.

First, photonic crystals can facilitate phase matching even for materials that cannot be phase matched otherwise, *e. g.*, because they show no birefringence. The dispersion of a photonic crystal can be controlled by tuning geometrical parameters and can be adjusted such that it counteracts the given material dispersion. Optical materials usually show normal dispersion, *i. e.*, an increasing refractive index for increasing frequency. The refractive index for

a monochromatic electromagnetic wave in a photonic crystal is determined by the phase velocity that can be calculated from the band structure. For small frequencies corresponding to wavelengths that are large compared to the period of the photonic crystal, the individual features of the structure are not resolved and it shows properties that can be simply described by an effective refractive index determined through the properties of the constituting materials. With the wavelength decreasing and approaching the first stop band or bandgap, the interactions between wave and photonic crystal become stronger and result in an additional contribution to the total dispersion due to so-called geometrical dispersion [41]. Whereas this leads to even stronger normal dispersion on the long-wavelength side of the stop band or bandgap, anomalous dispersion is found across the gap region itself and, therefore, allows for perfect phase matching by tuning the interacting waves appropriately [42–45].

A slightly different aspect is the relaxed crystal momentum conservation that translates into a generalized phase matching condition in photonic crystals. It is worth noting that this phase matching scheme is often discussed in connection with nonlinear or $\chi^{(n)}$ photonic crystals for $n \geq 2$. In these photonic crystals, the linear susceptibility is kept constant throughout the whole structure. Thereby, undesired reflections and backscattering that might lead to a decrease in efficiency are avoided. The periodicity of material properties is given by the variation of the nonlinear susceptibility $\chi^{(n)}$. For the case of $n = 2$ and the process of second-harmonic generation the relaxed phase matching condition reads [37]

$$\Delta \boldsymbol{k} = 2\boldsymbol{k}_{\omega} - \boldsymbol{k}_{2\omega} - \boldsymbol{G} = 0 \tag{2.31}$$

with the wave vector at frequency i denoted by $\boldsymbol{k}_i$. The phase mismatch that originates from the material dispersion can be compensated for by a reciprocal lattice vector of the photonic crystal providing an additional momentum $\hbar\boldsymbol{G}$. This approach is called quasi-phase-matching and has been known in nonlinear periodically poled 1D structures for a long time (see Section 2.1). The generalization to higher dimensions in 2D and 3D photonic crystals allows for quasi-phase-matching to be fulfilled simultaneously for multiple directions and frequencies in the same structure. This has been ex-

tensively studied and experimentally demonstrated in 2D nonlinear photonic crystals [37, 46]. Due to the challenging fabrication the first 3D nonlinear photonic crystals were fabricated just recently by means of femtosecond laser writing approaches [47–49].

The second way nonlinear interactions are enhanced in a photonic crystal is through reinforced light-matter interactions. These can be achieved using dispersion related slow-light effects or strong mode confinement. Slow-light effects in photonic crystals usually arise at the boundaries of the Brillouin zone where a significant decrease of the group velocity, v_g, is observed. In a simple geometrical-optics model this low group velocity can be understood as a net effect caused by either coherent backscattering or omnidirectional reflection in the structure [50]. The optical interactions in the slow-light regime have been shown to be enhanced by a factor proportional to the slowdown factor, $S = v_{ph}/v_g$, in linear effects and by even higher orders in nonlinear processes [50–53]. The downside is that losses have been reported to increase as well and scale at least with a factor of S [54].

Enhanced light-matter interactions can also be achieved by confining light in one, two, or three dimensions. One example that was mentioned before are defect modes in the form of waveguides or cavities [39, 55–57]. Another way to confine the photonic crystal mode to two dimensions is to considerably limit the extent of the photonic crystal in one direction. The guiding mechanism in these 2D photonic crystal slabs, that are surrounded by a low refractive index medium, are analogous to the ones exploited in dielectric slab waveguide (see Section 2.6). Modes in waveguides and cavities can be characterized by their mode volume, V_{eff}, and, in case of resonating structures, their quality factor, Q. The mode volume describes the spatial confinement and the energy density of the mode. Its theoretical lower limit is given by half the wavelength in each confinement direction. The quality factor of a resonating structure is a measure of the temporal confinement and can be expressed as the ratio of the stored energy to the energy that is dissipated per oscillatory cycle. Lossy resonator modes show a slow decay and, therefore, behave as if they have a complex frequency $\omega_c = \omega - i\gamma$, where ω and γ are the resonance frequency and the attenuation rate, respec-

tively. The power decay of these modes is proportional to $\exp(-2\gamma t)$ and the quality factor, Q, is given as

$$Q = \frac{\omega}{2\gamma}. \tag{2.32}$$

Both the increase in spatial and temporal confinement cause an enhancement of nonlinear interactions. This was demonstrated using point defects and photonic crystal slabs for various nonlinear processes [58–65]. The confinement effects found in 2D photonic crystal slabs are of special interest for this work. Therefore, the corresponding modes will be studied in more detail from the point of view of dielectric waveguides showing a periodic modulation.

2.6 Dielectric Waveguides

The 3D nanolaminated photonic crystals that will be discussed in more detail in Section 4.2 are basically conformally coated 3D photonic crystals. Nevertheless, some of the features linked to the strong enhancement of second-harmonic generation in these structures can be intuitively understood in analogy with the properties of dielectric waveguides. Therefore, this section will cover fundamental properties derived for the example of an asymmetric dielectric slab waveguide. Talking about waveguides one cannot avoid mentioning the arrangements necessary to couple light into the waveguide modes. A very common approach is the introduction of a periodic modulation that leads to a dispersion relation closely related to that of a photonic crystal slab. This aspect will be discussed in the last part of this section.

Guiding light from one point to another by means of free-space optics can be quite tedious. The beam broadens and has to be refocused repeatedly on its way. Optical dielectric waveguides offer a solution by confining light and allowing for flexible and low-loss transport of light over thousands of kilometers. The operation is based on total internal reflection that occurs at the boundary between two dielectrics with refractive indices n_c and n_f. For $n_f \geq n_c$ and a ray coming from the medium with higher refractive index

n_f, total internal reflection occurs for angles of incidence, θ, larger than the critical angle, $\theta_c = \arcsin(n_c/n_f)$. Therefore, it is possible to trap light in a waveguide by embedding a lossless dielectric with refractive index n_f in a medium with lower refractive index n_c. One speaks of a mode of this waveguide if the twice reflected wave interferes constructively with the original wave. This requirement is called the self-consistency condition and can be fulfilled for discrete values of the incidence angle, θ_m, with $\theta_m < \theta_c$.

The waveguide modes are exemplary derived for an asymmetric slab waveguide. It consists of a guiding film of thickness h and refractive index n_f that is sandwiched between a cover and a substrate with refractive indices, n_c and n_s, respectively (see Figure 2.4a). Additionally, $n_f > n_s > n_c$ is assumed. The guided modes propagate in y-direction and the structure is invariant along the x-direction. In this case the self-consistency condition reads [66]

$$2kn_f \cos(\theta_m)h - 2\varphi_s - 2\varphi_c = 2\pi m \tag{2.33}$$

with the vacuum wave vector $k = 2\pi/\lambda$ and the mode index m. The total phase between initial and twice reflected wave is a sum of the phase accumulated through propagation given by the first term and additional phase shifts $2\varphi_s$ and $2\varphi_c$ due to total internal reflection at the film-substrate and the film-cover interface, respectively. The phase shifts caused by total internal reflection are given by the Fresnel equations. The guided wave propagates into the y-direction with the propagation constant $\beta_m = kn_f \sin(\theta_m)$. Equation 2.33 can be solved and gives the dispersion relation for an asymmetric slab waveguide. Figure 2.4b shows the solution for a transverse electric (TE) wave with $m = 0$ to 3. The guided modes are found between the light lines representing propagation in a homogeneous medium with refractive index n_f as the lower limit and a medium with the refractive index n_s as the upper limit. A continuum of radiation modes follows above the substrate light line.

The total number of guided modes, M, is limited by the fact that the mode angle, θ_m, has to be greater than both of the two critical angles for total internal reflection at the interface to substrate and cover, θ_s and θ_c, respectively, with $\theta_s > \theta_c$ for the given example. Using the ceiling function $\lceil x \rceil$ that maps

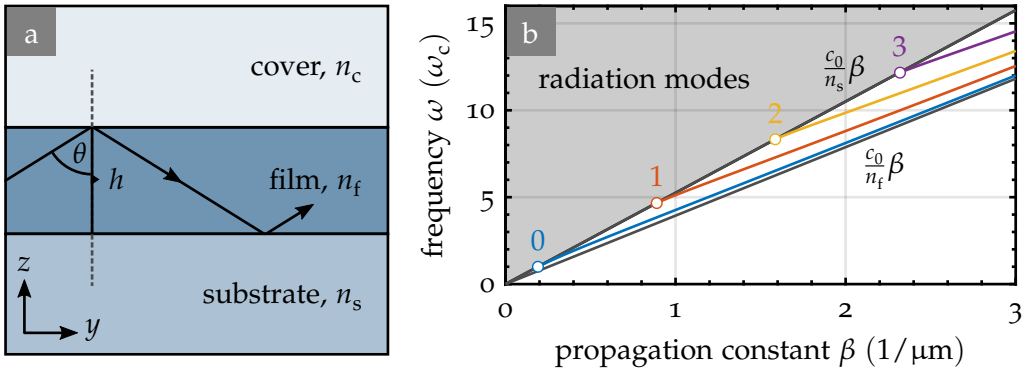

Figure 2.4: a) Scheme of an asymmetric slab waveguide that consists of a guiding film with thickness h and refractive index n_f sandwiched between a substrate and a cover layer with refractive indices n_s and n_c, respectively. For $n_f > n_s > n_c$ and an incidence angle, θ, that is larger than the critical angle, θ_c, total internal reflections at the interfaces with both substrate and cover can lead to the formation of a guided mode. b) Dispersion relation of the asymmetric dielectric slab waveguide for TE waves. The frequency, ω, is given in units of the cutoff frequency, ω_c, of the fundamental mode with $m = 0$. The waveguide modes are depicted for different mode indices, $m = 0$ to 3, indicated above the respective cutoff frequencies. The modes are bounded by the light lines of film and substrate, and the continuum of radiation modes is found above the substrate light line.

x to the smallest integer that is larger or equal to x, the number of guided modes, M, can be expressed as

$$M = \left\lceil \frac{2h}{\lambda} \sqrt{n_f^2 - n_s^2} \right\rceil . \tag{2.34}$$

Obviously, the number of modes increases with increasing thickness of the guiding film, h, and decreasing vacuum wavelength, λ. Unlike the case of a symmetric slab waveguide with $n_s = n_c$, the asymmetric slab waveguide has a non-vanishing cutoff frequency, ω_c, for the fundamental mode, $m = 0$, (see Figure 2.4b). Below this frequency there are no guided modes.

Considering a TE wave in an asymmetric slab waveguide with the electric field vector pointing in the x-direction, the complex field amplitude is independent of x and the guided modes inside the film can be described by

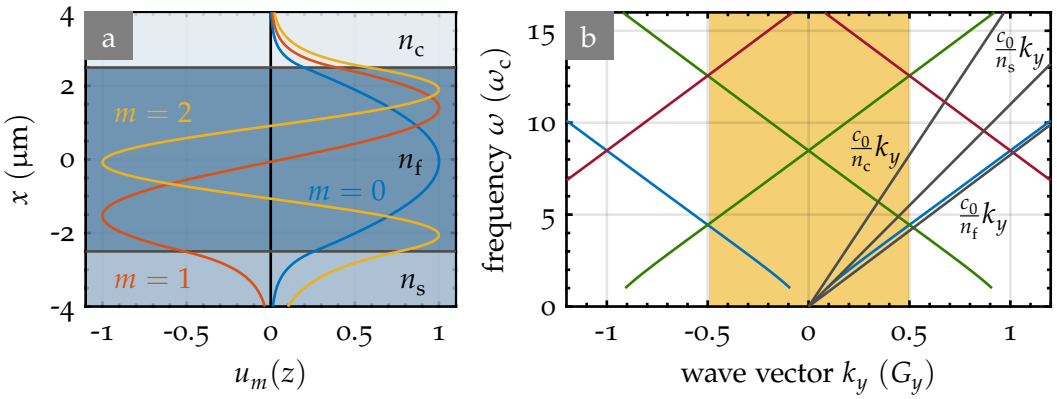

Figure 2.5: a) Normalized transverse field distribution $u_m(z)$ of three guided modes with $m = 0$ to 2 given at a fixed frequency. The number of zero-crossings increases with the mode order m. b) Dispersion relation of an asymmetric slab waveguide as shown in Figure 2.4a with an additional periodic modulation in the y-direction given by the lattice constant a_y. For simplicity only the fundamental mode ($m = 0$) is depicted and the effects of the modulation on the dispersion curve are neglected. Nevertheless, the periodicity causes the modes for wave vectors k_y and $k_y + G_y$ with $G_y = 2\pi/a_y$ to become identical. Therefore, the dispersion curves can be shifted by reciprocal lattice vectors G_y and it is sufficient to look at the modes in the first Brillouin zone marked yellow. The original dispersion is plotted in blue, the green and red curves are shifted by $\pm G_y$ and $\pm 2G_y$, respectively. In addition to the guided modes that existed before the periodicity was introduced, guided resonances occur above the light lines of both substrate and cover. These modes couple to the continuum of radiation modes and at the same time still show a strong confinement in the guiding film.

plane waves of the form

$$\left[\tilde{E}_\omega(y,z)\right]_x = a_m u_m(z) e^{i\beta_m y}, \tag{2.35}$$

where a_m is a constant. The function $u_m(z)$ can be derived from Maxwell's equations and by applying the proper boundary conditions [66]. It describes the transverse field distribution in the film and is depicted for a fixed frequency in Figure 2.5a for $m = 0$ to 2 together with the corresponding functions in the substrate and cover regions. The number of zero-crossings is determined through the waveguide mode order, m, and given by $m - 1$. The asymmetry of the structure is caused by the difference in refractive indices of

substrate and cover. For $n_s > n_c$ this results in waveguide modes penetrating deeper into the substrate underneath than into the cover on top of the film.

Having calculated the waveguide modes that are allowed for a given geometry one has to think about possibilities to couple light into these modes. To a certain extent the following considerations are also applicable to geometries other than the asymmetric slab waveguide. For a specific frequency ω in the dispersion relation (see Figure 2.4b), the wave vector component in propagation direction, k_y, of the radiation modes in both substrate and cover layer is always smaller than β_m of the guided mode in the film. Translation symmetry in the direction parallel to the film requires the conservation of the corresponding wave vector component k_y. Therefore, it is not possible to couple light coming from the substrate or cover into a waveguide mode without additional effort. Several approaches exist to tackle this challenge. A quite straightforward way to go is to couple the light by focusing it on the facet of the waveguide. This way, the conservation of the wave vector poses no limitation. The disadvantage of this approach is the required alignment precision determined by the waveguide dimensions. Another approach often found for an air cover layer, is the use of a prism with a refractive index n_p that is larger than n_f. The prism is placed in close proximity to the guiding film and light is sent into the prism in a way that leads to total internal reflection at the interface between towards air. This way the wave vector in y-direction is sufficiently large to allow for coupling to the guided modes based on the process of frustrated total internal reflection, *i. e.*, an energy transfer mediated by the evanescent field that extends over the air gap between prism and film.

Aside from using an additional medium with a refractive index larger than that of the guiding film, one can introduce an additional wave vector contribution to match the y-component of the incident wave vector with the propagation constant. As already discussed in connection with quasi-phase-matching for nonlinear processes in Section 2.5, a periodic modulation of optical properties can facilitate matching of the respective wave vectors due to the flexibility to add or subtract a reciprocal lattice vector, $\boldsymbol{G}$. In the same spirit, a grating coupler or other kinds of periodic modulations of

the waveguide can be used to provide the missing wave vector component in propagation direction. For light incident from the cover layer under an angle θ_i measured with respect to the surface normal, the phase matching condition is

$$\beta_m = n_c k \sin(\theta_i) + q\frac{2\pi}{a}, \tag{2.36}$$

where a is the periodic modulation of the waveguide film and q is an integer. Aside from the necessity to establish phase matching, the coupling efficiency and the actually excited waveguide modes are determined by the overlap between the field distributions of the light coupled into the waveguide and the guided modes.

The introduction of periodicity as a way to allow for coupling to waveguide modes can also be considered from the point of view of the dispersion relation. For the sake of simplicity, the effect a periodic modulation in y-direction will be only considered in terms of the relaxed momentum conservation. The impact on the curvature of the asymmetric slab waveguide dispersion (see Figure 2.4b) will be neglected for the moment. The eigenmodes and frequencies for the wave vectors $\boldsymbol{k}$ and $\boldsymbol{k} + \boldsymbol{G}$ become identical as it was already described for photonic crystals. Therefore, the waveguide dispersion relation can be redrawn such that the whole information is contained in the first Brillouin zone. In the given case the reciprocal lattice vector is $\boldsymbol{G} = G_y \hat{\boldsymbol{e}}_y$. The unit vector in y-direction is denoted by $\hat{\boldsymbol{e}}_y$ and $G_y = 2\pi/a_y$ is the magnitude of the reciprocal lattice vector with the period of modulation given by a_y. The resulting dispersion relation is shown exemplary for the fundamental waveguide mode ($m = 0$) in Figure 2.5b with the propagation constant, β, replaced by the wave vector component k_y. Higher order modes ($m > 0$) would undergo the same process but are not depicted for the sake of simplicity. The guided modes between the substrate and the film light line that show a strong field confinement in the film are still present. Additionally, new modes in the radiation regime above the light line of both the cover and the substrate layer appear. These modes still show a strong field confinement in the film but also couple to the continuum of radiation modes *via* the grating coupler effect. They are called leaky modes or guided resonances and are characterized by a finite lifetime and a

quality factor, Q, [55, 67]. Another point that is worth noting is that these modes exist for $k_y = 0$ and, therefore, can be excited under normal incidence.

Discarding the initial assumption of an infinitesimally small effect of the periodic modulation on the curvature of the dispersion relation, gaps open up at the crossing points, *e.g.*, at the center and edges of the Brillouin zone. The resulting dispersion relation of a periodically modulated waveguide is closely related to that of a photonic crystal slab. This resemblance is due to the structural similarity between the two systems. Consequently, the guided resonances mentioned above are found in both systems and pose an interesting approach to couple light in and out. At the same time, the resonances show a strong field confinement in the guiding layer that leads to reinforced light-matter interactions. The excitation of guided resonances is an important mechanism for the observed enhancement of second-harmonic generation in 3D nanolaminated photonic crystals presented in Section 4.2.3. The fact that guided resonances also occur in these structures can be intuitively understood if one regards them as leaky waveguides or "3D photonic crystal slabs".

2.7 Metamaterials

Optical waveguides and photonic crystals were shown to provide versatile tools to tailor light propagation and light-matter interactions in general. The extraordinary properties of photonic crystals are a direct consequence of the periodic arrangement of different materials on a scale that is comparable to the wavelength of interacting light. Therefore, the individual building blocks are still resolved and the response is mainly determined by interference and diffraction of the incident light. This changes when considering a photonic crystal in the long wavelength limit, *i.e.*, for small frequencies, ω. Here, the modulation of optical properties occurs on a scale that is way smaller than the wavelength of the interacting light and the details of the material distribution can no longer be resolved. The photonic crystal behaves like a bulk material and can be described using effective material parameters. This long wavelength limit is where the border between photonic crystals and metamaterials becomes blurred. An introduction to the ideas behind this rel-

atively new class of materials will be given in this section. The application of the metamaterial concept in various research areas will be presented. Finally, the focus will be once again on nonlinear optical phenomena and, especially, on all-dielectric metamaterials as they are related to the nanolaminate optical metamaterials designed and fabricated in Section 4.1.

Ordinary matter is built from an arrangement of atoms or molecules. The different atoms and molecules, their arrangement and their interaction with each other determine the effective properties of the resulting material. It is possible to manipulate the material composition and its structure, at least to a certain degree, to arrive at the desired properties, but, obviously, this is usually not straight forward and one is limited in the choice of the basic atomic building blocks. This is where the metamaterial idea comes into play. One starts from a meta-atom that is an artificially constructed building block on a scale that is much smaller than the wavelength of stimuli. Subsequently, the metamaterial is built by periodical arrangement of this meta-atom and can be described as a homogeneous medium with effective material parameters. The bulk metamaterial limit is reached as soon as these parameters converge and remain unchanged for an increasing number of periods [68]. The intriguing aspect of metamaterials is that the properties of the bulk are determined by the structure of the building block and not just by the constituent materials [69]. This rational design approach facilitates metamaterials with properties that sometimes even go beyond what is found in nature.

The starting point for the recent boom in metamaterial research was based on the idea of realizing a negative refractive index material and applying it to build a perfect lens [70–72]. A negative refractive index can be obtained if both the effective dielectric function, ε_{eff}, and the effective magnetic permeability, μ_{eff}, are negative for the same frequency

$$n_{\text{eff}} = \sqrt{\varepsilon_{\text{eff}}\mu_{\text{eff}}} < 0 \tag{2.37}$$

with $\varepsilon_{\text{eff}} < 0$ and $\mu_{\text{eff}} < 0$. Conventional materials showed to be of no use to arrive at the required negative magnetic permeability in the optical regime. Contrary to that, metamaterials met the requirements by introducing

meta-atoms with a non-vanishing coupling to an external magnetic field. As in the case of the dielectric function, the magnetic permeability becomes negative close to the resonance. This allows for the realization of a negative index of refraction at frequencies ranging from the microwave to the optical regime [68]. The field of metamaterials expanded beyond negative refractive index materials to cover other electromagnetic phenomena, like chirality, nonlinearity, and invisibility cloaking [73–80].

Obviously, the concept is not limited to electromagnetism and found its way into many other research areas [81]. In thermodynamics, rationally designed metamaterials were used to implement inhomogeneous and anisotropic distributions of material properties derived from coordinate transformations. These transformations can be used to mold the flow of heat or diffusive particles by design and, for example, guide them around an obstacle [82, 83]. Mechanical metamaterials expand the available parameter space of material properties through ultra-lightweight, auxetic, and pentamode materials [84–86]. Additionally, previously unavailable degrees of freedom can be addressed like for example the coupling of a longitudinal deformation to a twist of the whole medium [87]. The intriguing fact that the properties of metamaterials depend on the meta-atom structure is demonstrated beautifully in designs that allow for a continuous tuning of the effective material properties through the change of geometrical meta-atom parameters. This tuning even allows for a sign-inversion with respect to the properties of the constituent materials. Examples are a negative thermal-expansion coefficient for a metamaterial built from constituents showing a positive coefficient, and a Hall coefficient that is negative with respect to the metamaterial constituents [88].

It is said that the next big step for metamaterials lies in the "development of active, controllable and nonlinear metamaterials" [89]. The latter are an important part of this work and, therefore, the following subsection will deal with the impact of metamaterials on nonlinear optics in more detail.

Nonlinear Optical Metamaterials

There are various approaches to create metamaterials with a nonlinear response that differ by their applicability in different frequency regimes and the role the meta-atom plays [90]. One way is to make use of the nonlinear response of the constituents the metamaterial is built of [76]. Another commonly followed approach is to start out with a metamaterial and complement it by an additional nonlinear element. This nonlinear ingredient may come in the form of an insertion in the gap of a split-ring resonator, a substrate, a superstrate, or a nonlinear medium the metamaterial is embedded in [91–93]. Finally, the nonlinearity can be introduced by properly structuring the constituents in a way that gives rise to a collective nonlinear response, although, the constituents show no nonlinearity by themselves [94, 95].

Independent of the actual implementation, metamaterials can be used to generate, enable, and enhance nonlinear optical phenomena in different ways. Some of the exploited mechanisms are not exclusive to metamaterials and can, for example, also be found in photonic crystals (see Section 2.5). Others give rise to approaches that are exclusive to metamaterials.

One fascinating aspect of metamaterials is the possibility to deliberately tune the magnetic and electric resonances and optimize them for specific nonlinear interactions, or even enable interaction schemes that are not possible otherwise. Suchowski *et al.* have shown that phase-mismatch free four-wave mixing is possible in metamaterials with a refractive index of zero [96]. The interacting waves can be tuned to give perfect phase matching in both the forward and backward direction at the same time. A different example is given by second-harmonic generation in a metamaterial that shows a negative index of refraction $n_{\omega,\mathrm{eff}} < 0$ for the fundamental and a positive index of refraction $n_{2\omega,\mathrm{eff}} > 0$ for the second-harmonic frequency. If these refractive indices have the same magnitude backward phase matching is achieved and the material acts as a nonlinear-optical mirror that can convert the incoming wave at frequency ω into a reflected wave at frequency 2ω with very high efficiency [97].

Another aspect is that metamaterials allow for a precise control and rational design of the electric and magnetic field distribution. The nonlinear response can be enhanced by making use of strong electromagnetic fields in the vicinity of resonant structures. Additionally, a field distribution tailored by proper metamaterial design allows for coupling of the electric field to specific components of the nonlinear susceptibility tensor that might not be accessible otherwise [92, 98].

The metamaterial designs mentioned so far show fascinating phenomena but also have their disadvantages when it comes to their application in optical devices. They are all based on meta-atoms with metallic constituents and many of them are operated at frequencies that are close to resonances. This leads to limitations due to a small operation bandwidth or increased losses of the metals at optical frequencies. Strongly enhanced nonlinear interactions become of less practical use when they are accompanied by a strongly reduced interaction length and, therefore, low efficiency [99]. Furthermore, these structures are often incompatible with complementary metal-oxide semiconductor fabrication processes. Here, all-dielectric nonlinear metamaterials may offer a solution. The losses can be significantly reduced using dielectric, high refractive index materials like silicon or titanium dioxide (TiO_2) to construct the meta-atom. At the same time, Mie resonances can be used to engineer metamaterial functionalities comparable to the ones found in the metal-based case [100].

An interesting approach that does not rely on meta-atom resonances, but on the structural tailoring of a second-order nonlinear response, are ABC-type nanolaminates [95, 101]. These metamaterials are built from alternating layers of centrosymmetric low-loss dielectrics. Possessing inversion symmetry, the individual constituents show a second-order susceptibility that is equal to zero in the bluk (see Section 2.3). Nevertheless, the final metamaterial shows a nonlinear response with $\chi^{(2)} \neq 0$. The underlying idea is the proper tailoring of nonlinear surface susceptibilities, $\chi_s^{(2)}$, that arise at the individual interfaces where the inversion symmetry is locally broken. From a microscopic point of view this can be understood as follows: Nonlinear effects arise whenever the potential becomes anharmonic and, hence, the

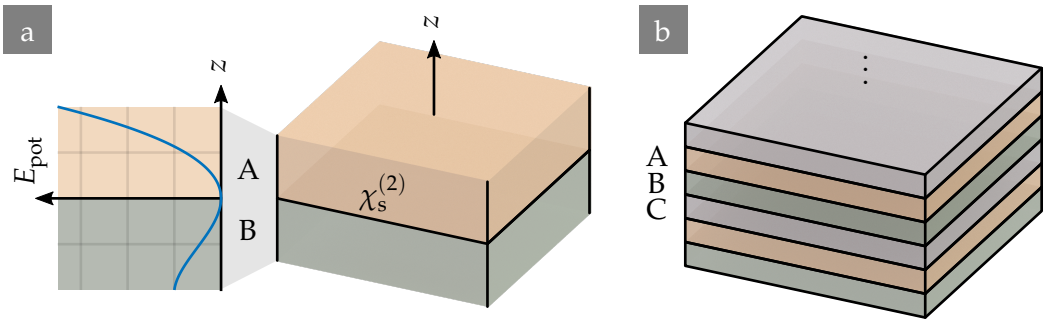

Figure 2.6: a) The interface between two homogeneous and centrosymmetric dielectric materials, denoted by A and B, shows a non-zero nonlinear surface susceptibility, $\chi_s^{(2)}$. It originates from breaking of the inversion symmetry at the interface and can be understood in terms of the anharmonic potential seen by the electrons. b) Scheme of a metamaterial made from three dielectric materials A, B, and C that exploits the local symmetry breaking at the individual interfaces to generate a bulk second-order susceptibility. The stacking order ("ABCABC...") provides a structure without inversion symmetry and ensures that neighboring interfaces do not interfere destructively as it would be the case for a material built from only two materials A and B.

restoring force on the electrons is nonlinear. That is exactly what happens at the interface between two materials as illustrated in Figure 2.6a. To arrive at an appreciable effective nonlinear susceptibility, $\chi^{(2)}$, the interfaces have to be densely packed and carefully arranged. Taking a scalar susceptibility as an example, one has to keep in mind that the nonlinear surface susceptibility that arises at the interface between material A and B has the same magnitude but the opposite sign of the surface susceptibility at the interface between B and A:

$$\chi_{s,AB}^{(2)} = -\chi_{s,BA}^{(2)}. \tag{2.38}$$

It is thus not enough to stack layers of two materials A and B on top of each other. The globally restored inversion symmetry in a system with a sequence given by "ABAB..."leads to a vanishing second-order nonlinear susceptibility. This problem is resolved by introducing a third constituent material as shown in Figure 2.6b. The resulting stapling sequence ("ABCABC...")

lacks inversion symmetry on a macroscopic scale and allows for an effective second-order susceptibility. A layer with thickness d contributes an effective susceptibility proportional to $1/d$ and, hence, the strength of the effective nonlinear susceptibility depends on the density of layers. Atomic-layer deposition is, therefore, the fabrication method of choice. It allows for the conformal deposition of dielectrics with a thickness that ideally is equivalent to one atomic monolayer. A more detailed description of the technique and its features is given in Section 3.1. This approach was implemented by two groups using the constituents HfO_2, TiO_2, and Al_2O_3 or In_2O_3, TiO_2, and Al_2O_3, respectively. The complete bulk second-order susceptibility tensor was determined with values of $\chi^{(2)}_{zzz} = 0.67\,\frac{\mathrm{pm}}{\mathrm{V}}$ and $\chi^{(2)}_{zzz} = 1.17\,\frac{\mathrm{pm}}{\mathrm{V}}$ for the largest element in the two respective material systems [102]. These values are comparable to the second-order susceptibilities of bulk nonlinear crystals, but still leave room for improvement. Therefore, another approach for the fabrication of second-order nonlinear materials grown by atomic-layer deposition will be developed and implemented in this work (see Section 4.1).

Chapter 3

3 Methods

This chapter gives an introduction to the most important fabrication and characterization methods utilized in this work. Atomic-layer deposition and 3D direct laser writing will be discussed first. These techniques are essential for the fabrication of nonlinear nanolaminates and 3D nanolaminateds photonic crystals. Subsequently, the setups and approaches used for both the linear and nonlinear optical characterization of the structures are presented. To arrive at a better understanding of the effects leading to the observed nonlinear optical response, additional information on the structural properties and the expected theoretical behavior are necessary. Therefore, the fundamentals of X-ray diffraction and the finite element method, with their respective implementations, are discussed in the last part of this chapter.

3.1 Atomic-Layer Deposition

Atomic-layer deposition (ALD) is a technique that is essential to the fabrication of the samples studied in this thesis. We will make use of its unique properties to both tailor a strong second-order nonlinear susceptibility in ALD-grown nanolaminate metamaterials and establish an easy route for the fabrication of 3D photonic crystals showing a second-order nonlinear response. In the following, the basic principles of ALD will be discussed with an emphasis on the deposition of ZnO and Al_2O_3 thin films. Subsequently, the used ALD reactor will be described and the recipes adapted for the growth on plane substrates and 3D polymer templates will be presented.

ALD is a vapor phase technique compatible with state-of-the-art complementary metal oxide semiconductor processes. It allows for the thin-film deposition of various materials including metals, oxides and nitrides on amorphous and crystalline substrates as well as on polymer and biological templates [103]. This facilitates a wide range of applications from microelectronics over photovoltaics to energy storage. New use cases in various industries emerge permanently [104]. ALD derives its unique properties from the sequential and self-limiting surface reaction of at least two reactants called precursors. The sample surface reacts with the precursor inserted into the reaction chamber until a monolayer has formed. Ideally, the surface is terminated at this point and no further reactions occur. This leads to the elimination of the influence of the gaseous precursor distribution and the thin film grows with identical rate on all surfaces. The deposition chamber is purged to remove the excess precursor and the reaction products before the next precursor is inserted. Subsequently, the chamber is once again purged and one so-called ALD cycle is completed. Repeating these steps over and over again results in the growth of continuous and pinhole-free films with a control of the thickness down to a single monolayer. Additionally, the process allows for conformal coating of nearly arbitrary 3D structures even for high aspect ratios [103]. These aspects are the main advantages of ALD as compared to other deposition techniques, such as physical or chemical vapor deposition.

The precursors have to fulfill a certain set of requirements to give a process with the properties mentioned above. It is crucial that the only contribution to film growth is given by the reaction of the precursor with the unterminated surface sites and not by unwanted side reactions of reactants or products. Additionally, each step has to lead to stable chemical species and terminate all surface sites in a given time span. Even for ideal precursors these requirements are only met for a certain temperature region usually called the ALD window. It is characterized by a growth per ALD cycle that is constant with respect to small temperature variations. Processes run outside this regime are often hard to control, lead to the loss of conformality, and an inferior film quality. On the low temperature side the ALD window is limited by the condensation of precursor on the substrate or incomplete reactions due to insufficient activation energy. Going to high temperatures the decomposition of chemical species in the chamber, *e.g.*, of the precursor or the surface molecules, into products that can not be removed during purging, and the increased surface desorption pose a problem.

The nonlinear nanolaminate metamaterials we discuss in Section 4.1 are made from alternating layers of zinc oxide (ZnO) and aluminium oxide (Al_2O_3). In what follows, the precursors and reactions for both materials will be presented and a typical ALD process will be illustrated taking the deposition of ZnO as an example.

Deposition of Zinc Oxide and Aluminium Oxide Films

There exist a number of possible precursors for the growth of ZnO by means of ALD. The use of diethyl zinc (DEZ, $Zn(C_2H_5)_2$) and water (H_2O) is by far the most common as the reactants are readily available and result in a process with a wide ALD window [105]. Nevertheless, DEZ suffers from thermal decomposition at elevated temperatures in combination with prolonged exposure times [106]. Additionally, both the orientation of the crystallites and the electrical properties of the deposited ZnO films show a strong temperature dependence [107–111]. We will come back to these aspects when discussing the nonlinear nanolaminates in more detail. The

chemical equation describing one cycle of ZnO film growth is

$$\mathrm{Zn(C_2H_5)_2 + H_2O \longrightarrow ZnO + 2\,C_2H_6} \tag{3.1}$$

and has a reaction enthalpy of $\Delta H = -70\,\mathrm{kcal}$ [103]. Due to the sequential nature of ALD each cycle consists of a binary sequence that can be split into two half-reactions illustrating the processes that take place at the surface for the individual precursors [112]

$$\mathrm{\underline{R}{-}OH + Zn(C_2H_5)_2 \longrightarrow \underline{R}{-}O{-}Zn(C_2H_5) + C_2H_6,} \tag{3.2}$$
$$\mathrm{\underline{R}{-}O{-}Zn(C_2H_5) + H_2O \longrightarrow \underline{R}{-}O{-}Zn{-}OH + C_2H_6.} \tag{3.3}$$

In these equations $\underline{\mathrm{R}}$ denotes the remainder of the chemical species that is chemisorbed at the surface.

The ALD growth of Al_2O_3 from trimethylaluminum (TMA, $Al(CH_3)_3$) and water (H_2O) used as precursors results in amorphous films and is considered a model system [113]. This ideal growth behavior is ascribed to the highly efficient and self-limiting half-reactions with an extremely high overall reaction enthalpy of $\Delta H = -376\,\mathrm{kcal}$ [103]. Nevertheless, it shows a loss of chemisorbed surface species with increasing temperatures that results in a decline of the growth per ALD cycle [114]. The overall chemical equation for the deposition of Al_2O_3 is given by

$$\mathrm{2\,Al(CH_3)_3 + 3\,H_2O \longrightarrow Al_2O_3 + 6\,CH_4.} \tag{3.4}$$

It can be again subdivided into steps that occur sequentially and describe the surface reactions of the individual precursors

$$\mathrm{\underline{R}{-}OH + Al(CH_3)_3 \longrightarrow \underline{R}{-}O{-}Al(CH_3)_2 + CH_4,} \tag{3.5}$$
$$\mathrm{\underline{R}{-}O{-}Al(CH_3)_2 + 2\,H_2O \longrightarrow \underline{R}{-}O{-}Al(OH)_2 + 2\,CH_4.} \tag{3.6}$$

The deposition process itself involves more steps than illustrated by the chemical half-reactions given for ZnO and Al_2O_3. These additional steps serve the purpose of strictly separating the two precursors at any given time. We will discuss a typical sequence of steps in ALD based on the deposition of ZnO. The individual steps are sketched in Figure 3.1 and are as follows:

a) One starts out from a surface that is reactive with at least one of the precursors. In the given example the surface is covered with reaction sites in the form of hydroxyl groups ($-OH$).

b) By a process called pulsing the gaseous DEZ is introduced as the first precursor into the chamber. One of the ethyl groups ($-C_2H_5$) of the DEZ molecules reacts with a hydroxyl group at the surface to form gaseous ethane (C_2H_6). The Zn atom with the remaining ethyl group is now attached to the surface and, ideally, stays there without decomposing or desorbing. This half-reaction is described by Equation 3.2.

c) The precursor stays in the chamber for the exposure time $\tau_{\mathrm{exp,\,P1}}$ that has to be chosen such that all surface sites, *i. e.*, all $-OH$ groups, are saturated. It is crucial that the reaction is self-limiting and stops once all hydroxyl groups have reacted. The excess precursor, the products or any species that are formed from the former two should not react with or alter the molecules chemisorbed at the surface. At this point, the surface is filled with $Zn(C_2H_5)$ groups attached to the oxygen remaining from the hydroxyl group.

d) The reactor chamber is pumped till the reaction product (ethane) and the excess precursor (DEZ) are removed. For non-ideal processes this time can be prolonged to allow for condensed or physically adsorbed species to be removed from the chamber. This marks the end of the first half of the binary cycle completed. The surface sites have gone from being terminated by hydroxyl groups to a termination by ethyl groups.

e) In the next step, the second precursor, *i. e.*, water in the given example of ZnO deposition, is pulsed into the chamber. The H_2O molecules react with the ethyl groups attached to the Zn atoms at the surface to form gaseous ethane and leave behind a hydroxyl group at the surface-bound Zn atom (see Equation 3.3).

f) After the exposure time $\tau_{\mathrm{exp,\,P2}}$ the surface reaction should have reached completion and all surface sites should be terminated by hydroxyl groups as a result from the reaction with water molecules. By now one layer of ZnO has been deposited on all surfaces that were previously covered with hydroxyl groups and that have been exposed to the gaseous precursors.

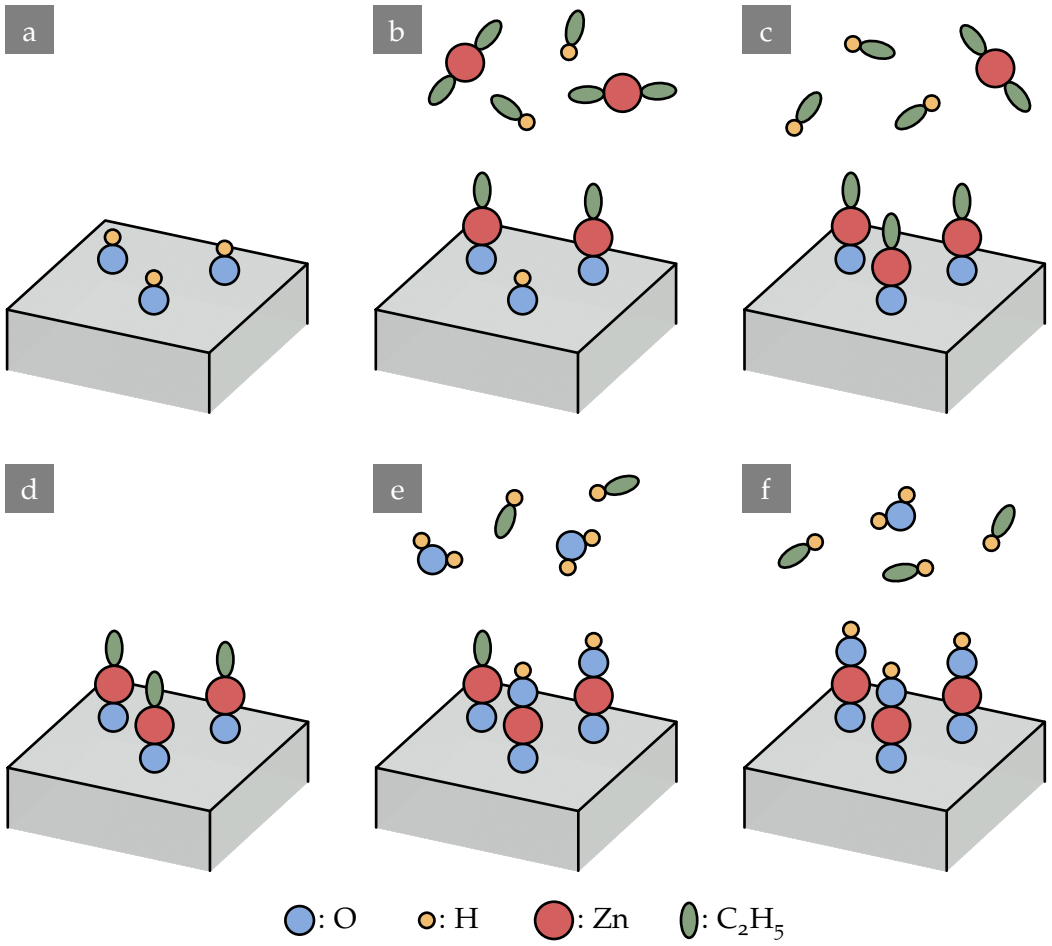

Figure 3.1: Scheme of one ALD cycle. The individual steps are depicted for the deposition of ZnO from DEZ and H_2O used as precursors. A detailed description of the process is given in the main text.

g) The reactor chamber is pumped till the reaction product and the excess precursor (ethane and water, respectively) are completely removed. With this, one full cycle is completed. The state is similar to the initial state depicted in Figure 3.1a except for one additional layer of ZnO that has been added beneath the hydroxyl groups. The deposition of the next layer is done by repeating the cycle given by steps b)-g).

An aspect of ALD that has not been covered so far is the initial stage of film growth providing the foundation necessary for the cyclic layer by layer

growth as it is described above. On regular substrates like glass or silicon wafers the process relies on a sufficient number of surface functional groups that are reactive with at least one of the utilized precursors. For the mentioned substrates these are usually hydroxyl groups (–OH) that are highly reactive with both DEZ and TMA. To make sure the surface is covered with a sufficient number of reactive sites one can, additionally, functionalize or activate it using an air plasma. The lack of a fair amount of hydroxyl groups leads to island growth and, thereby, hinders the deposition of a smooth and continuous film [115].

Aside from the deposition of ALD films on plane glass or silicon substrates, we are also interested in the conformal deposition on polymer templates. The processes involved in this case are slightly different. Obviously, the previously mentioned mechanism involving surface functional groups is still an important factor, but so are the diffusion of precursor molecules into the spaces between the polymer chains and the interaction with functional groups in the polymer backbone and side chains [116]. The exact mechanism and the resulting film properties depend on the involved polymer, the precursors, and the deposition parameters.

We will focus on the growth of Al_2O_3 from TMA and water used as precursors on polymer templates based on the monomer pentaerythritol triacrylate (PETA). Al_2O_3 has been found to reliably initialize film growth on various surfaces with a constant growth per cycle showing no nucleation delay as it is, for example, observed in ALD-grown ZnO films [117]. The monomer PETA has four functional groups. Three of those lead to cross-linking with other monomers molecules to form the polymer. The last one is a hydroxyl group that is available for reactions with TMA. In addition to this standard path, the precursor can also diffuse into the polymer network and get trapped there [118]. The subsequent pulsing of the second precursor leads to the formation of Al_2O_3 clusters close to the surface. Eventually, the individual clusters grown from the precursors that penetrated the polymer network and the ones grown at the sites of the hydroxyl groups coalesce and form a closed layer. This layer hinders further diffusion of the precursors into the polymer network and lays the foundation for the subsequent ALD cycles.

Therefore, utilizing ALD-grown Al_2O_3 as a seed layer will be the method of choice to ensure reproducible deposition on both conventional substrates and polymer templates.

ALD Reactor and Deposition Recipes

The ALD reactor used in this work is the commercially available Savannah 100 (Cambridge NanoTech) depicted schematically in Figure 3.2. It is based on a so-called viscous flow reactor where an inert carrier gas constantly flows through the evacuated reaction chamber towards the pump. We use argon (Ar) as the carrier gas. All the precursors described above have a vapor pressure at room temperature that is higher than the pressure in the reaction chamber. Hence, they can be simply dosed into the Ar flow by briefly opening (pulsing) the pneumatic valves ($V_{p,i}$) at the individual precursor containers i. The gaseous precursors are carried by the carrier gas and introduced into the reaction chamber through the inlet. The excess precursor and the products are, subsequently, removed from the chamber by the pump connected to the outlet. Various parts of the system can be heated to control the process temperature and avoid condensation of the chemical species. Independent temperatures can be set for the central part of the reaction chamber holding the substrate (T_{sub}), the outer rim of the chamber ($T_{chamber}$), the inlet piping between the precursor containers and the chamber (T_{in}), and the outlet piping connecting the chamber to the pump (T_{out}). A mass flow controller is used to regulate the flow of carrier gas given in standard cubic centimeters per minute (sccm) into the system. On the other side of the reaction chamber, right behind the outlet, a Pirani gauge monitors the pressure. It is followed by a stop valve (V_s) that allows disconnecting the pump from the reaction chamber.

The actual deposition of ALD films using the system described above is specified in a "recipe". It gives an application- and material-specific sequence of steps and process parameters for the deposition of ALD films. The necessity to adapt the recipe for a given use case can be illustrated by considering the deposition of ZnO on temperature sensible samples. On the

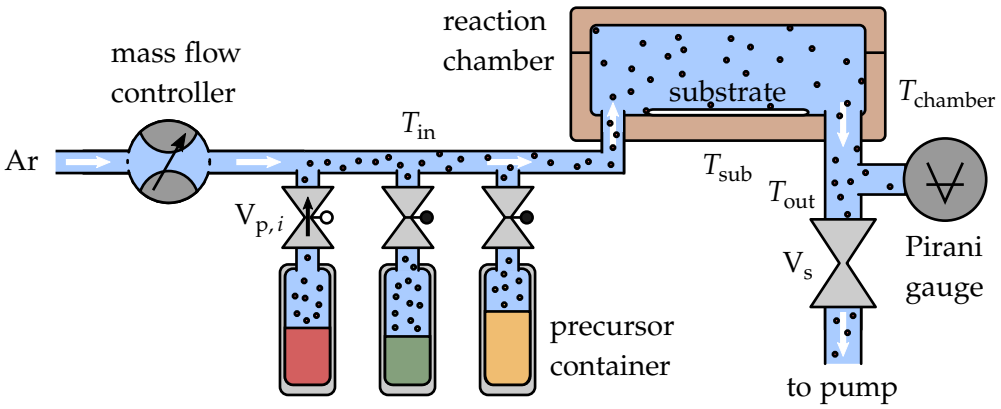

Figure 3.2: Scheme of the viscous flow reactor used in this work. Ar is used as inert carrier gas with its flow into the evacuated system regulated by a mass flow controller. The individual precursors can be dosed into the carrier gas by briefly opening the pneumatic valves, $V_{p,i}$. This way the reactants are introduced to the reaction chamber where they interact with the sample surface. Excess precursor and reaction products are removed by a pump that can be disconnected from the chamber using the stop valve, V_s. A Pirani gauge allows for online monitoring of the pressure in the chamber. Individual parts of the system can be heated to temperature T_i to avoid the condensation of chemical species and to control the reaction in the chamber.

one hand, one would try to deposit at temperatures chosen as low as possible to avoid damaging the sample. On the other hand, the low temperature leads to increased exposure times and altered properties of the deposited film. The recipes and process parameter we use for the deposition of ALD films on temperature insensitive, plain substrates and on temperature sensible, complex 3D polymer templates are presented in the following.

Recipe for Plain Films

When depositing films on plain and thermally stable substrates, we aim at short overall growth times allowing for large parameter sweeps as they will be used to optimize the nonlinear properties of the nanolaminates in Section 4.1.3. The short fabrication times will be achieved by depositing at an increased substrate temperature, T_{sub}, of 250 °C. The high temperature results in an enhanced diffusion and accelerated reaction kinetics allowing

for short exposure and pump times. The temperature of the other heatable parts will be set to $T_{in} = T_{chamber} = T_{out} = 150\,^{\circ}C$. The mass flow controller keeps the Ar flow constant at 20 sccm. An ALD half-cycle as it is shown in Figure 3.1a-d consists of the following two steps: First, the precursor valve, $V_{p,i}$, is briefly opened for $t_{pulse} = 15\,ms$ to pulse the gaseous precursor into the carrier gas flow. Second, a pause of 5 sec is introduced to allow for surface saturation and the subsequent removal of chemical species from the reaction chamber. These two steps are repeated for the complementary precursor and together the four steps form a complete cycle giving one layer of ZnO or Al_2O_3. In this recipe, the pump is permanently connected to the chamber. Nanolaminates can be easily fabricated by exchanging the pulses of DEZ for TMA pulses (or vice versa). The final thickness of the deposited film is controlled by adjusting the total number of full ALD cycles and can be estimated from the so-called bulk growth per cycle of the individual materials. The latter is determined from ellipsometry measurements on thick samples grown using the deposition parameters described above. Mean values of 0.19 nm/cycle and 0.12 nm/cycle are derived for the bulk growth per cycle of ZnO and Al_2O_3, respectively.

Recipe for 3D Polymer Templates

The deposition recipe becomes a little more sophisticated when coating 3D polymer templates (see Section 4.2.1). The main reason is the necessity to find a good balance of competing effects. We have to reduce the deposition temperature as compared to the plain films to avoid damaging the polymer templates. The downside of this measure is that both diffusion and reaction kinetics slow down. Nevertheless, we have to make sure that the precursors can penetrate the whole structure and reach the surface sites lying deep within. Additionally, the film growth on polymers relies on precursors diffusing into the polymer network. Therefore, we have to make sure that the polymer templates are exposed to the precursors for a sufficiently long time in order to compensate for the decreased temperature and to ensure a truly conformal film growth.

A temperature of 150 °C will be set for all parts of the ALD system, including

the substrate heater, when depositing films on 3D polymer structures. The Ar flow is initially set to 20 sccm. To prolong the exposure time of the sample to the precursors, we use half-cycles that are as follows: First, the stop valve, V_s, is closed, thereby, disconnecting the reaction chamber from the pump. Second, the precursor is pulsed by opening the precursor valve, $V_{p,i}$, for 15 ms. Third, the carrier gas flow is reduced to 5 sccm for a period of 5 sec using the mass-flow controller. Finally, the pump is reconnected, the flow is reset to 20 sccm and the reaction chamber is purged for 60 sec to remove excess precursor and reaction products. The complementary precursor follows the same half-cycle sequence and the complete cycle is repeated to control the final film thickness. This deposition scheme comes at the cost of longer fabrication times as compared to the plain film recipe, but results in undamaged polymer templates with a smooth and conformal coating (see Section 4.2.2). The bulk growth per cycle of ZnO and Al_2O_3 using this recipe is identical to the values determined for films grown with the plain film recipe (see above).

3.2 3D Direct Laser Writing

3D direct laser writing (DLW) is a fabrication technique that is essential to this thesis. It will be used to rapidly fabricate polymer photonic crystals that serve as templates for subsequent coating using ALD (see previous section). After a short overview of other fabrication approaches for 3D photonic crystals, 3D DLW will be considered in more detail. We will summarize the basics of radical photopolymerization and see why a nonlinear photoresist response is necessary for true 3D laser lithography. Motivated by experimental demands, a fruitful scheme to reduce polymer autofluorescence and at the same time increase resolution in DLW will be discussed. Finally, the 3D DLW setup used in this thesis will be presented.

The fabrication of 3D photonic crystals can be quite challenging. It demands for techniques that allow structuring of dielectric materials in three dimensions with a resolution that lies in the wavelength regime of the interacting light. These requirements have been met by a few approaches each with its own advantages and disadvantages [36]. Self-assembled colloidal crystals

and directional etching are just two examples that were successfully demonstrated, but are only applicable to certain geometries and, therefore, lack flexibility [119, 120]. Another approach is based on the idea to assemble the structures in a layer-by-layer manner. The individual layers can be fabricated by means of well established patterning techniques like for example electron-beam lithography in combination with etching. Subsequently, the structured layers are planarized using a filling material that gives a sufficient refractive index contrast or one that can be removed in the very last step [121]. At this point the next layer can be structured. Instead of planarizing the layer, one can, alternatively, stack two layers that are structured on a wafer and bond them. After removing the substrate this step can be repeated and, given a highly precise alignment of the individual layers down to a few tens of nanometers, results in high quality 3D photonic crystals [122]. With the layer-by-layer approach large refractive index contrasts and a relatively high flexibility are achievable. The downside lies in the time consuming nature of the process.

Another technique that can be used for the fabrication of 3D photonic crystals is 3D DLW. The nonlinear optical response of a suitably composed photoresist leads to multiphoton absorption and allows for the rapid fabrication of nearly arbitrary 3D structures in one single step. The most common implementation that was first proposed and demonstrated in 1996 relies on the third-order nonlinear effect of 2PA (see Section 2.3) [123]. Meanwhile, 3D DLW is a well-established technique that has been demonstrated to provide a resolution in the sub-micrometer regime and high-quality 3D photonic crystals [124, 125]. By means of a sophisticated combination of approaches including stimulated-emission-depletion inspired direct laser writing (STED-DLW) and a titanium dioxide double inversion using ALD, it was even possible to demonstrate a 3D photonic bandgap in the visible wavelength regime [126, 127].

Radical Photopolymerization

In DLW tightly focused laser pulses are used to locally alter the properties of a photoresist. A widely used scheme that we will call the standard ap-

proach is based on the radical polymerization of a negative-tone photoresist in combination with fs-pulses in the wavelength regime around 800 nm. Typically, the photoresist contains a monomer and a photoinitiator that is chosen according to the excitation wavelength. The absorption of light by the photoinitiator leads to the formation of radicals necessary to start the polymerization reaction. As a result of this reaction a polymer network, that is insoluble in the solvents used to wash away the remaining monomer, is created.

A typical radical photopolymerization involves the following four stages [128, 129]:

1. **Radical Formation.** The absorption of incident radiation causes the formation of a radical species denoted by $R^\bullet$. There exist various pathways for this step. Quite often it is intermediated by the excitation of a photoinitiator molecule, I,

$$I \xrightarrow{\hbar\omega} I^* \longrightarrow \ldots \longrightarrow R^\bullet. \tag{3.7}$$

2. **Chain Initiation.** The radical species, $R^\bullet$, attacks a monomer, M, and forms a monomer radical, $RM^\bullet$ that serves as the starting point of the polymer chain

$$R^\bullet + M \longrightarrow RM^\bullet. \tag{3.8}$$

3. **Chain Propagation.** More and more monomer molecules are added to the growing polymer chain

$$R\,(M)_n\,M^\bullet + M \longrightarrow R\,(M)_{n+1}\,M^\bullet. \tag{3.9}$$

   This results in a polymer that can no longer be dissolved once a certain degree of polymerization is achieved. For monomers that have more than one functional group, cross-linking between the individual polymer chains occurs and leads to a complex interwoven polymer network.

4. **Chain Termination.** One possible way the radical polymerization is stopped is by the reaction of two radicals. For example:

$$R_1\,(M)_n\,M^\bullet + R_2\,(M)_m\,M^\bullet \longrightarrow R_1\,(M)_{n+m+2}\,R_2. \tag{3.10}$$

Other possibilities to terminate the chain growth are through the formation of a stable radical that will not react any further or the transfer of a hydrogen atom between two chains to form a saturated and an unsaturated chain.

3D Structuring and the Nonlinear Photoresist Response

The local confinement of radical generation spatially limits the formation of a polymer network and can be used to "print"3D structures, but one has to be cautious. The details of radical formation, or to be more precisely, its dependence on the intensity of the excitation laser, plays a crucial role for the fabrication of 3D structures. We assume that a certain energy per volume given by the threshold dose, D_{th}, is necessary to form a sufficient number of radicals and ensure a degree of polymerization that withstands the solvents used in the development step following exposure. Additionally, we assume that the photoresist "remembers"the whole process and the exposure dose, D, is, therefore, proportional to the total intensity absorbed during the whole exposure. We will first have a look at photoresists that show a predominantly linear absorption (see Equation 2.23). The linear absorption coefficient, $\alpha(\omega)$, has to be sufficiently small to avoid the absorption of a large portion of the energy right at the beginning of the light path through the photoresist. The exposure dose, D, is linear in the excitation intensity, I, and given by

$$D(x, y, z) \propto I(x, y, z, t). \tag{3.11}$$

For a single point-wise exposure using a focused Gaussian beam the dose, D, can be chosen such that the relation $D(x, y, z) \geq D_{\text{th}}$ is only satisfied for a small region in the focus resulting in a polymerized volume often called a voxel. Nevertheless, problems with an exposure dose that is linear in the excitation intensity start arising as soon as one tries to fabricate complex connected structures: In the limiting case of exposing a plane that is perpendicular to the beam propagating along the z-direction, the total exposure dose becomes independent of the axial coordinate, *i. e.*, z, [36]. Instead of fabricating a xy-plane, one ends up with a block due to the constant exposure dose along the beam direction rendering 3D fabrication in one single step impossible.

The situation changes as soon as any kind of nonlinearity of order $N > 1$ is introduced in the photoresist response. Often this nonlinearity is given by multi-photon absorption of the photoinitiator with the standard DLW pathway of 2PA described by $N = 2$, but it can also have other origins [130]. The exposure dose is no longer linear in the excitation intensity. Instead it is described by

$$D(x, y, z) \propto I(x, y, z, t)^N. \tag{3.12}$$

If one again considers the previous example of the exposure of a xy-plane, the z dependence no longer drops out as long as $N > 1$ [36]. Therefore, more or less arbitrary 3D structures can be fabricated by moving the sample with respect to the laser focus or vice versa.

Reducing the Autofluorescence

In agreement with the necessity for a nonlinear photoresist response given above, the photoresist in the standard DLW approach based on an excitation wavelength, λ, around 800 nm consists of a monomer that shows negligible linear and nonlinear absorption for both λ and $\lambda/2$. Additionally, a photoinitiator that shows no absorption at the excitation wavelength, λ, but 2PA at $\lambda/2$ is used. However, there exist situations where the use of a photoinitiator in the photoresist is unpractical. Measuring the second-harmonic generated from structures based on DLW polymer templates is one of those. The reason lies in the strong photoresist autofluorescence that would interfere with the second-harmonic signal [131]. The autofluorescence is dominated by the photoinitiator contribution and even initiators that are supposed to have a very low fluorescence signal are problematic and a source of errors in the experiments presented in this thesis [132].

Fortunately, it turns out that by using fs-pulses at a significantly reduced excitation wavelength of 405 nm, the photoinitiator can be discarded altogether. The reason is that the double bonds present in the acrylate groups show a strong absorption for wavelengths shorter than 220 nm [133]. It has been demonstrated that a variety of acrylates can be photopolymerized without

an additional photoinitiator following linear absorption of photons from an excimer laser at 222 nm and the subsequent generation of radicals [134, 135].

The radical generation can also be triggered by nonlinear processes as they are necessary for 3D DLW. Using an excitation wavelength of 405 nm, where the linear absorption in the photoresist is very low, the monomer PETA was found to show a nonlinear response with $N = 1.61$ [136]. The non-integer value is attributed to contributions from different mechanisms like for example a contribution from linear absorption involved in the formation and termination of free radicals. The experiments were performed using an electronically pulsed laser diode with pulse durations in the ps regime. Throughout this thesis we will follow a related approach but turn to fs-pulses at 405 nm. The idea is to increase the dynamic range, *i. e.*, the relative range from threshold to damage dose of the process that was found to be limited in Reference [136]. Using short fs-pulses we can avoid overheating of the photoresist that otherwise leads to micro-explosions and a low damage dose. Therefore, this allows for higher stability during DLW and excellent results in terms of structure quality (see Section 4.2.2).

Resolution in 3D Direct Laser Writing

The operating wavelength of photonic crystals is determined by the achievable resolution of the utilized fabrication method. To be able to fabricate 3D woodpile photonic crystals with parameters envisioned in this work, it is necessary to increase the resolution as compared to the standard DLW configuration based on an excitation wavelength around 800 nm. One way to achieve this is by employing STED-DLW that was shown to provide a resolution beyond the diffraction limit [126]. Unfortunately, this approach is incompatible with the demand for a low autofluorescence signal from the polymer structures: The utilized photoinitiator 7-Diethylamino-3-thenoylcoumarin (DETC) that provides a working depletion pathway also shows a strong fluorescence signal in the wavelength range from 400 nm to 600 nm [137].

Another way to improve the resolution is the choice of a smaller fabrication wavelength, λ, as it is regularly done in the semiconductor industry.

The achievable resolution in 3D DLW can be expressed by a slightly modified Abbe diffraction limit that also shows to be in good agreement with numerical calculations based on the generalized Sparrow criterion [137]. The nonlinearity, N, results in an exposure-dose profile that is no longer proportional to $|\boldsymbol{E}|^2$ as in the case of purely linear absorption but to $|\boldsymbol{E}|^{2N}$. Assuming a Gaussian profile in both lateral (x, y) and axial (z) direction, the critical lateral distance, a_{xy}, for an objective lens with a given numerical aperture (NA) becomes

$$a_{xy} = \frac{\lambda}{2\mathrm{NA}\sqrt{N}}. \tag{3.13}$$

A similar expression for the critical axial distance, a_z, can be derived. It incorporates the fact that the focus is elongated along the axial direction by introducing the aspect ratio, AR, of the exposure volume and reads

$$a_z = \frac{\lambda \mathrm{AR}}{2\mathrm{NA}\sqrt{N}}. \tag{3.14}$$

A typical value for high-NA objective lenses is AR = 2.5 [137].

From Equations 3.13 and 3.14 it is quite evident that changing the excitation wavelength from around 800 nm to 405 nm is accompanied by a reduction of the critical distances by nearly a factor of two. This is the approach that we will follow in the setup discussed in the following section. Aside from the increased resolution, we profit from the simple photoresist formulation that dispenses with the photoinitiator that would lead to increased autofluorescence from the fabricated samples.

Experimental Setup for 3D Direct Laser Writing at 405 nm

The 3D DLW system we use for the fabrication of 3D photonic crystals is based on the highly automatized setup that was initially designed and assembled by J. Fischer with the help of J. Kaschke and J. Müller. It was modified from the former standard excitation wavelength of 810 nm and optimized for operation at the second-harmonic wavelength of 405 nm by the author and P. Müller. The following description will mainly focus on

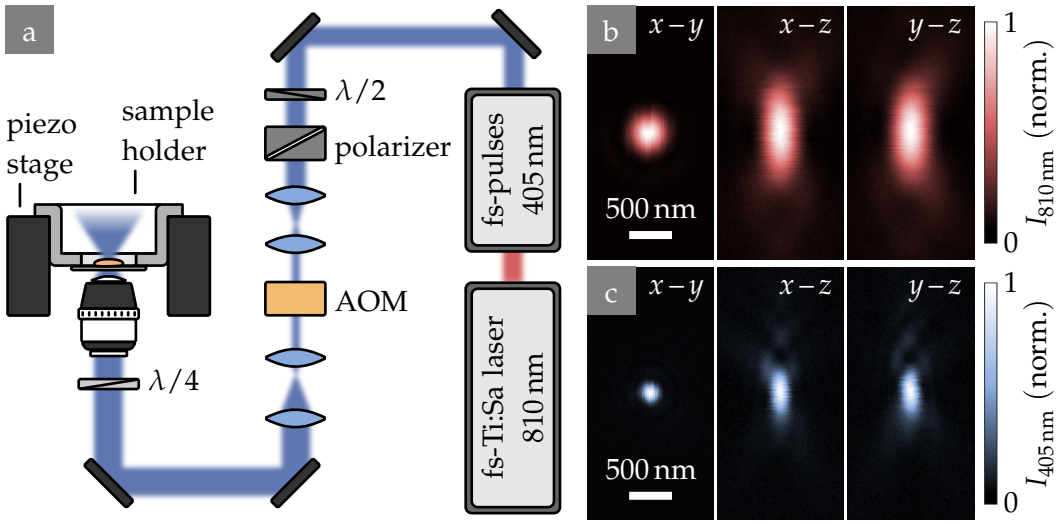

Figure 3.3: a) Main components of the setup used for 3D DLW. A mode-locked fs-Ti:sapphire oscillator is tuned to a center wavelength of 810 nm and frequency doubled to arrive at 405 nm fs-pulses used for excitation. The mean power going into the system is adjusted by means of a half-wave plate ($\lambda/2$) and a Glan-laser polarizer. An AOM controls the mean power during the writing process. The beam is converted from linear to circular polarization using a quarter-wave plate ($\lambda/4$) before it is tightly focused into the photoresist by a high-NA objective lens. The sample is mounted to a piezo stage and can be moved with respect to the focus. The setup is characterized by scanning a gold bead through the focus and collecting the backscattered signal. Panels b) and c) show the normalized intensity in different planes for a center wavelength of 810 nm and 405 nm, respectively. As expected the focus size is reduced by approximately a factor of two by going from the fundamental to the second-harmonic wavelength.

the aspects that differ from the previously used configuration. For a more detailed description of the latter please refer to Reference [138].

As mentioned earlier, the goal of an increased resolution is achieved by significantly decreasing the excitation wavelength, λ. To this end the output of the fs-Ti:sapphire oscillator (Spectra-Physics, MaiTai HP) is sent onto a second-order nonlinear crystal resulting in fs-pulses at a repetition rate of 80 MHz and a center wavelength of 405 nm (see Figure 3.3a). The mean laser

power is reduced by a combination of a half-wave plate ($\lambda/2$) and a Glan-laser polarizer. The beam passes an acousto-optic modulator (AOM), used to control the mean excitation power during fabrication, before being sent into an inverted microscope body. A quarter-wave plate ($\lambda/4$) converts the linear into a circular polarized beam that is focused by a high-NA oil immersion objective lens (Leica, HCX PL APO $100\times/1.4-0.7$ OIL CS). Using circular polarized light at the back-focal plane of the objective lens is essential to arrive at a electric field distribution in the focus that is rotationally symmetric around the propagation direction.

The setup can be characterized by measuring the focal intensity distribution using single gold beads (diameter $d = 80\,\text{nm}$) that are spin-coated on a substrate and covered by PETA. A 3D reconstruction of the intensity is derived from the backscattered signal collected while scanning a single gold bead through the focus. This way we can make sure that the change of wavelength indeed leads to the expected results and the setup is well aligned for fabrication. Figure 3.3b and c shows measurements of the focal intensity for an excitation wavelength of 810 nm and 405 nm, respectively. Both foci look good but also show some minor aberrations, *e. g.*, their shapes are not perfectly identical for the xz- and yz- planes as one would expect from an ideal focus that shows rotational symmetry around the z-axis. Additionally, the fact that the focus dimensions in x- and y-direction are not the same could hint at a slight digression from the desired circular polarization of the beam at the back-focal plane. The focus sizes for the two configurations are determined by fitting a 2D Gaussian to the individual slices. The mean FWHM values are summarized in Table 3.1. As expected from the considerations on resolution in 3D DLW, a decrease of the wavelength by a factor of two goes hand in hand with a focus that is smaller by the same factor and, therefore, facilitates the fabrication of 3D photonic crystals for shorter operation wavelengths.

This concludes the introduction to the two fundamental techniques used for sample fabrication in the scope of this thesis. ALD and 3D DLW provide the tools necessary to tailor film properties and deposit them conformally on costume made polymer templates. Details on the fabrication processes and the

	810 nm	405 nm	ratio ($\bullet_{810\,nm}/\bullet_{405\,nm}$)
x_{FWHM} (nm)	316	157	2.02
y_{FWHM} (nm)	335	165	2.03
z_{FWHM} (nm)	887	435	2.04

Table 3.1: Comparison of focus characteristics for center wavelengths of 810 nm and 405 nm. The focal intensity is derived from the signal backscattered from a single gold bead that is scanned through the focus. Subsequently, a 2D Gaussian is fitted to the data. The given FWHM values are averaged over the different measured planes as they are shown in Figure 3.3b and c. The ratio of the respective values at the two wavelengths are given in the last column and are very close to the expected value of two.

structural parameters of the nonlinear nanolaminates and 3D nanolaminated photonic crystals are given in Section 4.1.1 and 4.2.1, respectively. The following sections deal with the techniques used to characterize the fabricated samples and to get a better understanding of the underlying effects.

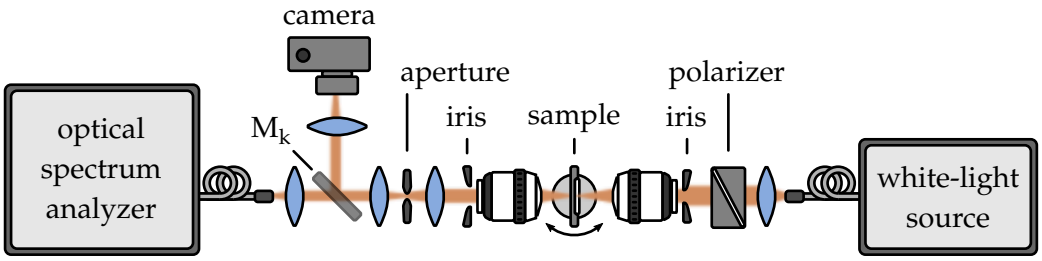

Figure 3.4: Setup used for the measurement of linear transmittance spectra. A fiber-coupled white-light source is linearly polarized and focused onto the sample by an objective lens. An identical objective lens is used to collect the transmitted light that is, subsequently, coupled into an optical spectrum analyzer. The spread of incidence angles can be reduced by an iris in front of the back-focal plane of the focusing objective lens. The investigated area on the sample is defined by an adjustable aperture that is placed in the intermediate image plane. A kinematic mirror, M_k, and a camera aid with the setup of the measured area.

3.3 Linear Optical Characterization

The linear optical characterization of the samples provides important information on the sample properties and their quality. The isotropic refractive index dispersion and thickness of the deposited ALD films are determined by fitting Cauchy's equation to ellipsometry data recorded with a Sentech SE 850. These parameters are necessary to control further sample iterations and also as an important input, for example, in the determination of the second-order susceptibility tensor.

Additionally, linear transmittance experiments are performed to study the quality and to determine the position of spectral features, like for example, stop bands, in both 3D photonic crystal templates and 3D nanolaminated photonic crystals. The linear transmittance spectra are measured using the setup depicted in Figure 3.4. A fiber-coupled white-light source (Energetiq, EQ-99 LDLS) is sent through a polarizer. The resulting light that is horizontally polarized is focused onto the sample by a NA = 0.4 objective lens. An iris diaphragm at the back-focal plane of the focusing objective

lens is used to reduce the effective numerical aperture and, thereby, limit the contribution by oblique incidence angles. The transmitted light is collected by another NA = 0.4 objective lens. The measurement area on the sample can be adjusted using an aperture that is placed in the intermediate image plane in combination with a kinematic mirror, M_k, and a camera. Once the sample is appropriately aligned and the investigated area is chosen, the kinematic mirror is removed and the transmitted signal is detected with a fiber-coupled optical spectrum analyzer (Ando, AQ-6315B). The recorded transmittance spectra are normalized to an identical measurement on the substrate right next to the structures.

3.4 Nonlinear Optical Characterization

The nonlinear optical characterization of the samples is a key aspect in this thesis. It provides quantitative measures for parameter optimization and allows for a deeper understanding of the underlying mechanisms. This section is divided into two parts. In the first part, the characterization of the nanolaminate metamaterials will be discussed. Here, the focus lies on the measurement of the generated second-harmonic power. The results are used to optimize the nanolaminates in terms of the layer sequence and the individual layer thicknesses. Subsequently, a different setup is used to determine the full second-order susceptibility tensor for the optimized nanolaminate. In the second part, the setup used for the characterization of 3D nanolaminated photonic crystals will be presented. The goal is to understand the spectral features arising from the interplay of nonlinear nanolaminate metamaterials and photonic crystals used as a template for conformal deposition.

Nanolaminate Metamaterials

The properties of the nonlinear nanolaminate metamaterials discussed in Section 4.1 depend critically on the exact layer sequence and thickness. Therefore, a large parameter sweep is necessary to study the impact of the individual parameters and to optimize the nonlinear metamaterial. In princi-

pal, the determination of the complete $\chi^{(2)}$ tensor for each of the grown films would be the perfect way to go. Unfortunately, this is not feasible due to the sheer number of samples and the effort involved in determining the tensor. Instead, we measure the generated second-harmonic power in the individual nanolaminates for a single combination of in and output polarization at a fixed angle of incidence. Subsequently, we normalize the detected power to the squared film thickness, and use this quantity as a figure of merit for the sequence optimization.

The setup utilized to measure both the mean fundamental and second-harmonic power is depicted in Figure 3.5. The fundamental wavelength is generated by a mode-locked Ti:sapphire (Ti:Sa) laser (Spectra-Physics, MaiTai HP) with a pulse duration of below 100 fs and a center wavelength of 800 nm. A half-wave plate ($\lambda/2$) and a Glan-laser polarizer are used to control the mean power. The polarizer is followed by an optical isolator that stops back reflections from interfering with the cavity mode or even damaging the laser. A small fraction of the x-polarized fundamental laser beam is reflected at a glass plate and detected with a Si photodiode. Having calibrated the photodiode with a power meter, allows for online monitoring of the mean fundamental power, P_ω, incident on the investigated sample. The main part of the laser power is focused onto the sample through a lens (L_1) with a focal length of $f_1 = 50$ mm. A stage that supports both translations and rotations of the sample allows for proper alignment with respect to the laser focus. The emerging beam containing both fundamental and second-harmonic signal is collected by the lens L_2 ($f_2 = 100$ mm). To get rid of the fundamental wavelength for the measurement, the signal is sent through two shortpass filters (Thorlabs, FESH0700) with a cut-off wavelength of 700 nm. Finally, the second-harmonic signal is detected using a photomultiplier tube (PMT, Hamamatsu, R4332). The signal-to-noise ratio is improved by modulating the impinging signal with a chopper wheel (CW) and sending the signal detected by the PMT through a lock-in amplifier. With an appropriate calibration the voltage measured at the PMT can be translated into the generated second-harmonic power, $P_{2\omega}$.

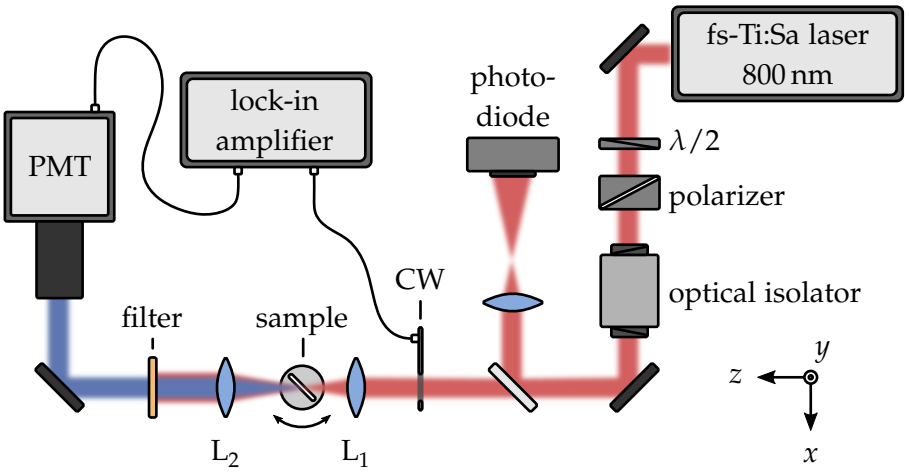

Figure 3.5: Setup used for the nonlinear characterization of nanolaminate metamaterials. A mode-locked Ti:sapphire laser tuned to a center wavelength of 800 nm is used to generate fs-pulses. The mean power is adjusted by a half-wave plate ($\lambda/2$) and a polarizer. An optical isolator is used to ensure that reflections in the setup cannot return to the laser. The mean power, P_ω, of the x-polarized fundamental beam is measured with a calibrated photodiode. Lenses L_1 ($f_1 = 50\,\text{mm}$) and L_2 ($f_2 = 100\,\text{mm}$) are used to focus and collect the light incident on and emitted from the sample, respectively. The sample itself is mounted on a stage that allows for both translations and rotations to enable the proper positioning with respect to the laser focus. Two shortpass filters are used to block the fundamental and only allow the second-harmonic wavelength onto the PMT. To increase the signal-to-noise ratio a lock-in amplifier is used to evaluate the signal stemming from the PMT. The incident fundamental beam is modulated by a chopper wheel (CW) positioned in the beam path right in front of lens L_1.

The setup described above is a good starting point to get an idea of the nonlinear response, but, obviously, it does not suffice to determine all elements of the second-order susceptibility tensor. There are numerous approaches that can be used to deduce the full tensor. Two techniques that are especially suitable for thin films as they are investigated in this thesis were compared in Reference [102]. It was shown that the tensor elements for identical samples determined by the two approaches are in very good agreement and, therefore, both seem to be a viable choice. One of the approaches relies on the interference of the second-harmonic generated from the investigated

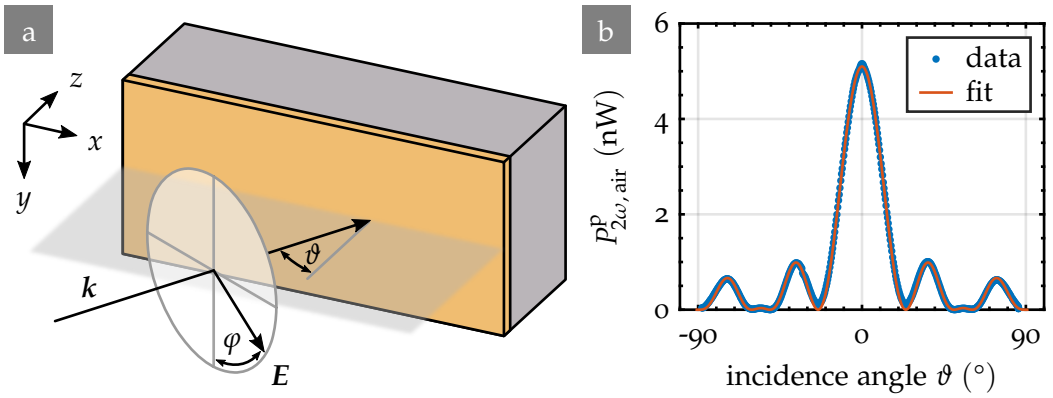

Figure 3.6: a) Measurement scheme for the determination of the second-order susceptibility tensor of nanolaminate metamaterials. A fixed angle of incidence, ϑ, is used. The orientation of the linearly polarized electric field vector of the fundamental beam is described by the angle φ and varied during the measurement. b) The setup utilized for the determination of the second-order susceptibility tensor is calibrated with a Maker-fringe measurement on a quartz plate for $\varphi = 90°$ (p-polarization). A typical measurement gives the transmitted p-polarized second-harmonic power in air, $P^{p}_{2\omega,\,air}$, as a function of the incidence angle, ϑ. The setup parameters are determined by fitting a model based on the well-known second-order susceptibility tensor of quartz to the measured data.

thin film with the second-harmonic originating from the interface between the backside of the substrate and air under varying angle of incidence. For increasing second-harmonic power generated in the nonlinear film, this approach tends to be unsuitable as the signal generated at the substrate-air interface becomes negligible and does not provide a sufficient modulation of the detected signal.

In contrast to that, the second technique that was first described in Reference [95], possesses no limitations of that kind and will be used in this work with some minor improvements that are discussed below. The approach is based on the measurement of the second-harmonic power for a fixed angle of incidence, ϑ, but varying orientation of the linear electric field polarization described by the angle φ (see Figure 3.6a). This minimizes errors originating from a misalignment of the focus with respect to the thin film as it may occur in measurement schemes based on the variation of the angle of incidence.

To fully determine the second-harmonic susceptibility tensor, the generated second-harmonic signal is detected for both the polarization perpendicular and parallel to the plane of incidence (s- and p-polarization, respectively).

Subsequently, the measured data for s- and p-polarization is fitted by a theoretical model that is derived by extending the expressions given by Herman and Hayden to arbitrary linear polarization orientations [95, 139]. The model describes the generated second-harmonic for a system that consists of a nonlinear thin film, a substrate, and air. The inhomogeneous wave equation (see Section 2.1) is solved in the individual materials taking into account the boundary conditions at the interfaces. For all calculations presented in this thesis we will neglect the reflections of the second-harmonic wave at the boundary between air and the nonlinear film. This approximation was suggested by Herman and Hayden as the effect of the reflections is small compared to the typical measurement errors and allows for a drastic simplification of the final expression [139]. For a fundamental beam with polarization angle φ that is incident at an angle ϑ from the side of the nonlinear film, the transmitted s/p-polarized second-harmonic power in air, $P^{\mathrm{s/p}}_{2\omega,\mathrm{air}}$, is given by

$$\begin{aligned} P^{\mathrm{s/p}}_{2\omega,\mathrm{air}} = {} & \chi^{(2),\mathrm{s/p}}_{\mathrm{eff}}(-2\omega;\omega,\omega) P^2_\omega \left(\frac{\omega}{c_0} L\right)^2 \operatorname{sinc}(\Psi)^2 \\ & \times \frac{2\left(\left(\sin(\varphi) t^{\mathrm{p}}_{\omega,\mathrm{a\text{-}f}}\right)^2 + \left(\cos(\varphi) t^{\mathrm{s}}_{\omega,\mathrm{a\text{-}f}}\right)^2\right)^2 \left(t^{\mathrm{s/p}}_{2\omega,\mathrm{f\text{-}s}}\, t^{\mathrm{s/p}}_{2\omega,\mathrm{s\text{-}a}}\right)^2}{c_0 \varepsilon_0 A \left(n_{2\omega,\mathrm{f}} \cos(\vartheta_{2\omega,\mathrm{f}})\right)^2}. \end{aligned} \tag{3.15}$$

The first line is very similar to the second-harmonic intensity that was derived previously in Equation 2.27. The second line introduces effects due to the incidence angle and orientation of polarization. The superscript s/p indicates perpendicular/parallel polarization with respect to the plane of incidence. The Fresnel transmission coefficients for frequency i, s/p-polarization, and at the given interface between the media n and m, where m and n can be a(ir), f(ilm), and s(ubstrate), are denoted by $t^{\mathrm{s/p}}_{i,\mathrm{m\text{-}n}}$. A is the focus area, P_ω the fundamental power, L is the thickness of the nonlinear film, and $n_{i,\mathrm{f}}$ its refractive index at frequency i. Both the film thickness, L, and the refractive index dispersion are taken from ellipsometry measurements modeling the material

properties using Cauchy's equation. $\chi_{\mathrm{eff}}^{(2),\mathrm{s/p}}(-2\omega;\omega,\omega)$ denotes the effective second-order susceptibility for the given second-harmonic polarization and will be discussed in more detail below. The linear polarization orientation of the fundamental beam is defined such that $\varphi = 0°$ and $\varphi = 90°$ corresponds to s- and p-polarization, respectively. The propagation angle in the nonlinear film, $\vartheta_{i,\mathrm{f}}$, at frequency i is given by Snell's law as $\sin(\vartheta_{i,\mathrm{f}}) = \sin(\vartheta)/n_{i,\mathrm{f}}$. $\Psi = \phi_\omega - \phi_{2\omega}$ is calculated from $\phi_i = \omega/c_0 \cdot n_{i,\mathrm{f}} \cos(\vartheta_{i,\mathrm{f}})$.

The actual form of the effective susceptibility, $\chi_{\mathrm{eff}}^{(2),\mathrm{s/p}}(-2\omega;\omega,\omega)$, is determined by the excitation conditions and the non-zero elements of $\chi^{(2)}$. The latter can be deduced from the inherent symmetries of the investigated system. We will study nanolaminates that derive their nonlinear properties from ZnO that typically crystallizes in the wurtzite structure. It belongs to the crystal class $6mm$ (or C_{6v} in Schoenflies notation) which has a 6-fold rotation axis and, additionally, 6 mirror planes that contain the rotation axis. This crystal class can be shown to have a second-order susceptibility tensor with four independent non-vanishing elements given by [6]

$$\begin{aligned}
&\chi_{xxz}^{(2)}(-\omega_\sigma;\omega_1,\omega_2) = \chi_{yyz}^{(2)}(-\omega_\sigma;\omega_1,\omega_2),\\
&\chi_{xzx}^{(2)}(-\omega_\sigma;\omega_1,\omega_2) = \chi_{yzy}^{(2)}(-\omega_\sigma;\omega_1,\omega_2),\\
&\chi_{zxx}^{(2)}(-\omega_\sigma;\omega_1,\omega_2) = \chi_{zyy}^{(2)}(-\omega_\sigma;\omega_1,\omega_2), \text{ and}\\
&\chi_{zzz}^{(2)}(-\omega_\sigma;\omega_1,\omega_2).
\end{aligned} \tag{3.16}$$

Furthermore, when considering second-harmonic generation permutation symmetry leads to a further reduction of the number of independent elements from four to three

$$\begin{aligned}
&\chi_{xxz}^{(2)}(-2\omega;\omega,\omega) = \chi_{yyz}^{(2)}(-2\omega;\omega,\omega) = \chi_{xzx}^{(2)}(-2\omega;\omega,\omega) = \chi_{yzy}^{(2)}(-2\omega;\omega,\omega),\\
&\chi_{zxx}^{(2)}(-2\omega;\omega,\omega) = \chi_{zyy}^{(2)}(-2\omega;\omega,\omega), \text{ and}\\
&\chi_{zzz}^{(2)}(-2\omega;\omega,\omega).
\end{aligned} \tag{3.17}$$

It is worth mentioning that Kleinman symmetry, *i. e.*, the assumption of a vanishing nonlinear susceptibility dispersion in the considered wavelength

regime, was not exploited to arrive at this point.

The ALD-grown ZnO films are not crystalline but rather consist of small crystalline domains, *i. e.*, they are polycrystalline. Nevertheless, we will show that characterizing the nonlinear nanolaminates based on a model with the nonlinear susceptibility elements given by Equations 3.17 results in an excellent agreement between theory and measurement. The reason this works so well is that textured films are well described by the symmetry class ∞m (or $C_{\infty v}$ in Schoenflies notation) [140]. They have an infinite number of mirror planes containing the axis of rotation and a form of the second-order susceptibility tensor that is identical with that of crystal class $6mm$.

Keeping these considerations in mind, the effective second-order susceptibility for the process of second-harmonic generation in both crystal class ∞m and $6mm$ can be expressed as given in Reference [95]

$$\begin{aligned}
\chi_{\mathrm{eff}}^{(2),\mathrm{p}} = &-\frac{1}{2}\chi_{xzx}^{(2)}\cos(\vartheta_{2\omega,\mathrm{f}})\sin(2\vartheta_{\omega,\mathrm{f}})\sin(\varphi_{\mathrm{f}})^2 \\
&-\frac{1}{2}\chi_{zxx}^{(2)}\sin(\vartheta_{2\omega,\mathrm{f}})\left(\cos(\vartheta_{\omega,\mathrm{f}})^2\sin(\varphi_{\mathrm{f}})^2+\cos(\varphi_{\mathrm{f}})^2\right) \\
&-\frac{1}{2}\chi_{zzz}^{(2)}\sin(\vartheta_{2\omega,\mathrm{f}})\sin(\vartheta_{\omega,\mathrm{f}})^2\sin(\varphi_{\mathrm{f}})^2, \\
\chi_{\mathrm{eff}}^{(2),\mathrm{s}} = &-\frac{1}{2}\chi_{xzx}^{(2)}\sin(\vartheta_{\omega,\mathrm{f}})\sin(2\varphi_{\mathrm{f}}).
\end{aligned} \tag{3.18}$$

The frequency argument $((-2\omega;\omega,\omega))$ was omitted for the sake of readability. φ_{f} denotes the polarization orientation of the fundamental beam in the nonlinear film and is given by

$$\tan(\varphi_{\mathrm{f}}) = \frac{t_{\omega,\mathrm{a\text{-}f}}^{\mathrm{p}}}{t_{\omega,\mathrm{a\text{-}f}}^{\mathrm{s}}}\tan(\varphi). \tag{3.19}$$

The setup we use for the determination of the second-order susceptibility tensor elements is very similar to the one shown in Figure 3.5 and is described in more detail in Reference [95]. Additionally, a complete derivation of the presented theoretical model can be found there.

A drawback of the approach presented so far is its reliance on setup specific parameters like the fundamental power and the spot size on the sample. The uncertainties accompanied by the determination of these quantities can be easily eliminated by performing a Maker-fringe calibration measurement for the given setup. We use a 100 µm thick y-cut quartz plate that has a well-known second-order susceptibility tensor with the dominant element $\chi^{(2)}_{xxx} = 0.6\,\mathrm{pm/V}$ [141]. The detected p-polarized second-harmonic power for an identically polarized incident fundamental beam with a mean power of 100 mW is fitted to the theoretical expressions given by Herman and Hayden [139]. A typical calibration measurement and the respective fitted theoretical curve are depicted in Figure 3.6b. With this modification to the previously described scheme we are able to determine the second-order susceptibility tensor of nonlinear thin films without having to rely on setup-dependent values.

3D Nanolaminated Photonic Crystals

The characterization of 3D nanolaminated photonic crystals presented in Section 4.2 focuses on aspects that are different from the ones considered for nonlinear nanolaminates. Whereas the goal for the latter is on quantifying the effective nonlinear material parameters to allow for a comparison with well-established nonlinear crystals, our emphasis when investigating 3D nanolaminated photonic crystals is on the interplay of nonlinear nanolaminates and photonic crystal templates. How does the spatial arrangement of the second-order susceptibility enforced by the polymer template influence the second-order nonlinear response of the resulting structure?

The properties of a photonic crystal with fixed geometrical parameters strongly depend on the considered wavelength. Therefore, it only seems natural to study the nonlinear response of 3D nanolaminated photonic crystals for various center wavelengths of the fundamental beam. For a correct comparison of the effects at different wavelengths, the wavelength-dependent setup properties like for example, the mean fundamental power, the pulse length, the transmittance and reflectance of the individual components, and also the dispersive properties of the nonlinear metamaterial itself have to

be determined. A way to get around the uncertainties arising from the determination of these parameters is to measure the nonlinear response of the nanolaminated photonic crystals relative to the response of the plain nonlinear nanolaminate measured right next to the structure. This way all wavelength-dependent effects are automatically taken into account. By performing this measurement for each sample we can, additionally, eliminate batch to batch fluctuations in the properties of the ALD-grown films and long-time fluctuations of the laser properties. Due to the symmetry properties of the grown films, the second-harmonic generated for a normally incident fundamental, *i. e.*, $\vartheta = 0°$, (see Figure 3.6), is zero. Therefore, we choose an angle of $\vartheta = 45°$ for the reference measurements. The 3D nanolaminated photonic crystals are, nevertheless, excited at an incidence angle of $\vartheta = 0°$.

When it comes to the measurement of the generated second-harmonic signal, we are interested in both its spectral distribution and its emission angle. The wavelength-sensitive detection allows confirming the source of the signal and eliminating possible errors due to, for example, fluorescence light stemming from the setup components or the polymer. To this end, a spectrometer will be used to analyze the generated signal. Dealing with photonic crystals with a lattice constant that is smaller than the wavelength of the second-harmonic signal, inevitably leads to the emission into various diffraction orders. The information on the contribution of the generated second-harmonic to different diffraction orders is retained by imaging the back-focal plane of the objective lens that is used to collect the signal onto the entrance slit of the spectrometer.

The setup used for the characterization of 3D nanolaminated photonic crystals is depicted in Figure 3.7. A mode-locked fs-Ti:sapphire oscillator (Spectra-Physics, MaiTai HP) generates pulses with a center wavelengths that is adjustable in the range from 800 nm to 1020 nm. The pulse duration depends on the chosen wavelength and is below 100 fs. The mean power is controlled by a combination of a half-wave plate ($\lambda/2$) and a Glan-laser polarizer. To avoid back reflections, especially for measurements at normal incidence, from disturbing the operation or damaging the laser, an optical

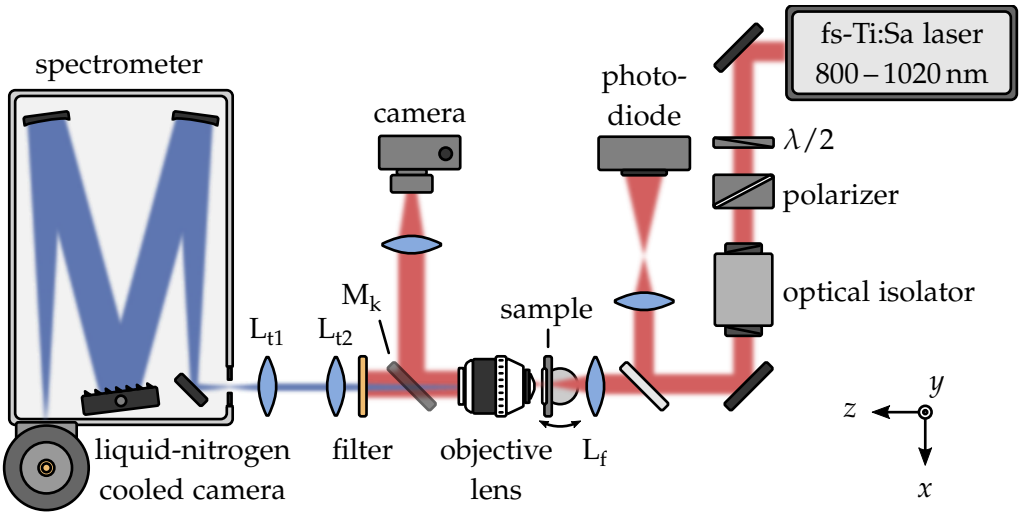

Figure 3.7: Setup for the spectral nonlinear optical characterization of 3D nanolaminated photonic crystals. A mode-locked fs-Ti:sapphire laser is used to generate the beam at the fundamental wavelength. For a typical measurement the center wavelength is tuned between 800 nm and 1020 nm. The mean power is regulated by means of a half-wave plate ($\lambda/2$) and a Glan-laser polarizer. An optical isolator hinders reflected power from returning to the laser. A small fraction of the incident power is reflected at a glass plate and is detected using a calibrated photodiode. This way the fundamental power, P_ω, can be monitored online. The beam is focused onto the sample using the lens L_f with a focal length of 50 mm. An objective lens with NA $= 0.75$ is used to collect the diffraction orders of the generated second-harmonic. The structure to be investigated can be aligned with respect to the focus using the stage and a camera. The illumination beam path is not depicted. Two shortpass filters block the fundamental beam. The lenses L_{t1} and L_{t2} are used to image the back-focal plane of the objective lens with a magnification of 0.25 onto the spectrometer slit. The signal entering the spectrometer is sent onto a grating and, subsequently, imaged onto a liquid-nitrogen cooled charge-coupled device camera for detection. The spectrometer measurement modes and the respective data imaged onto the camera are described in the main text and illustrated in Figure 3.8.

isolator is used. A small fraction of the beam is reflected at a glass plate and sent onto a calibrated Si photodiode for the online measurement of the mean fundamental power, P_ω. The fundamental beam is focused onto

the sample using a lens with a focal length of 50 mm resulting in a focal $1/e^2$ beam diameter of approximately 40 µm. The sample is mounted on a stage that allows for rotations around the y-axis and translations in all directions. A dry objective lens (Zeiss, LD Plan-Neofluar 63 × /0.75) with a numerical aperture of 0.75 (maximum half-angle of 48.6°) and a focal length of 2.6 mm is used to ensure that at least the first diffraction order at the second-harmonic wavelength is collected. Using a kinematic mirror, M_k, that is removed during measurements and a monochrome camera allows for aligning the individual structures with respect to the incident excitation beam. The fundamental wavelength is filtered out using two shortpass filters (Thorlabs, FESH0700) with a cut-off wavelength of 700 nm. We use two lenses (L_{t1} and L_{t2}) to image the back-focal plane of the objective lens with a magnification factor of 0.25 onto the entrance slit of the spectrometer (Jobin Yvon, HR460). For polarization resolved measurements an additional Glan-Thompson polarizer followed by an achromatic half-wave plate (not depicted) can be inserted between the lens L_{t1} and the entrance slit of the spectrometer. This way one can make sure to measure just the selected polarization while at the same time avoiding measurement errors due to the polarization dependent diffraction grating efficiency. The light entering the spectrometer through the adjustable entrance slit is sent onto a grating with 300 lines/mm by a concave mirror and is afterwards imaged by another concave mirror onto a silicon-based charge-coupled device camera (Princeton Instruments, LN/CCD-1340/100-EB/1) connected to the output of the spectrometer. The camera is cooled by liquid-nitrogen and operated at a set temperature of −100 °C to allow for a high signal-to-noise ratio. The spectrometer is calibrated using the documented emission lines of a Hg (Ne) lamp.

A typical measurement involves the sweep over a set range of fundamental wavelengths with a spectrometer image taken for each excitation wavelength. Once the sample is manually aligned such that the investigated structure is in the focus of the fundamental beam, a computer is used to run the following automated procedure: The Ti:sapphire laser is tuned to the desired wavelength while the shutter is closed. After the specified wavelength is set, a pause is introduced to allow for the stabilization of the laser mode. The

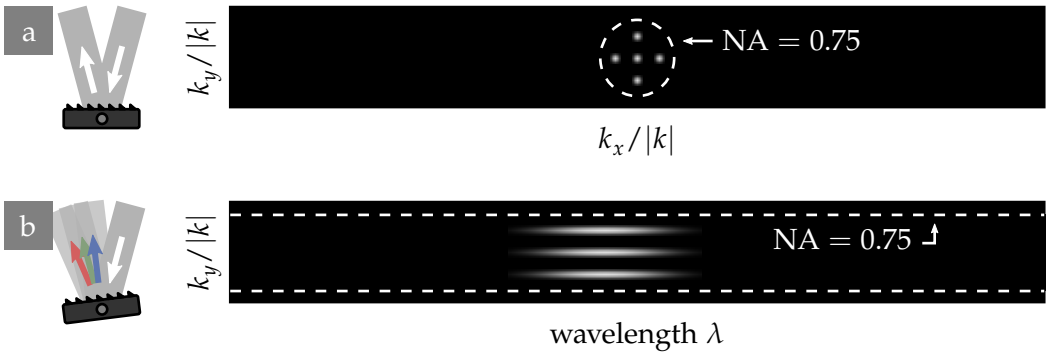

Figure 3.8: Illustration of the spectrometer operation modes sketching the grating configuration and the respective image on the charge-coupled device camera. a) The second-harmonic diffraction pattern in the back-focal plane can be directly imaged by rotating the spectrometer grating to its zeroth diffraction order and opening the spectrometer entrance slit to 2.2 mm. The axes show the reciprocal space, spectral information is not available. The field of view is indicated by the dashed line and is limited by the NA of the objective lens. b) Spectral information on the generated signal can be retrieved by rotating the grating to its diffraction order. The spectrometer slit needs to be closed to 300 µm to limit the diffraction orders in the x-direction to the zeroth order. The horizontal axis now shows the wavelength, λ, whereas, the vertical axis remains unchanged and still shows $k_y/|k|$. The field of view is again limited by the NA of the objective lens.

shutter is opened allowing for the excitation of the structure. With only a minimal safety delay a trigger signal is sent to the spectrometer and starts the exposure. After a specified exposure time t_{exp} the measurement stops and the shutter of the excitation laser is closed again with a small safety delay. The excitation wavelength, the mean fundamental power that was measured online, and the spectrometer image are stored. Subsequently, the whole procedure is repeated for the desired range of fundamental wavelengths.

There are two spectrometer measurement modes used to study 3D nanolaminated photonic crystals. With the spectrometer grating rotated to its zeroth diffraction order and the spectrometer slit fully opened to 2.2 mm, we record an image of the reciprocal space with k_x on the horizontal and k_y on the vertical axis (see Figure 3.8a). This allows for imaging of the whole diffraction

pattern collected by the objective lens but without any information on the wavelength. In the second scheme the grating is rotated to its diffraction order resulting in a hybrid image showing the wavelength on the horizontal and the reciprocal space on the vertical axis (see Figure 3.8b). This way we can study the spectra while still retaining some information on the individual diffraction orders. The entrance slit of the spectrometer has to be closed to a width of 300 µm to avoid mixing up the spectral and the spatial information by limiting the diffraction orders in the x-direction to the zeroth order.

3.5 X-Ray Diffraction

Using, X-ray diffraction (XRD) measurements, the structural properties of the deposited ALD films can be studied. The nonlinear optical properties of the nanolaminate metamaterials are determined by their structure and, therefore, this allows for a deeper understanding of the mechanisms that influence the optical material response (see Section 4.1.2).

XRD is based on the diffraction of electromagnetic radiation from periodic structures with a periodicity in the range of the interacting wavelength. To study the arrangement of atoms in a crystal with interatomic distances in the sub-nm regime, one has to use X-rays with a wavelengths that is of the same order. The observed phenomena are related to what was already discussed for photonic crystals in Section 2.5. X-rays are elastically scattered by electrons in the atoms that build up the investigated material. Scattering from the nuclei can be neglected due to the significantly higher mass resulting in a small amplitude of the scattered wave. Given a wave with wave vector $\boldsymbol{k}$ impinging on a specific sample, a large scattered field can be observed in characteristic directions denoted by the wave vectors of the outgoing waves $\boldsymbol{k}'$. For these directions that are determined by the Bragg or the Laue condition, the individual X-rays scattered at a set of crystal planes interfere constructively. This is given whenever the scattering vector, $\boldsymbol{q} = \boldsymbol{k}' - \boldsymbol{k}$, coincides with a reciprocal lattice vector, $\boldsymbol{G}$, of the investigated crystal [142]

$$\boldsymbol{k}' - \boldsymbol{k} = \boldsymbol{G}. \tag{3.20}$$

From a different point of view this can be interpreted as momentum con-

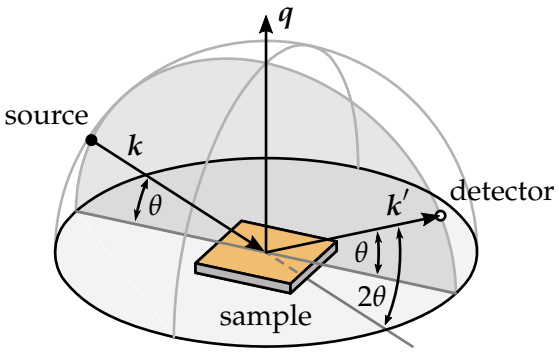

Figure 3.9: Scheme of a $\theta/2\theta$ measurement for the structural characterization of a thin film. X-ray source and detector are moved on the surface of a hemisphere that has the sample placed in its center. The wave vectors of the incoming and outgoing waves $\boldsymbol{k}$ and $\boldsymbol{k}'$, respectively, are adjusted such that they always enclose an identical angle θ with the sample surface. Consequently, the scattering wave vector, $\boldsymbol{q}$, is always parallel to the surface normal. The angle enclosed by $\boldsymbol{k}$ and $\boldsymbol{k}'$ is 2θ.

servation in the scattering process that is ensured through an additional momentum $\hbar\boldsymbol{G}$ provided by the crystal lattice. Studying the intensity for various incoming and outgoing wave vectors one can map out the reciprocal lattice and, thereby, determine the set of lattice planes that contribute to a certain intensity peak also called a Bragg peak. The actual intensity of the scattered wave depends on a variety of other things like the atomic and structural form factors of the considered material. It will not be discussed in detail as it is of minor relevance for the remainder of this thesis.

The information on the microstructure of thin films is often derived in $\theta/2\theta$ measurements as illustrated in Figure 3.9 [143]. In this scheme both the X-ray source and the detector are moved on the surface of a hemisphere with the sample placed at its center. The X-ray source defines the incident wavelength, λ, and the wave vector, $\boldsymbol{k}$, that is described by the angle θ measured with respect to the sample surface. The detector and, thereby, the outgoing wave vector, $\boldsymbol{k}'$, is adjusted to lie in the plane defined by $\boldsymbol{k}$ and the surface normal of the sample and enclose an angle of θ with the respect to the sample surface. The angles for incoming and outgoing wave vector $\boldsymbol{k}$ and $\boldsymbol{k}'$, respectively,

are kept identical throughout the measurement and enclose a total angle of 2θ . Due to the specifics of the $\theta/2\theta$ measurement, the scattering vector, $\boldsymbol{q}$, is always normal to the substrate and, therefore, only lattice planes that are parallel to the sample surface contribute to the measured signal.

Two further aspects have to be mentioned when dealing with polycrystalline thin films as it is the case for the measurements presented in this work. First, the scattered intensity for a fixed angle θ is not limited to a few points as for single crystals, but is spread on a circle due to the random orientation of the crystallites in the sample plane. Second, the peaks in the scattered intensity are broadened as compared to a single crystal sample. The reasons are the finite size of the domains that scatter coherently and microstrains that induce a variation of the local lattice constant. We will use a relation that was derived by P. Scherrer to estimate the mean crystallite size τ perpendicular to the substrate plane [144, 145]

$$\tau = \frac{0.9\lambda}{\Delta(2\theta)\cos(\theta)}. \tag{3.21}$$

Here λ is the X-ray wavelength, $\Delta(2\theta)$ denotes the FWHM of the peak given in radians, and θ is the Bragg angle the peak occurs at. Equation 3.21 has to be used with care as it is only valid for planes oriented along $(00l)$ directions with l being an integer. Furthermore, the broadening can not solely be attributed to finite crystallite size effects, but is also determined by microstrains and the instrument response. Nevertheless, Equation 3.21 is helpful in quantifying structural changes and will be used to estimate the lower limit for the size of the crystallites contributing to the (002) peak in the presented experiments.

In Section 4.1.2 a D8-Discover diffractometer (Bruker AXS GmbH) with Cu–K_α radiation is used for the $\theta/2\theta$ measurements in Bragg–Brentano geometry.

3.6 Finite Element Calculations

XRD measurements allow for deriving additional information on nonlinear nanolaminates and, thereby, supplement the optical measurements. To get a deeper insight into the effects leading to an enhanced second-harmonic generation in 3D nanolaminated photonic crystals, we will perform numerical calculations based on the finite element method (FEM). The results are compared with and complement the optical measurements. In this section, we will briefly summarize the basics of the FEM. A detailed introduction to the topic can be found in the literature. Subsequently, the specifics of the frequency-domain implementations used in this thesis will be discussed.

Many physical problems including the ones in electromagnetism can be described by partial differential equations (PDEs). Often these equations cannot be solved analytically and numerical methods, such as the FEM, come into play. One way to formulate the equations of interest is given by the so-called weak form that allows for a reduction of the differentiation order and, additionally, enables a straightforward implementation of boundary conditions [146]. Whereas the equation given by a PDE has to hold for each point individually, the integral equation used in the weak form "only"has to be fulfilled for the complete set of so-called test functions that are zero everywhere except for a small region and, thereby, sample a finite area in the investigated domain. To allow for a numerical solution of the problem, the equations given in the weak form are discretized on a given mesh that fills the whole domain. A very common approach is to expand the solution function in a basis that is identical with the set of test functions. This results in a system of N equations for the individual test functions describing the N unknown expansion coefficients. Boundary conditions can be implemented directly and introduce further coefficients and the same number of additional equations. By solving the system of coupled equations one derives the expansion coefficients and the solution function that approximates the solution of the PDEs on the prescribed mesh.

We use the FEM implemented in the commercially available software COMSOL Multiphysics to solve the inhomogeneous wave equation in frequency

domain (see Equation 2.17) describing the electromagnetic waves in the 3D nanolaminated photonic crystals. The structures are simulated from two different points of view. On the one hand, we look for eigenmodes that can be, in principle, coupled to for the given excitation conditions and compare their properties with the experimental findings. On the other hand, we try to mimic the experimental measurement based on a perturbative approach. Starting from plane waves that are incident on the structure, we determine the nonlinear polarization, and, finally, derive the generated wave at the second-harmonic frequency.

The essential properties of the simulated model for both approaches are more or less the same. In the lateral directions (xy-plane) the model consists of one square unit cell with an extent given by the rod spacing, a, in both x- and y-direction. Using periodic boundary (PB) conditions on the exterior boundaries with a surface normal in the xy-plane, results in a periodic structure with an infinite number of unit cells in the lateral directions. The exact form of the periodic boundary conditions depends on the eigenmodes that are supposed to be excited or the impinging plane wave. In general, one considers Floquet-Bloch periodic boundary conditions where the value of a function $u(x, y, z)$ that is shifted by arbitrary lateral unit cell vectors remains unchanged except for a phase shift. Therefore, the values of $u(x, y, z)$ and $u(x + a, y, z)$ on the periodic boundaries in the x-direction are connected by

$$u(x + a, y, z) = u(x, y, z)e^{ik_x a}, \tag{3.22}$$

where k_x is the x-component of the considered wave vector. Obviously, the same condition applies for the y-direction.

In the axial direction (z) a finite number of N_z unit cells with an axial lattice constant, c, is assumed. The woodpile photonic crystal is constructed from rods with an elliptical cross-section that are elongated along the axial direction due to the properties of 3D DLW (see Section 3.2.) A fixed ratio of the semiaxes, $r_z/r_x = r_z/r_y = 2.5$, that is typical for 3D DLW and which agrees well with the values obtained for the fabricated structures by means of focused-ion-beam milling, is used [126]. The whole photonic crystal is conformally covered by a single layer that represents the ALD-grown nonlinear

nanolaminate metamaterial. Its thickness, d_f, is equal to the total thickness of the deposited nanolaminate. This 3D nanolaminated photonic crystals is surrounded by air that extends into the $+z$- directions and is placed on a substrate that extends into the $-z$-direction. The model dimensions in axial directions are chosen such that the fields can be studied in the far field regime. The isotropic refractive indices of the individual materials are implemented with their respective dispersion relations. For the polymer and the nanolaminate it is described by the Cauchy equation with coefficients taken from Reference [147] (IP-L) and ellipsometry measurements, respectively. The dispersion of the glass substrate is modeled using the Sellmeier equation and data given for "D 263 T eco Thin Glass"(Schott AG). All further model properties specific to the individual calculations are discussed in the following two sections.

Eigenmode Calculations

In studying the eigenmodes of 3D nanolaminated photonic crystals, the goal is to identify possible sources of field enhancement in the structure. One example was given in Section 2.6 in terms of guided resonances found in photonic crystal slabs and periodically modulated waveguides. The Floquet-Bloch periodic boundary conditions are adjusted such that the resulting eigenmodes can be coupled to by a given incident plane wave with wave vector, $\boldsymbol{k}$. For example, eigenmodes that are calculated for $k_x = k_y = 0$ can potentially couple to a plane wave that is normally incident on the structure and so on. In contrast to the guided modes in a waveguide, the modes in 3D nanolaminated photonic crystals are not completely confined to the structure, but also couple to air and substrate modes due to the periodic modulation of the refractive index. To suppress reflections of these radiating parts of the modes in the air and substrate layers at the ends of the simulated domain, one can use open boundaries. Technically, these can be implemented through a so-called perfectly matched layer (PML) that absorbs the impinging wave in the PML region without reflecting it. Having set up the model in this way (see Figure 3.10a), we can compute eigenmodes of the 3D nanolaminated photonic crystals for a given frequency.

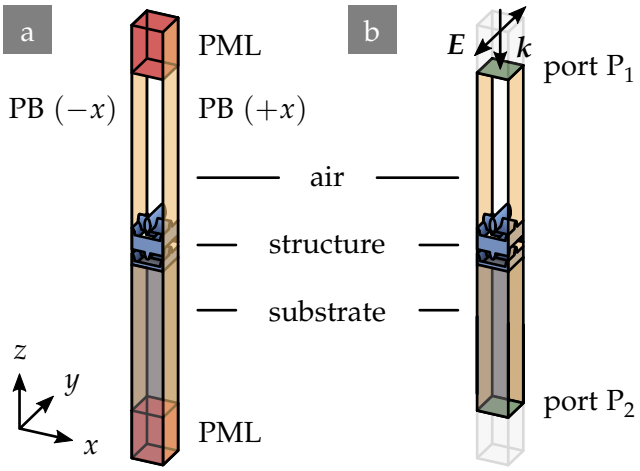

Figure 3.10: Illustration of the model used for the frequency-domain FEM. It consists of a substrate carrying the structure. The latter is built from a polymer that is conformally coated by a thin film. Air surrounds the structure and extends to the $+z$-direction. The periodic boundaries (PB) in x-direction are highlighted in orange. For the sake of clarity the ones in y-direction are not shown. a) Configuration as it is used for the eigenmode calculations and the calculations at the second-harmonic frequency. A PML is used at both ends of the domain along the z-direction to prevent reflections. b) Configuration used for calculations with a plane wave incident at the fundamental frequency. Port P_1 is used to excite the linearly polarized wave with wave vector $\boldsymbol{k}$ and electric field strength $\boldsymbol{E}$. Both P_1 and P_2 act as open boundaries for the given polarization and occurring diffraction orders.

Plane Wave Calculations

Performing the calculations for a plane wave at the fundamental frequency impinging on the 3D nanolaminated photonic crystals and generating a wave at the second-harmonic frequency, allows for a direct comparison of the calculated properties with the experimentally measured ones. In principle, one would have to solve a coupled set of equations describing the waves at both the frequencies just as in the example discussed for one dimension and a homogeneous material in Section 2.4. For a complex 3D structure this approach is quite time and resource consuming. However, like in the 1D case we can use the fact that the conversion efficiency from fundamental to

second-harmonic frequency is low and apply the undepleted pump approximation. This allows for a decoupling of the equations at the two frequencies and a step-wise solution of the problem.

We start by calculating the electromagnetic field that is caused by a linearly polarized incident plane wave at the fundamental frequency. To this end, port boundaries are used at both the air and the substrate end of the model (see Figure 3.10b). The ports allow for the excitation of a wave with a given polarization and, additionally, act as open boundaries for the specified polarization. Furthermore, they can be set up to show no reflections for the occurring diffraction orders in periodic structures. The periodic boundary conditions in the lateral directions are defined by the wave vector, $\boldsymbol{k}$, of the incident plane wave. The electromagnetic field distribution in the model is calculated by solving the inhomogeneous wave equation with a fundamental wave impinging from air that is excited by port P_1. Additionally, we can calculate both the transmission and the reflection of the structure at the specified frequency.

Given the field distribution at the fundamental frequency, we are, at least in principle, able to calculate the nonlinear polarization in the nonlinear layer used as a source term in the inhomogeneous wave equation at the second-harmonic frequency. Due to the conformal growth of the film the second-order susceptibility tensor has not only a nonuniform spatial distribution but also a nonuniform orientation throughout the structure. Therefore, the calculation of the amplitude of the second-order nonlinear polarization, $\tilde{\boldsymbol{P}}^{(2)}_{2\omega}(\boldsymbol{r})$, according to Equation 2.12 has to be performed with some caution and involves further steps. For reasons discussed in Section 4.1 the c-axis of the ZnO crystallites is assumed to be predominantly oriented perpendicular to the underlying Al_2O_3 layer and, therefore, parallel to the normal of the surface it is conformally grown on. Consequently, the second-order susceptibility tensor, that was determined for the c-axis parallel to the z-direction, has to be rotated such that the c-axis coincides with the local surface normal of the polymer template. For the symmetry properties of the given $\chi^{(2)}$, rotations of the tensor around the c-axis are irrelevant. Therefore, the same two angles that are used to describe the direction of the

surface normal are sufficient to describe the local orientation of the second-order susceptibility tensor. We choose the polar angle θ and the azimuthal angle φ like they are used in spherical coordinate systems for this purpose. The components of the third-rank tensor $\chi^{(2)}$ are transformed to the local coordinate system by two rotations. Each transformation is described by

$$\chi^{(2)'}_{ijk}(\boldsymbol{r}) = R^{(p)}_{il}(\alpha(\boldsymbol{r}))R^{(p)}_{jm}(\alpha(\boldsymbol{r}))R^{(p)}_{kn}(\alpha(\boldsymbol{r}))\,\chi^{(2)}_{lmn}(\boldsymbol{r}) \tag{3.23}$$

where the matrix $\boldsymbol{R}^{(p)}(\alpha(\boldsymbol{r}))$ denotes a rotation by an angle $\alpha(\boldsymbol{r})$ around the p-axis. The frequency argument of the susceptibility describing second-harmonic generation ($(-2\omega;\omega,\omega)$) was omitted for the sake of readability.

What remains is the derivation of the local surface normal with the corresponding rotation angles $\theta(\boldsymbol{r})$ and $\varphi(\boldsymbol{r})$. Another intermediate step is necessary to determine these angles. The reason is that the structures is build from intersecting basic elements that do not allow for an unambiguous determination of the surface normal by geometrical means. This step is based on modeling the heat transfer in the nonlinear layer. The outer surface of this layer is fixed to a temperature T_1 and the inner surface, in contact with the polymer template, is set to temperature a T_2 with $T_1 > T_2$. The temperature gradient, $\nabla T(\boldsymbol{r})$, given by the stationary solution of this physical problem is identical to the surface normal and, therefore, can be directly used to calculate the local rotation angles. With this additional information, the nonlinear polarization amplitude, $\tilde{\boldsymbol{P}}^{(2)}_{2\omega}(\boldsymbol{r})$, is fully defined. For technical reasons it is implemented in the form of the free current density, $\boldsymbol{J}_\mathrm{f}$. As can be seen from Equation 2.3 defining the source term by means of a free current density is identical to using the partial time derivative of the polarization. In frequency-domain the amplitude of the free current density oscillating at the second-harmonic frequency can be easily calculated and is

$$\left[\tilde{J}_{\mathrm{f},2\omega}(\boldsymbol{r})\right]_\mu = -i2\omega\cdot\tfrac{1}{2}\varepsilon_0\left[\chi^{(2),\mathrm{L}}(\boldsymbol{r})\right]_{\mu\alpha_1\alpha_2}\left[\tilde{E}_\omega(\boldsymbol{r})\right]_{\alpha_1}\left[\tilde{E}_\omega(\boldsymbol{r})\right]_{\alpha_2} \tag{3.24}$$

with the local second-order susceptibility tensor elements

$$\begin{aligned}\left[\chi^{(2),\mathrm{L}}(\boldsymbol{r})\right]_{\mu\alpha_1\alpha_2} = {} & R^{(z)}_{\mu i}(\varphi(\boldsymbol{r}))R^{(z)}_{\alpha_1 j}(\varphi(\boldsymbol{r}))R^{(z)}_{\alpha_2 k}(\varphi(\boldsymbol{r}))\\ & R^{(y)}_{il}(\theta(\boldsymbol{r}))R^{(y)}_{jm}(\theta(\boldsymbol{r}))R^{(y)}_{kn}(\theta(\boldsymbol{r}))\,\chi^{(2)}_{lmn}(\boldsymbol{r}).\end{aligned} \tag{3.25}$$

Finally, the inhomogeneous wave equation at the second-harmonic frequency, 2ω, is solved with the source term in the nonlinear film defined through the free current density (see Equation 3.24). As for the eigenmode calculations, PML at the end of the domain in the $+z$- and $-z$-direction are used to avoid reflections (see Figure 3.10a). We end up with the second-harmonic field distribution and are able to calculate the optical intensity from the monochromatic-wave amplitudes according to Equation 2.21.

Chapter 4

4 Results

In this chapter, the results achieved in the scope of this thesis will be discussed. The first part covers the design, fabrication, and characterization of second-order nonlinear nanolaminates made from alternating layers of ZnO and Al_2O_3. The influence of the individual parameters is studied by complementing the nonlinear optical measurements with data obtained from XRD. Finally, the nanolaminate layer sequence is optimized and the effective second-order susceptibility tensor of the thin film is derived. The second part of this chapter deals with 3D nanolaminated photonic crystals. These structures are fabricated by conformal deposition of the previously designed nanolaminates on 3D photonic crystals. The interplay of these two systems is studied experimentally by measuring the generated second-harmonic signal. Numerical calculations serve to complement the experimental data and allow for a better understanding of the dominant effects.

4.1 Second-Order Nonlinear Nanolaminates

This section deals with the design, optimization, and characterization of second-order nonlinear ZnO/Al_2O_3 nanolaminate metamaterials as they are discussed in Reference [148]. The idea was developed and the experiments were interpreted by the author and C. Kieninger with guidance from C. Koos and M. Wegener. The author fabricated all samples, performed the parameter sweeps to define an optimal cycle sequence, and studied the films by means of scanning electron microscopy (SEM). C. Kieninger measured the ellipsometry data and determined the elements of the effective second-order susceptibility tensor. Help with the structural characterization using XRD was provided by C. Sürgers. Scanning transmission electron micrographs and energy-dispersive X-ray maps were taken by S. Schlabach and X. Mu.

Probably the most important ingredient in nonlinear optical structures and devices is the material providing the nonlinear response. Its properties and the techniques necessary for its deposition or fabrication determine the range of possible applications. Whereas bulk crystals show the desired nonlinearity, they are hard to incorporate in integrated or compact optical systems. Here, nonlinear thin films deposited by well-established techniques provide a promising alternative. Focusing on materials that show a second-order nonlinear optical response and, at the same time, are compatible with thin film deposition, ZnO has gained a lot of attention due to its favorable properties [149]. In its bulk crystalline form ZnO has a wide-bandgap of 3.37 eV, is highly transparent in the visible wavelength regime, and shows a high thermal stability [150]. It crystallizes in the hexagonal wurtzite structure and shows an intrinsic n-doping that seems to be caused by defects that are formed during crystal growth [151]. From the variety of interesting properties, we are mostly interested in the optical nonlinearity of ZnO. The lack of inversion symmetry in the crystal structure leads to a second-order nonlinear response with the largest element of the susceptibility tensor in ZnO single crystals being $\chi^{(2)}_{zzz} = -14.31\,\frac{\mathrm{pm}}{\mathrm{V}}$ [152]. It was shown that this nonlinearity is also found in polycrystalline thin films grown by various techniques with the values of the second-order susceptibility tensor, $\chi^{(2)}$, sometimes even exceeding that in bulk [153–163].

Among the available ZnO deposition techniques, ALD is an interesting candidate. The growth of ZnO by means of ALD has been intensively studied and is well-established [105]. Additionally, the technique facilitates an easy incorporation of the deposited film in complex 3D structures and integrated optics. ALD allows for conformal deposition on nearly arbitrary templates with a thickness control down to an atomic monolayer and is compatible with state-of-the-art complementary metal-oxide-semiconductor processing. Despite the advantages of ALD for certain applications, there used to be no publications on the nonlinear optical properties of ALD-grown ZnO films prior to our work (see Reference [148]). In general, the number of second-order nonlinear materials fabricated by means of ALD is scarce and mainly based on an accumulated effect from interface susceptibilities in trinary nanolaminates where each constituent material shows a vanishing $\chi^{(2)}$ in the bulk (see Section 2.7) [95, 101]. This approach is fascinating from a physical point of view, but has its limits when it comes to the strength of the nonlinear response. Here, we will follow the straightforward approach of using a non-centrosymmetric material, *i. e.*, ZnO, with a non-vanishing $\chi^{(2)}$ from the start. The most important factors influencing the second-order nonlinear response in ZnO thin films will be discussed in the next section. Based on these findings we will suggest a material design and present the actual fabrication using ALD.

4.1.1 Design and Fabrication of Nonlinear Nanolaminates

Studying the literature on second-order nonlinearities in polycrystalline ZnO thin films deposited by various techniques, there seem to be two key factors influencing the performance: The orientation and the size of the ZnO crystallites.

The orientation of the ZnO crystallites has to exhibit a preferential direction throughout the whole film, otherwise, the interference of neighboring crystallites may lead to a decreased response or even its complete cancellation. The structural properties of a thin film are strongly influenced by the substrate it is deposited on. This influence also covers the orientation of the crystal-

lites. Usually, a growth mode with the optical axis of the ZnO crystallites (crystallographic *c*-axis) perpendicular to the substrate is desired for a strong second-order response [158]. Nevertheless, other schemes, like for example well-aligned crystallites having a preferential orientation with the *a*-axis perpendicular to the substrate, have been demonstrated for properly chosen substrates [160]. Unfortunately, the substrate influence decreases and stacking faults become more and more frequent with increasing film thickness. Therefore, a well-defined and stable orientation throughout the whole film is hard to achieve and a thickness dependence of the nonlinear properties is observed in ZnO thin films [154, 161, 163]. Interestingly, the growth of ZnO crystallites with a certain preferential orientation is not exclusively found on crystalline substrates. For ALD-grown thin films it was shown that an amorphous Al_2O_3 seed layer underneath the ZnO film fosters the growth of crystallites with their *c*-axis perpendicular to the surface and, at the same time, suppresses other orientations [164]. Aside from the choice of substrate, the crystallite orientation also strongly depends on the deposition parameters. ALD-grown ZnO films are predominantly oriented with their crystallite *c*-axes perpendicular to the substrate for deposition temperatures ranging from 220 °C to 300 °C [107]. On the contrary, this orientation is greatly suppressed for lower deposition temperatures in the range of 155–220 °C.

The size of the individual crystallites in the polycrystalline films is the second key factor. It was shown that the value of the second-order susceptibility can exceed that of bulk ZnO crystals and tends to decrease towards the bulk value for increasing crystallite size in thicker films [154, 163]. This behavior is explained by the strong contribution of crystallite boundaries and interfaces to the effective nonlinearity. Nevertheless, the ZnO crystallites have to be sufficiently distinct to show a bulk second-order susceptibility at all. Based on these considerations a sweet spot with respect to the crystallite size is expected. Therefore, we have to find a way to control the ZnO crystallite size in order to optimize the second-order nonlinear response. An easy way would be to just stop the film growth at a certain point, but obviously this approach is limited in terms of the achievable thickness and does not result in thickness independent effective optical properties. The crystallite size

and surface morphology of materials deposited by ALD, can be tuned by introducing an intermediate layer of a different material that has no epitaxial relation with the previously deposited material. The intermediate layer can inhibit further crystallite growth and reset the starting point for the subsequently deposited layer. A 0.5 nm thick intermediate layer of amorphous Al_2O_3 was demonstrated to be enough to disrupt the growth of crystallites between either two zirconium or hafnium oxide layers deposited by ALD [165].

Nanolaminates have already been demonstrated for tuning of the mechanical, linear and third-order nonlinear optical properties of ALD-grown films [164, 166, 167]. Therefore, we will apply the idea of nanolaminates to rationally design and optimize a metamaterial with the desired second-order nonlinear properties. Having identified the key factors determining the second-order response and ALD-compatible ways to control them, suggests a nanolaminate design that is built from alternating ZnO and Al_2O_3 layers. These ALD-grown layers are made up from a given number of deposition cycles of the respective material (see Section 3.1). The first layer consists of S cycles of Al_2O_3. It serves as a seed layer to enable subsequent ZnO crystallite growth with a controlled orientation. Additionally, it is supposed to limit the influence the substrate has on the ZnO growth. The nonlinear properties stem from the crystallites in the ZnO layers with Z cycles each. To control the crystallite size and, at the same time, favor crystallites with a defined orientation throughout the whole film, each ZnO layer is followed by I cycles of Al_2O_3 forming an intermediate layer. The sequence of $Z \times$ ZnO and $I \times Al_2O_3$ is one macrocycle, M, that can be repeated to achieve the desired film thickness (see Figure 4.1). In terms of ALD cycles the resulting nanolaminate sequence is

$$S \times Al_2O_3 + M \times (Z \times ZnO + I \times Al_2O_3)\,.$$

All plain film nanolaminate samples are deposited using the ALD process parameters discussed in Section 3.1. The films are deposited on either 170 µm thick borosilicate glass or silicon wafers used as substrates. Prior to deposition, the substrates are cleaned with acetone and, subsequently, dry-

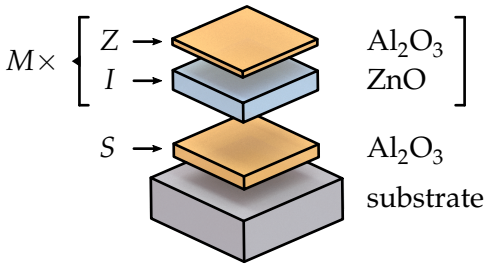

Figure 4.1: Schematic illustration of the nonlinear nanolaminate cycle sequence. S cycles of Al_2O_3 serve as the seed layer. On top of that macrocycles given by a sequence of $Z \times$ ZnO and $I \times Al_2O_3$ are repeated M times to arrive at the desired thickness.

blown with nitrogen. The film growth on the back surface of the substrates is avoided by using high temperature resistant masking tape that is removed after deposition.

4.1.2 Structural and Nonlinear Optical Characterization

With the nanolaminate design and fabrication outlined above, we want to verify the underlying assumptions for the used materials and process parameters both in terms of the structural and also nonlinear optical properties. Scanning electron microscopy, scanning transmission electron microscopy (STEM), and XRD are employed for the structural analysis. The generated second-harmonic power, $P_{2\omega}$, for a fundamental beam that is incident at an angle of 45° is divided by the squared film thickness, d^2, and used as a figure of merit for the optical second-order nonlinear response.

SEM is used for visual inspection of the deposited films. We study the growth of crystallites in pure ZnO films with 70, 175, and 350 ZnO cycles deposited on silicon wafers. As expected an increase of the crystallite size with the total film thickness can be qualitatively observed, if the growth is not limited, *e. g.*, by intermediate layers (see Figure 4.2a-c). The structural effect of the intermediate Al_2O_3 layers can be studied directly by inspecting the cross section of nanolaminates with $M = 7$ macrocycles, $Z = 50$ ZnO cycles, and $I = 10$, 50, and 100 intermediate layer cycles (see Figure 4.2d-f). Especially for $I = 50$ and $I = 100$ a clear laminate structure is visible suggesting a disruption of crystallite growth. Using SEM this observation is hard

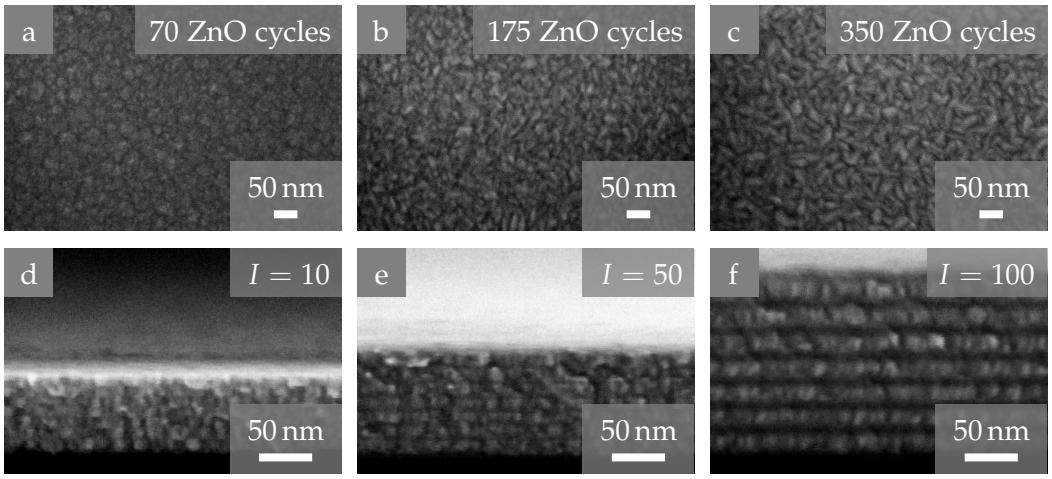

Figure 4.2: SEM image of ALD grown thin films. a-c) ZnO films with $Z = 70$, 175, and 350 cycles, respectively, viewed from above. An increase in ZnO crystallite size is visible for increasing Z. d-f) Cross section of nanolaminates with $M = 7$ macrocycles, $Z = 50$ ZnO cycles, and $I = 10$, 50, and 100 intermediate Al_2O_3 cycles, respectively. The substrate appears black and the top of the film is visible in the upper part of the images due to slightly tilted sample. A clear separation of individual layers is visible for $I = 50$ and $I = 100$ indicating a disruption of ZnO crystallite growth in these samples.

to validate for the sample with $I = 10$ intermediate cycles corresponding to an Al_2O_3 layer thickness of approximately 1.2 nm. STEM allows imaging the individual, well-separated layers even for this sample (see Figure 4.3a). Additionally, information on the elemental composition of the film can be obtained from energy-dispersive X-ray (EDX) maps depicted in Figure 4.3b-d. The Zn and Al maps reveal a modulation that is in agreement with the layers visible in Figure 4.3a. As expected, the O map shows a constant contribution in the whole nanolaminate.

The investigation using SEM and STEM seems to confirm some of the initial assumptions, but is difficult to interpret and analyze quantitatively. Therefore, $\theta/2\theta$ XRD measurements (see Section 3.5) are performed on samples with three different nanolaminate sequences to study the effects the seed and

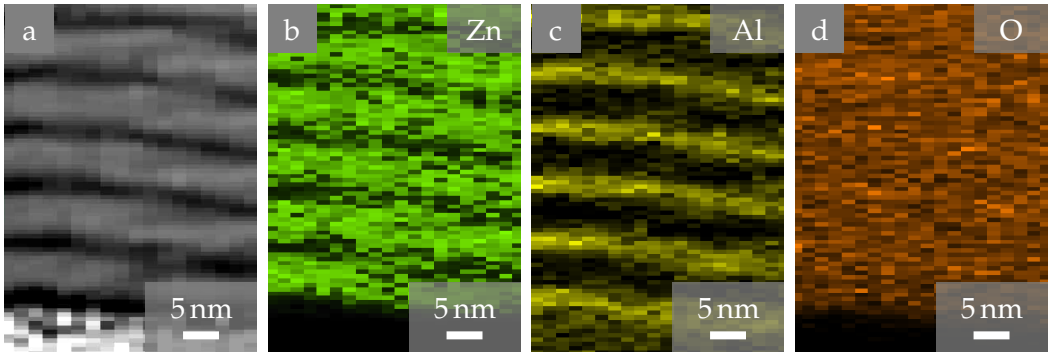

Figure 4.3: a) Cross section of a nanolaminate with $M = 7$ macrocycles, $Z = 50$ ZnO layer cycles, and $I = 10$ intermediate Al_2O_3 layer cycles taken using STEM. The separation of individual layers is visible despite an estimated intermediate layer thickness of only 1.2 nm. b-c) Elemental maps obtained from STEM-EDX measurements showing the integrated signal at the Zn−K, the Al−K, and the O−K edge, respectively. Both Zn and Al show the expected modulations, whereas, the O signal is homogeneous in the whole nanolaminate. Adapted from Reference [148].

intermediate Al_2O_3 layers have on the ZnO crystallites. The nanolaminates are fabricated on both glass and silicon wafer substrates. The latter facilitate the determination of the film thickness by means of ellipsometry. Sample A is a pure ZnO film with a total of 700 cycles deposited on a substrate and serves as a reference. A total thickness of $d = 95.1$ nm is determined using ellipsometry. The resulting mean growth per cycle of ZnO is merely 0.14 nm/cycle as compared to the value of 0.19 nm/cycle determined for the bulk growth per cycle (see Section 3.1). The reason is a nucleation delay that leads to a reduced growth per cycle of ZnO on the untreated substrate [117]. It is attributed to the strong sensitivity of ZnO growth to the substrate properties mentioned previously.

In Sample B an Al_2O_3 seed layer with $S = 50$ cycles is introduced beneath the ZnO film. This is supposed to reduce the substrate sensitivity and foster the growth of crystallites with a predefined orientation. A first hint suggesting that this approach works is the total film thickness of $d = 73.3$ nm resulting from the deposition of only 350 ZnO cycles on top of the seed layer. This value is in excellent agreement with the thickness estimated from

Sample	Cycle sequence	Measured thickness
A	$700 \times \mathrm{ZnO}$	95.1 nm
B	$50 \times \mathrm{Al_2O_3} + 350 \times \mathrm{ZnO}$	73.3 nm
C	$50 \times \mathrm{Al_2O_3} + 7 \times (50 \times \mathrm{ZnO} + 10 \times \mathrm{Al_2O_3})$	79.7 nm

Table 4.1: Samples used to study the influence seed and intermediate Al_2O_3 layers have on the ZnO crystallite growth. The mean growth per cycle in sample A is way lower as compared to sample B and C due to a nucleation delay of ZnO on the untreated substrate.

the bulk growth per cycle of the constituent materials. In contrast to ZnO, Al_2O_3 forms stable amorphous films and adheres perfectly well to all kind of substrates [103]. ZnO in turn shows no nucleation delay when grown on Al_2O_3.

Sample C is designed to investigate the effect of intermediate Al_2O_3 layers on the film properties. Starting from the sequence of sample B, the ZnO film is subdivided by introducing additional Al_2O_3 layers. We repeat the macrocycle of $Z = 50$ ZnO cycles followed by $I = 10$ Al_2O_3 cycles $M = 7$ times. The value of M is chosen such that the total thickness of the nonlinear material, *i. e.*, ZnO, remains the same as in sample B. Sample C has a total thickness of $d = 79.7\,\mathrm{nm}$ that is again in good agreement with the value estimated from the bulk growth per cycle. The cycle sequences and thicknesses of the three samples are summarized in Table 4.1.

The XRD $\theta/2\theta$ measurements of the three samples are depicted in Figure 4.4a. A quadratic baseline was subtracted from each data set. As discussed in Section 3.5 only lattice planes parallel to the film surface give rise to a signal in the given measurement configuration. In our samples we can identify three Bragg peaks. Using ZnO-powder diffraction measurements from literature (gray bars) as a reference, we can ascribe these peaks to contributions from (100), (002), and (101) ZnO crystallite planes oriented parallel to the substrate surface. The (100) and (101) orientations indicate the presence

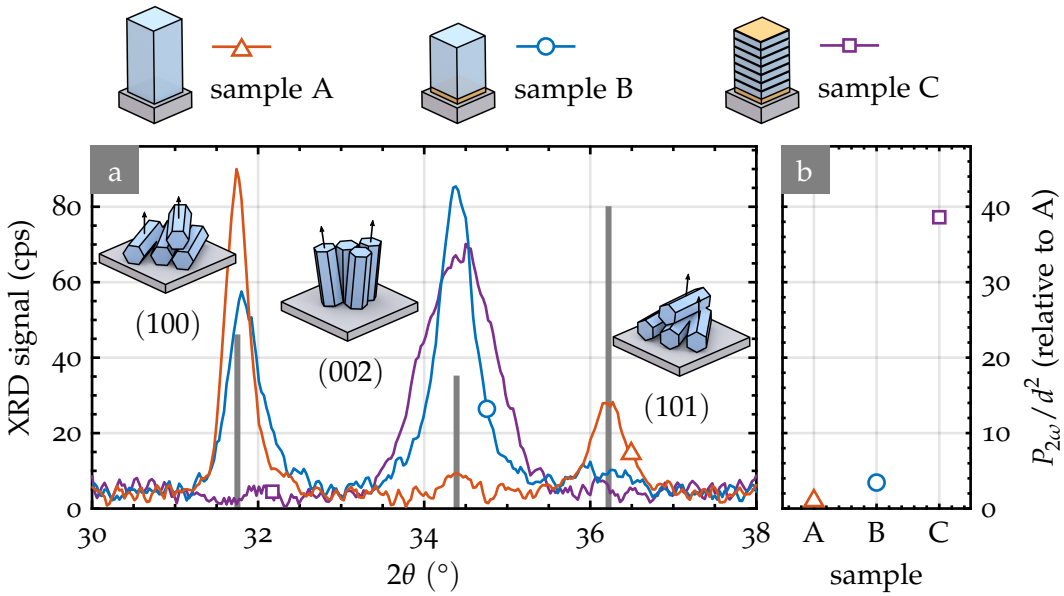

Figure 4.4: Structural and nonlinear optical characterization to investigate the effects of seed and intermediate Al_2O_3 layers on the ZnO crystallite growth based on the samples A, B, and C (see Table 4.1). a) XRD data derived from $\theta/2\theta$ measurements reveals the structural effects. The observed Bragg peaks stem from crystallites with (100), (002), and (101) orientation illustrated by the respective insets. Relative intensities from ZnO-powder diffraction measurements (gray bars) are depicted for comparison [168]. The Al_2O_3 seed layer greatly fosters the growth of ZnO crystallites with (002) orientation, *i. e.*, with their optical axis perpendicular to the substrate, in samples B and C. The additional intermediate Al_2O_3 layers in sample C limit the crystallite size perpendicular to the substrate plane and suppress the growth of crystallites with orientations other than (002). b) The generated second-harmonic power, $P_{2\omega}$, divided by the measured film thickness, d, squared is given relative to sample A and used as a figure of merit for the nonlinear optical performance. $P_{2\omega}/d^2$ increases by nearly 40 times going from the pure ZnO film (sample A) to the nanolaminate with seed and intermediate Al_2O_3 layers (sample C). Adapted from Reference [148].

of crystallites that have their optical axis (c-axis) in the plane of the film (see insets in Figure 4.4a). Due to the amorphous nature of the underlying surface as it is found in all samples, there is no preferential direction in the surface plane. Therefore, there is no reason for these crystallites to show a

preferential orientation leading to optical axes pointing into random directions. The situation is different for crystallites with (002) orientation. They have their optical axis perpendicular to the substrate surface and, therefore, show a well-defined orientation throughout the whole film.

According to the XRD data the pure ZnO film (sample A) consists mainly of crystallites with (100) and (101) orientation. The (002) planes should give a signal at a Bragg angle of 34.4°, but are barely visible in this sample. The picture changes dramatically once the Al_2O_3 seed layer is introduced in sample B: The XRD signal from crystallites with (002) orientation becomes the main contribution. At the same time, the signal from the two other orientations decreases. This validates the idea to control the orientation of ZnO crystallites by means of an amorphous Al_2O_3 seed layer. Introducing additional Al_2O_3 intermediate layers in sample C, has two further effects: First, the growth of crystallites with (100) and (101) orientation is strongly suppressed and peaks at the respective Bragg angles cannot be identified anymore. The orientation of ZnO crystallites with their optical axis perpendicular to the substrate is enforced throughout the whole film. Second, the remaining Bragg peak associated with (002) crystallite planes is broadened in samples C as compared to sample B. Using the Scherrer equation (see Equation 3.21) one can estimate the lower limit for the crystallite size, τ, which we identify with the size of the domain coherently contributing to the scattered signal, from the width of the (002) peak. The FWHM of the Bragg peaks is determined by fitting a Gaussian to the data after the subtraction of a quadratic baseline. A change in the crystallite size from $\tau = 15.1\,\text{nm}$ in sample B to $\tau = 8.4\,\text{nm}$ in sample C is observed. This change is in good agreement with the estimated thickness of 9.3 nm for the individual ZnO layers in sample C. This finding confirms that the growth of ZnO crystallites is indeed disrupted and that their size can be controlled by introducing intermediate Al_2O_3 layers.

The XRD measurements show structural changes that are in agreement with our expectations. The next step is to determine the effects these structural changes have on the nonlinear optical performance of the thin films. To this end we measure the generated second-harmonic power, $P_{2\omega}$, from sam-

ples A, B, and C using the setup depicted in Figure 3.5 (see Section 3.4). The p-polarized fundamental is incident at an angle of $\vartheta = 45°$ with respect to the surface normal and a mean power of 100 mW. The generated second-harmonic power increases with the square of the sample thickness for propagation lengths that are well below the coherence length (see Equation 2.27). Therefore, we use the second-harmonic power divided by the film thickness, d, squared as a figure of merit to take different sample thicknesses into account (see Figure 4.4b). The seed layer fosters the growth of well-oriented crystallites and results in an increase of $P_{2\omega}/d^2$ by more than three times from sample A to sample B. The improvement is even more pronounced in sample C that shows a signal that is nearly 40 times larger than that of sample A. On a structural level we ascribe this enhancement to an optimized crystallite size maximizing the contribution from grain boundaries and interfaces. Additionally, the intermediate Al_2O_3 layers can be regarded as seed layers in the depth of the nanolaminate that promote crystallites with a well-defined orientation, reduce stacking faults, and lead to homogeneous effective properties.

The generated second-harmonic signal from ZnO/Al_2O_3 nanolaminates is further analyzed to exclude possible sources of error. First of all a quadratic relation between the fundamental and the second-harmonic power is expected for thin films (see Equation 2.27). Exemplary measurements on four samples with different values of the number of macrocycles, M, are depicted in Figure 4.5a and confirm the quadratic dependence. Using a PMT for detection one lacks the spectral sensitivity to make sure the detected signal is at the proper wavelength and not contaminated. Therefore, we perform exemplary measurements of the second-harmonic signal using a spectrometer. For the fundamental tuned to a center wavelength of 800 nm, the generated second-harmonic signal is indeed centered around a wavelength of 400 nm (see Figure 4.5b). Other contributions to the signal do not exist. Finally, we expect a purely p-polarized second-harmonic given a fundamental beam with identical polarization and considering the symmetry of the second-order susceptibility tensor (see Equations 3.18). Figure 4.5c shows a polarization resolved measurement of the generated signal that is in excellent agreement

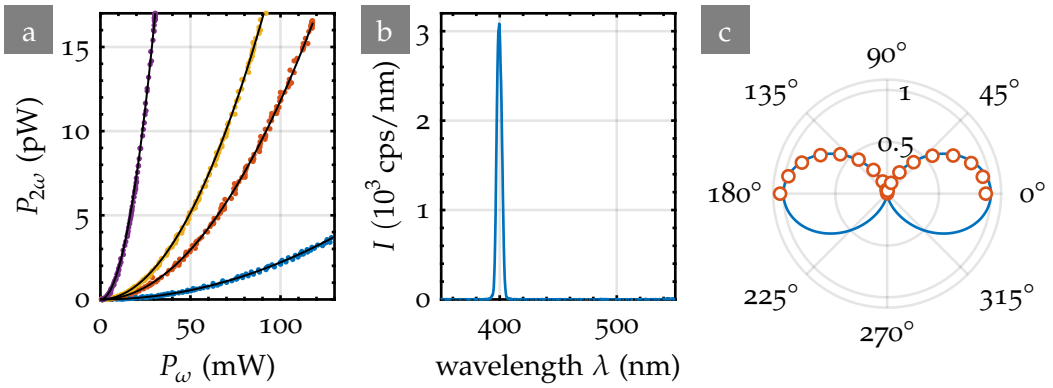

Figure 4.5: Optical characterization of the second-harmonic generated in ZnO/Al_2O_3 nanolaminates. a) The quadratic dependence of the second-harmonic power, $P_{2\omega}$ on the fundamental power, P_ω, is confirmed for nanolaminates with different values of the number of macrocycles, M. The black curves are quadratic fits to the data. b) Spectral analysis of the generated second-harmonic signal showing the expected position at 400 nm for a fundamental signal centered around 800 nm. c) The polarization dependence of the normalized second-harmonic power (red dots) is in agreement with the anticipated behavior of a p-polarized beam (blue curve).

with the predictions.

4.1.3 Systematic Nanolaminate Sequence Sweeps

Having demonstrated the validity of the initial assumptions that lay the foundation for the nanolaminate metamaterial design, systematic parameter sweeps are performed to get a better understanding and identify the optimal cycle sequence. One has to keep in mind that the individual optimized layer thicknesses discussed in the following are specific to the used ALD system and process parameters. Nevertheless, the underlying mechanism and the rational design can be widely applied to tailor the desired nonlinear response for other systems and fabrication parameters as well. The characterization is again based on the measurement of the second-harmonic power generated for excitation conditions that are identical to the ones discussed before. The quantity $P_{2\omega}/d^2$ is used as a figure of merit and the film thickness, d, is estimated from the growth per cycle of ZnO and Al_2O_3 as it is given in

Section 3.1. Our starting point is the cycle sequence of sample C. Variations of the number of seed layer cycles, S, the intermediate layer cycles, I, and the cycles in the individual ZnO layers, Z, are performed.

The influence of the seed layer is studied by varying the number of seed layer cycles, S, in six nonlinear nanolaminate samples following the sequence $S \times Al_2O_3 + 7 \times (50 \times ZnO + 10 \times Al_2O_3)$. The generated second-harmonic power, $P_{2\omega}$, increases with S and saturates around $S = 100$ for an estimated Al_2O_3 seed layer thickness of 12 nm (see Figure 4.6a). We ascribe this behavior to the reinforced growth of crystallites with their optical axis oriented perpendicular to the substrate. Additionally, the influence the substrate has on the ZnO growth decreases with increasing seed layer thickness and saturates once this influence is completely screened. We aim at the design of a nonlinear material with maximized effective nonlinear properties and, hence, the sample with $S = 50$, showing the largest value of $P_{2\omega}/d^2$, is optimal for our purpose.

The number of intermediate layer cycles, I, is varied for samples with the sequence $50 \times Al_2O_3 + 7 \times (50 \times ZnO + I \times Al_2O_3)$. A rapid increase of the second-harmonic power, $P_{2\omega}$, is observed when going from $I = 0$ to 7 cycles (≈ 0.8 nm) and keeps on increasing more slowly up to $I = 100$ (see Figure 4.6b). The rapid increase for thin layers suggests that a minimum number of intermediate layer cycles, I, is necessary to stop the crystallite growth and enforce a preferential growth orientation in the subsequently deposited ZnO layer. This finding is in good agreement with the previously found minimal Al_2O_3 layer thickness of 0.5 nm that was shown to be necessary to disrupt the growth between adjacent zirconium or hafnium oxide layers [165]. Despite the fact that $P_{2\omega}$ keeps increasing with increasing I, we find a maximum of our figure of merit, $P_{2\omega}/d^2$, for $I = 10$ and, hence, will use this optimized value in the following.

Finally, the number of ZnO cycles, Z, in each layer is varied while adjusting the number of macrocycles, M, such that the total number of ZnO cycles is fixed to 350. This allows for a comparison of sequences that have the same

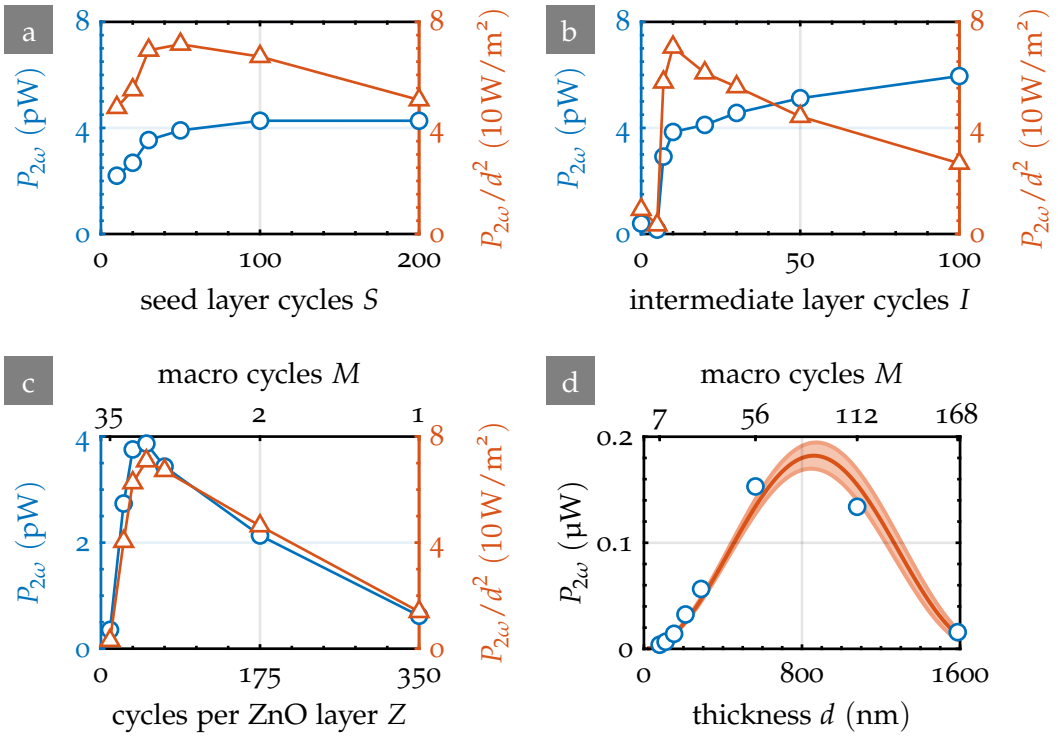

Figure 4.6: a-c) Parameter sweeps used to optimize the nonlinear nanolaminate cycle sequence and get a deeper understanding of the individual influencing factors. For each sample the generated second-harmonic power, $P_{2\omega}$, for a p-polarized fundamental beam that is incident at an angle of 45° and with a mean power of 100 mW is measured. The quantity $P_{2\omega}/d^2$ with the estimated film thickness, d, is used as the figure of merit for optimization. Based on the sequence of sample C, a) the number of Al_2O_3 seed layer cycles, S, b) the number of cycles in each intermediate Al_2O_3 layer, I, and c) the number of cycles per ZnO layer, Z, for a fixed total number of 350 ZnO cycles are varied. c) Generated second-harmonic power, $P_{2\omega}$, from samples following the optimized sequence $50 \times Al_2O_3 + M \times (50 \times ZnO + 10 \times Al_2O_3)$. The number of macrocycles is varied from $M = 7$ to 168. The measured data (blue dots) is in excellent agreement with theoretical calculations (red curve) based on the assumption of effective material properties. The error region (red area) stems from slight variations of refractive indices measured for the individual samples. Adapted from Reference [148].

total nonlinear material thickness. The fabricated nanolaminates follow the cycle sequence $50 \times Al_2O_3 + 350/Z \times (Z \times ZnO + 10 \times Al_2O_3)$. Figure 4.6c

shows that the generated second-harmonic power, $P_{2\omega}$, is small for samples with a large number of macrocycles and thin ZnO layers, *e. g.* $M = 35$ and $Z = 10$. Interestingly the same is also true for just one macrocycle ($M = 1$) and a ZnO layer with $Z = 350$ cycles. The reason is that, on the one hand, the crystallites have to be sufficiently distinct to show an optical nonlinearity at all. By stopping the ZnO crystallite growth through the introduction of an intermediate Al_2O_3 layer after just a few cycles, prevents them from growing to the necessary size. On the other hand, the probability for stacking faults increases with the thickness of the individual ZnO layers given by Z [161]. This leads to the growth of crystallites with undesired orientations and the incorporation of defects. Additionally, the increased crystallite size is accompanied by a decreased contribution of grain boundaries and interfaces to the effective second-harmonic susceptibility [163]. In between these two extrema, there is a sweet spot for the thickness of the individual ZnO layers. The contributions to the second-order nonlinearity from ZnO crystallites and from interfaces and grain boundaries have to be balanced while, at the same time, ensuring a proper crystallite alignment. For the given configuration the second-order nonlinear response in terms of both $P_{2\omega}$ and $P_{2\omega}/d^2$ is maximized for $Z = 50$ cycles per ZnO layer. Therefore, we conclude that the nanolaminate sequence optimized for a strong second-harmonic generation under the given conditions is $50 \times Al_2O_3 + 7 \times (50 \times ZnO + 10 \times Al_2O_3)$ and, hence, identical to the sequence used for sample C.

4.1.4 Effective Material Hypothesis

The nonlinear optical properties in thin films usually change with their thickness as a consequence of the mechanisms discussed above. In contrast, a proper metamaterial is expected to show effective material properties approaching a constant value for an increasing number of unit cells. We expect to find a similar behavior in our nanolaminates that is enabled through the nanolaminate design and the role the individual layers with a thickness well below the interacting wavelengths play.

To investigate this effective material hypothesis, we fabricate samples following the sequence $50 \times Al_2O_3 + M \times (50 \times ZnO + 10 \times Al_2O_3)$ with the

number of macrocycles going from $M = 7$ to 168. The second-harmonic power, $P_{2\omega}$ generated in a nonlinear material is proportional to the squared thickness for propagation lengths that are well below the coherence length L_c. For second-harmonic generation with a non-zero phase mismatch a deviation from this behavior occurs when the thickness, d, approaches the coherence length, L_c. The direction of energy flow that is initially going from the fundamental to the second-harmonic wavelength is reversed and oscillations of $P_{2\omega}$ as a function of d occur. Figure 4.6d shows the second-harmonic power, $P_{2\omega}$, generated from samples with different thicknesses, d, for the excitation conditions also used in the previous parameter sweeps. We compare the experimental data with expectations for $P_{2\omega}$ based on the theoretical model presented in Reference [139]. Due to slight fluctuations in sample fabrication and the deviations from the effective material limit for small values of M, there is a variation in the effective dispersion relation determined from ellipsometry measurements on the individual samples. A theoretical curve for the generated second-harmonic power, $P_{2\omega}$, is, therefore, calculated for each of the eight samples with their respective effective material parameters. The average of these eight curves is scaled with one global parameter to best fit the measured data (red curve). The error region (red area) is estimated from the deviations of the individual curves. The excellent agreement between the experimental data and the theoretical model based on effective material properties confirms the effective material hypothesis and indicates that we are in the bulk metamaterial limit (see Section 2.7). Therefore, our nonlinear nanolaminate design overcomes the shortcomings of conventional nonlinear thin films as it ensures constant effective nonlinear optical material properties that are almost insensitive to the used substrate and the total thickness of the deposited film.

4.1.5 Determining the Second-Order Susceptibility Tensor

Having found the optimized nanolaminate metamaterial sequence, we want to determine the full second-order susceptibility tensor, $\chi^{(2)}$. The measurements at a mean fundamental power of 200 mW are performed on a sample with $M = 28$ macrocycles and the overall sequence $50 \times Al_2O_3 + 28 \times (50 \times ZnO + 10 \times Al_2O_3)$. Figure 4.7 depicts a typical measurement

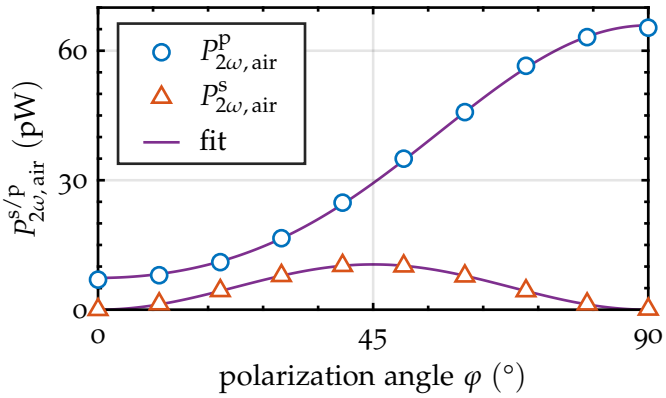

Figure 4.7: Typical measurement used to determine the elements of the second-order susceptibility tensor on a sample with $M = 28$. The generated s-/p-polarized second-harmonic power, $P^{s/p}_{2\omega,\mathrm{air}}$, is measured for varying polarization angles, φ, of the fundamental beam. The mean fundamental power is set to 200 mW incident at a fixed angle of $\vartheta = 45°$. The three independent second-order susceptibility tensor elements are determined by fitting a theoretical model (see Section 3.4) to the data resulting in $\chi^{(2)}_{xxz} = 1.6\,\frac{\mathrm{pm}}{\mathrm{V}}$, $\chi^{(2)}_{zxx} = 1.5\,\frac{\mathrm{pm}}{\mathrm{V}}$, and $\chi^{(2)}_{zzz} = -4.0\,\frac{\mathrm{pm}}{\mathrm{V}}$. Adapted from Reference [148].

used for the nonlinear characterization following the method described in Section 3.4. To ensure reproducibility, the measurement is repeated 23 times at different spots on two nominally identical samples. The values for the three independent second-order susceptibility tensor elements (see Equation 3.17) derived for each measurement show a relative standard deviation of no more than 10 % and their mean values are

$$\begin{aligned} \chi^{(2)}_{xxz} &= 1.6\,\tfrac{\mathrm{pm}}{\mathrm{V}}, \\ \chi^{(2)}_{zxx} &= 1.5\,\tfrac{\mathrm{pm}}{\mathrm{V}}, \\ \chi^{(2)}_{zzz} &= -4.0\,\tfrac{\mathrm{pm}}{\mathrm{V}}. \end{aligned} \tag{4.1}$$

The fact that the tensor elements $\chi^{(2)}_{xxz}$ and $\chi^{(2)}_{zxx}$ are not identical shows that Kleinman symmetry is not valid and, therefore, dispersion effects are not negligible for a fundamental wavelength of 800 nm (see Section 3.4).

4.1.6 Discussion

The presented results successfully demonstrate the rational design and tunability of a second-order nonlinear optical nanolaminate metamaterial. The magnitude of the derived second-order susceptibility tensor elements is comparable to well-established bulk crystals [141]. At the same time, our approach provides all the benefits accompanied by conformal thin film deposition using ALD and clearly exceeds the values previously obtained for ALD-grown ABC-type nanolaminates [95, 101]. Nevertheless, there is still room for improvement and fine tuning.

Our approach was adopted by the group of Roel Baets resulting in the fabrication of ALD-grown ZnO/Al_2O_3 films showing even larger values of the second-order susceptibility tensor elements. For ZnO grown on an Al_2O_3 seed layer a value of $\chi^{(2)}_{zzz} = (-15 \pm 4)\,\mathrm{pm/V}$ was derived [169]. The Al_2O_3 seed layer is grown under similar conditions, from the same precursors, and with the same thickness as in our structures. Therefore, we ascribe the difference in the nonlinear response to the quality of the deposited ZnO layer. The large values for the second-order susceptibility were measured for a ZnO film deposited by means of plasma-enhanced ALD using DEZ and an oxygen plasma at a temperature of 300 °C. These films seem to show a superior nonlinear response that is in agreement with the higher structural quality observed in films grown by plasma-enhanced ALD [105]. Despite the differences in the used ALD system, it was found that the introduction of an Al_2O_3 seed layer strongly enhances the second-harmonic response, thereby, once again confirming our basic idea and the general applicability of this approach. Unfortunately, systematic parameter sweeps to identify an optimal cycle sequences for this system were not performed.

Another opportunity for improvement lies in the unwanted n-type doping in ALD deposited ZnO films that leads to absorption in the infrared wavelength regime [170]. This could especially hinder the use in waveguide applications where long propagation distances are quite common. The process parameters can be optimized to decrease the carrier concentration by replacing the H_2O precursor with ozone (O_3) [171]. Another way is once again the use of

plasma-enhanced ALD that was shown to result in more stoichiometric ZnO films and a reduced intrinsic carrier concentration as compared to thermal ALD [105].

4.2 3D Nanolaminated Photonic Crystals

The second part of the results chapter covers the fabrication and characterization of 3D photonic crystals that are conformally covered with a second-order nonlinear nanolaminate. We will focus on the process of second-harmonic generation in these structures that we call 3D nanolaminated photonic crystals or, equivalently, 3D metacrystals. The fabrication, characterization and the finite element calculations were performed by the author. A. Abass provided guidance with the latter. SEM and focused-ion-beam (FIB) milling was done by the author and P. Brenner, respectively. The results were interpreted by the author together with A. Abass, H.-H. Hsiao, C. Rockstuhl, and M. Wegener.

3D nanolaminated photonic crystals are based on 3D photonic crystals that are combined with a conformally deposited nanolaminate metamaterial used to change the properties and extend the functionality of the resulting structure. The 3D photonic crystals serve as polymer templates and are fabricated by means of 3D DLW. In combination with the conformal deposition of ALD-grown, nonlinear ZnO/Al_2O_3 nanolaminates, the polymer template dictates a complex spatial distribution of the second-order nonlinear susceptibility tensor. This distribution can be adjusted by changing the geometrical parameters of the template and, thereby, tune the interplay of nonlinear nanolaminate and photonic crystal with the goal to achieve enhanced second-order nonlinear interactions in 3D nanolaminated photonic crystals.

4.2.1 Sample Design and Fabrication

The decision to use photonic crystals as polymer templates is motivated in their unique properties and beneficial effects on nonlinear interactions described in Section 2.5. Among 3D photonic crystals the so-called woodpile structure is quite common as it is compatible with layer-by-layer fabrication. Using 3D DLW we are not limited by such restrictions, nevertheless, the woodpile photonic crystal is also popular with this fabrication method and is quite versatile in its applications [80, 125, 172, 173]. We will base

our structures on 3D woodpile photonic crystals with different geometrical parameters to demonstrate the effects of the underlying template on the resulting nonlinear response.

A woodpile photonic crystal consists of periodically arranged rods with the horizontal rod spacing denoted by a. The individual rod layers are stacked on top of each other. One commonly used scheme has adjacent layers rotated by an angle of 90° with respect to each other. Additionally, two consecutive parallel rod layers are shifted horizontally by $a/2$. In stacking (axial) direction the structure repeats itself after four layers and the periodicity is given by the axial lattice constant, c. In general, the woodpile photonic crystal is described by a face-centered tetragonal lattice [36]. The special cases of a face-centered and a body-centered cubic lattice are given for an axial lattice constant to rod spacing ratio, c/a, of $\sqrt{2}$ and 1, respectively [174, 175].

In 3D DLW the rods of woodpile photonic crystals are, usually, written as individual lines. As a consequence of the elongation of the 3D DLW writing focus in the axial direction, the rods have an approximately elliptical cross section. The rod semiaxes are equal in the lateral direction: $r_x = r_y$. The axial semiaxis is determined by the aspect ratio as $r_z = r_x \cdot \mathrm{AR}$. AR ≈ 2.5 is derived using FIB milling and is in agreement with values typically found in 3D DLW [126]. The woodpile photonic crystals are fabricated on 170 µm thick borosilicate glass substrates using the DLW setup described in Section 3.2. The photoresist is based on PETA without an additional photoinitiator and is excited at a wavelength of 405 nm. The mean writing power, P, at the back-focal plane of the objective lens is varied around 1.2 mW. An increase (decrease) in writing power leads to larger (smaller) dimensions of the rod semiaxes and, therefore, allows for the fabrication of templates with different filling fractions, f. The rod spacing, a, takes values around $a = 675$ nm and is chosen such that the stop band of the resulting 3D nanolaminated photonic crystal lies in the regime that can be investigated by the setup used for nonlinear characterization. The axial lattice constant, c, is given in terms of the ratio c/a that we choose to be even smaller than the value for a body-centered cubic lattice. The reasons for this choice will be discussed and explained below. If not specified otherwise, the number of axial periods

is fixed to $N_z = 6$ and the footprint is $70\,\mu m \times 70\,\mu m$. After 3D DLW the polymer templates are developed in mr-Dev 600 (micro resist technology) for 15 minutes to remove the unpolymerized photoresist remains. To avoid damage during the evaporation of the remaining solvents, the structures are transfered to acetone and critical point dried (Leica, EM CPD030).

The next step is the conformal ALD growth of the previously discussed optimized nonlinear nanolaminate sequence. We deposit two nanolaminate macrocycles, M, resulting in a total ALD layer thickness, d_{ALD}, of approximately 27 nm. An alternative to the deposition of nonlinear ZnO/Al_2O_3 nanolaminates are nonlinear ABC-type nanolaminates (see Section 2.7). In deed, some experiments were conducted for this configuration as well. Nevertheless, the way lower second-order susceptibility of ABC-type nanolaminates leads to a low signal-to-noise ratio and complicates measurements. Therefore, we will focus on a consistent dataset based solely on structures with ZnO/Al_2O_3 nanolaminates in the following. To protect the polymer template and, at the same time, allow for a conformal growth on the complex 3D structure, we follow the ALD recipe for 3D polymer templates discussed in Section 3.1 at a deposition temperature of 150 °C . The nanolaminate growth is limited to the substrate side holding the polymer template by masking the backside with high temperature resistant tape that is removed after deposition. A 3D nanolaminated photonic crystal is schematically illustrated in Figure 4.8.

4.2.2 Structural and Linear Optical Characterization

The fabricated 3D nanolaminated photonic crystals are investigated using SEM and FIB milling to make sure the quality aligns with the expectations and to extract geometrical parameters for the use in FEM calculations. To avoid charging effects during image taking the samples are sputter coated with a 10 nm thick gold layer. The polymer template parameters are identical with the ones used in the optical experiments. Figure 4.9a depicts the SEM image of a structure with a rod spacing of $a = 675\,nm$ and a footprint of $70\,\mu m \times 70\,\mu m$. It suggests a highly homogeneous structure quality without

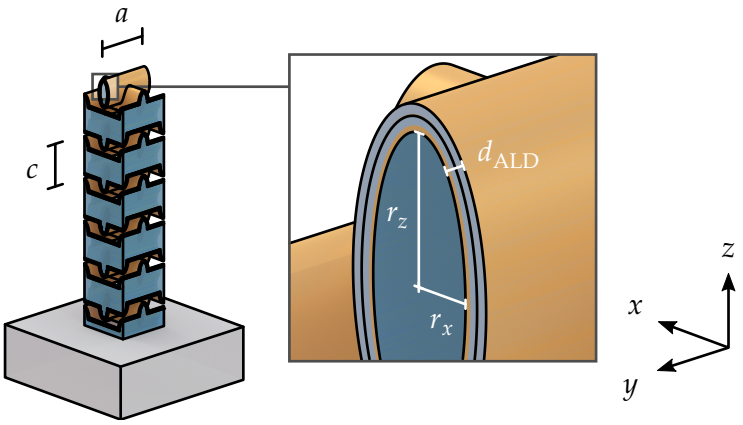

Figure 4.8: Scheme of a 3D nanolaminated woodpile photonic crystal with rod spacing a and axial lattice constant c. The structure has $N_z = 6$ unit cells in the axial direction and is periodically continued in x- and y-direction. The woodpile photonic crystal consists of elliptical rods that are characterized by the semiaxes r_x, r_y, and r_z with $r_x = r_y$. A conformal nanolaminate metamaterial layer with thickness d_{ALD} surrounds the polymer template. Adapted from Reference [176].

the shrinkage effects that are often found in DLW structures. The reason lies in the modified 3D DLW setup used for fabrication. The given woodpile parameters would be challenging for a standard DLW setup with an excitation wavelength of 810 nm. As discussed earlier we use an excitation wavelength of 405 nm and, thereby, are able to reduce the focus size by a factor of two. The increased resolution allows for fabrication with an exposure dose, D, that is clearly above the threshold dose, D_{th}. This leads to a higher degree of cross-linking in the polymer and reduced shrinkage effects as compared to woodpile photonic crystals written near the threshold dose, D_{th}.

For FIB milling a total of $M = 20$ nanolaminate macrocycles are deposited onto the DLW-written woodpile photonic crystal. The result is a solid structure that consists of the polymer template and the ALD-grown film. This way we can ensure the stability necessary for FIB milling is given. Figure 4.9b shows the bulk of a structure with $N_z = 6$ axial periods (24 layers). The polymer appears black and shows rods that are well separated both in the lateral and the axial direction. The DLW writing power used for this structure lies

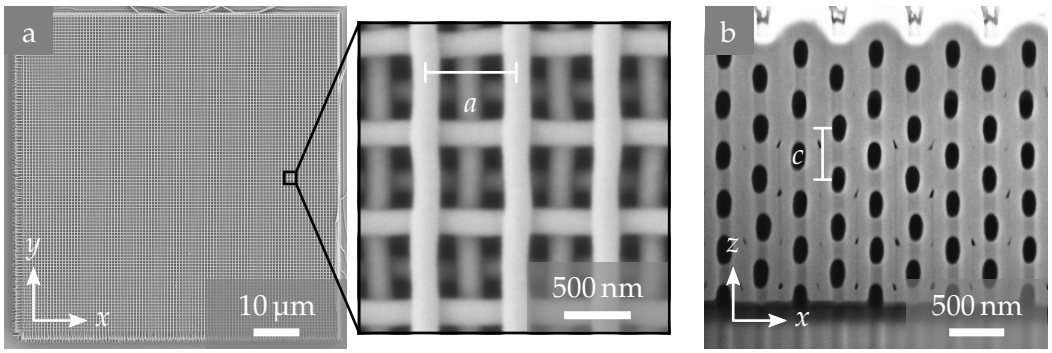

Figure 4.9: a) Scanning electron micrograph showing a fabricated 3D nanolaminated woodpile photonic crystal with $M = 2$ deposited nanolaminate macrocycles. The depicted sample has a rod spacing, a, of 675 nm and a footprint of 70 µm × 70 µm. b) To ensure the stability necessary for FIB milling, the photonic crystal template is completely filled using ALD. In the scanning electron micrograph the polymer and the ALD layer look black and gray, respectively. An axial lattice constant of $c = 540$ nm is derived. Adapted from Reference [176].

in the center of the power range used to fabricate the 3D nanolaminated photonic crystals discussed in the following. The derived mean values of the geometrical parameters for this configuration are: $r_x = 62$ nm, AR = 2.5, $a = 675$ nm, $c = 540$ nm, and $c/a = 0.8$. In the axial direction we find a shrinkage of roughly 13 % when comparing the observed ratio of c/a to the intended value of $c/a = 0.92$. We will take this into account by adjusting the value of c/a for the fabricated structures in the following discussion using the determined factor. Obviously, this correction factor is not the same for all structures as the actual shrinkage will depend on the writing power and the geometrical parameters. Nevertheless, an estimation based on a constant factor is sufficient for our purposes as the value is only used for a qualitative comparison of experimental results and numerical calculations.

SEM and FIB are good ways to verify that the parameters are in the specified range. Nevertheless, these techniques are time consuming and, afterwards, the structures cannot be used for further experiments. Additionally, they give no direct measure of the optical performance. Therefore, we use linear

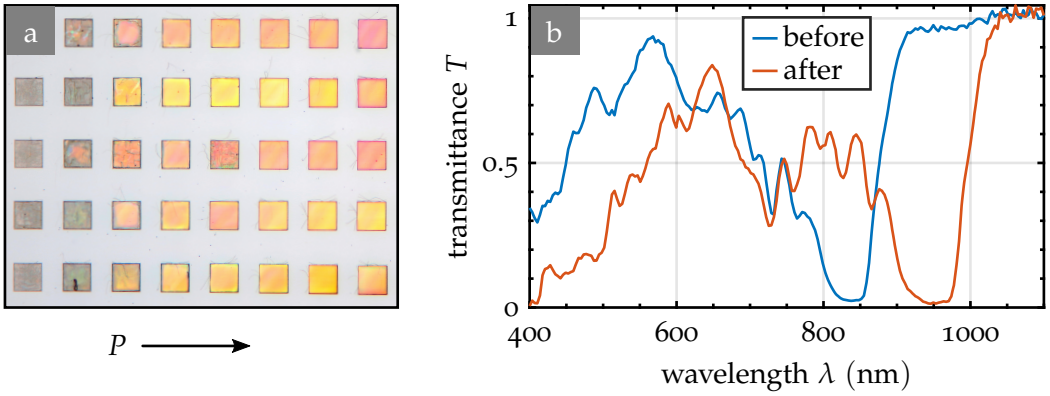

Figure 4.10: a) Optical microscope image of woodpile photonic crystals taken in reflection mode. The samples are fabricated at different writing powers, P, (horizontal) and rod spacings, a, (vertical). The colorful appearance indicates the existence of a stop band. Underexposed structures look grayish or inhomogeneous. b) Linear transmittance, T, of a woodpile photonic crystal before and after the conformal deposition of two macrocycles of the nonlinear nanolaminate. The ALD-grown film results in a spectral shift towards longer wavelengths, but shows barely any effects on the form of the spectrum otherwise. The good structural quality both before and after ALD is confirmed by the high transmittance below the stop band.

optical methods to further characterize the structures. Both the "raw"and conformally coated woodpile photonic crystals are expected to exhibit a stop band. In this wavelength region, that shifts with the fabrication parameters, the structures are supposed to show a high reflectivity. Therefore, a suitable set of writing parameters and eventually occurring fabrication problems can be easily identified at a glance using an optical microscope in reflection mode. Figure 4.10a shows such a micrograph of structures fabricated at different writing powers, P, (horizontal) and with different rod spacings, a, (vertical). The colorful appearance indicates the existence of a stop band. Structures written at too low powers are underexposed and unstable, Therefore, they show no or just inhomogeneous reflections. At writing powers that are chosen too high, the rods are no longer separated in the axial direction. Again the structures look grayish (not depicted).

This qualitative approach is supplemented by measurements of the linear

transmittance, T. We use the setup described in Section 3.3 to analyze the structures both before and after the ALD step. Exemplary measurements for one structure are depicted in Figure 4.10b. After ALD the stop band lies in the low transmittance region slightly below 1000 nm. The excellent structure quality both before and after ALD is confirmed by the high transmittance ($T \geq 80\,\%$) that is observed in the short-wavelength regime below the stop band. We find a spectral shift by approximately 120 nm towards longer wavelengths after the conformal deposition of two macrocycles of the nanolaminate metamaterial. Otherwise, the spectrum remains more or less unchanged. This behavior is in good agreement with our expectations: The 3D nanolaminated photonic crystal is very similar to the plain polymer template, but with increased mean refractive index and filling fraction.

4.2.3 Nonlinear Optical Characterization

The interplay of 3D woodpile photonic crystals and nonlinear nanolaminate metamaterials is expected to result in a spectrally dependent nonlinear response of the composite structure that is based on either phase matching or reinforced light-matter interactions provided by the photonic crystal template (see Section 2.5). The goal is to identify the involved mechanisms and, thereby, get a deeper understanding of 3D nanolaminated photonic crystals. To this end, we use the setup presented in Section 3.4 and measure the spectrally and diffraction order resolved second-harmonic power from our structures by imaging the back-focal plane of the objective lens onto the entrance slit of a spectrometer. The emitted signal is compared to the performance of the plain nonlinear film to compensate for dispersive properties of the setup and the second-order susceptibility tensor of the nanolaminate metamaterial that was shown to break Kleinman symmetry (see Section 4.1.5). Additionally, the strong variations of available excitation power at different fundamental wavelengths are accounted for by dividing the obtained data by the measured mean fundamental power, P, squared. The resulting quantity will, nevertheless, be referred to as an intensity and can be identified from the context and the given unit.

The second-harmonic response of the plain film necessary for the normal-

ization is measured for each sample right next to the 3D nanolaminated photonic crystals using p-polarized light incident at an angle of 45° with respect to the surface normal. Figure 4.11a shows the spectral intensity detected on the charge-coupled device array when the film is excited at a fundamental wavelength of $\lambda_F = 800\,\text{nm}$. As expected, there are no diffraction orders from the plain film and the only contribution to the signal stems from the generated second-harmonic centered around 400 nm. To allow for an easier interpretation, we omit the spatial information and sum over the vertical reciprocal space axis. The result is the spectral intensity, I, for an excitation at $\lambda_F = 800\,\text{nm}$ depicted in Figure 4.11b. This step is repeated for 111 different fundamental wavelengths in the range from 800 nm to 1020 nm and gives the overlay of spectra shown in Figure 4.11c. It confirms the necessity for normalization: Despite the fact that the variation in fundamental power, P, is already accounted for, the peak intensity, I, varies strongly for different excitation wavelengths. The measured data is further compressed by integrating the spectral intensity, I, in each second-harmonic peak. This gives the generated second-harmonic intensity, $I_{2\omega}$, as a function of the fundamental wavelength, λ_F, (see Figure 4.11d) that is used to normalize the results obtained from 3D nanolaminated photonic crystals and allows for comparing the nonlinear response at different wavelengths.

The general procedure used to analyze the second-harmonic generated from 3D nanolaminated photonic crystals is very similar to the one just described for the nonlinear thin films, but also involves additional measurements to study the effects arising from the interplay with the polymer template. We use a fundamental beam that is polarized along the x-axis and incident at an angle of 0° with respect to the surface normal. The mean fundamental power, P_ω, is set to 30 mW at $\lambda_F = 800\,\text{nm}$. As mentioned earlier, the rod spacing, a, in our structures is such that we expect to collect higher diffraction orders of the generated second-harmonic. The emission characteristics of the structures in reciprocal space are studied by rotating the spectrometer grating to its zeroth diffraction order. Figure 4.12a shows an example of the obtained back-focal plane image for an excitation wavelength of $\lambda_F = 964\,\text{nm}$. The visibility of low intensity features is increased by using a scale that is linear

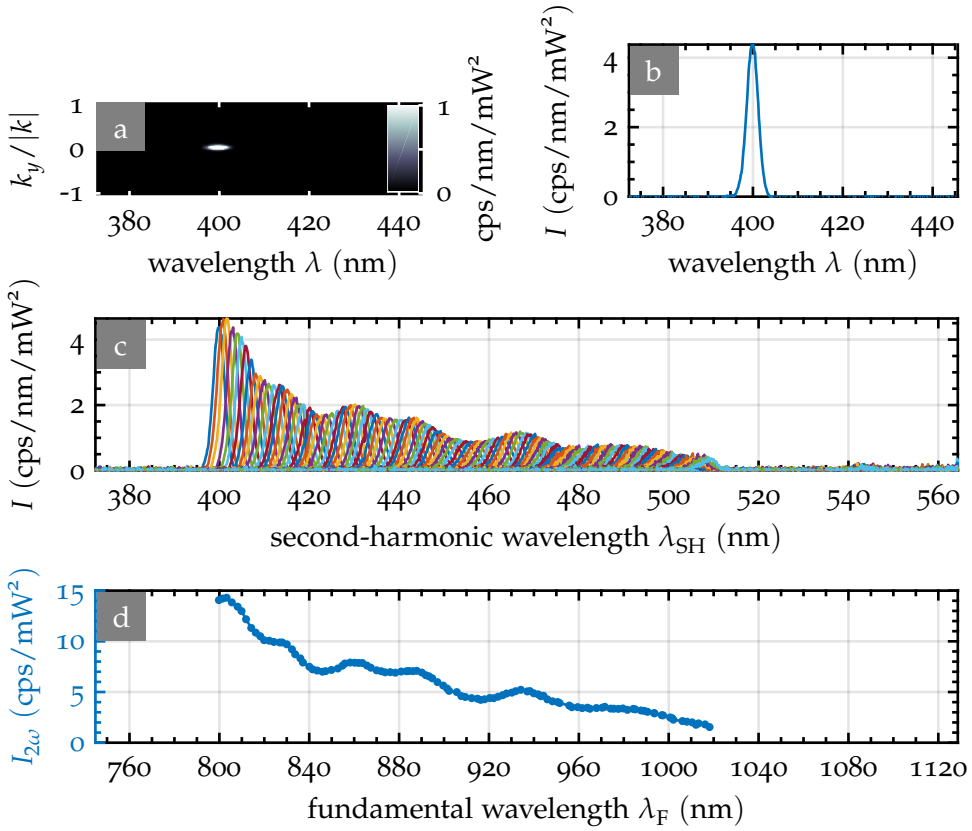

Figure 4.11: a) Hybrid image of the nonlinear nanolaminate emission with the wavelength, λ, on the horizontal and the reciprocal space on the vertical axis. The film is excited at an incidence angle of 45° and a fundamental wavelength, λ_F, of 800 nm. As expected, the generated second-harmonic is centered around 400 nm. b) Spectrum of the generated signal that is derived from panel a) by summing over the vertical reciprocal space axis and dividing by the squared mean fundamental power. c) Overlay of emission spectra derived in the same manner as b) but for 111 different fundamental wavelengths, λ_F. d) The wavelength-dependent second-harmonic intensity, $I_{2\omega}$, generated in the nanolaminate film is obtained from the peak area in each spectrum shown in panel c) and depicted as a function of the incident fundamental wavelength, λ_F.

up to an intensity of 15 cps/px/mW² and saturated for larger values. The limit of the circular field of view is clearly visible and determined by the NA of the objective lens used to collect the emitted light. Five distinct spots

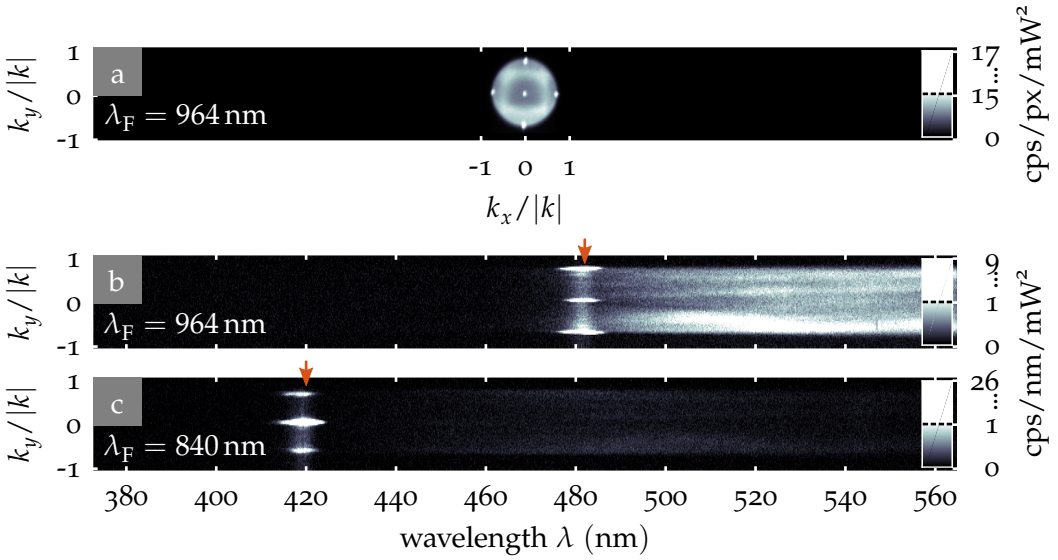

Figure 4.12: Measurements on 3D nanolaminated photonic crystals excited at the indicated fundamental wavelength, λ_F. a) For the spectrometer grating rotated to its zeroth order, an image of the generated signal in reciprocal space is obtained. The bright spots are ascribed to the zeroth and first diffraction orders of the generated second-harmonic. Additionally, a fluorescence background signal is visible. b-c) With the spectrometer grating rotated to its diffraction order, a hybrid image with the wavelength on the horizontal and the reciprocal space on the vertical axis is obtained. In this spectrometer operation mode the same structure as shown in panel a) is excited at two different fundamental wavelengths, λ_F. The red arrows indicate the respective second-harmonic wavelength, λ_{SH}. The diffraction orders of the generated second-harmonic signal are clearly visible and their relative strength varies with λ_F. The fluorescence background extends from λ_{SH} towards longer wavelengths. Adapted from Reference [176].

can be identified. They belong to the diffraction orders of the generated second-harmonic signal and are denoted by $(k_x, k_y) = (m, n)$ with m and n being -1, 0, or 1. The diffraction orders with $|m| = |n| = 1$ can, in principle, be emitted into air for excitation wavelengths below 960 nm. Nevertheless, their contribution cannot be detected due to the limited collection angle of the NA $= 0.75$ objective lens. Higher orders ($m, n \geq 2$) are totally reflected in the samples.

Aside from the spots ascribed to the diffractions orders of the generated second-harmonic, another contribution that is smeared out over the back-focal plane is visible. Its origin can be easier understood when looking at the spectral information. To this end we change the spectrometer operation mode by rotating the grating to its diffraction order. Thereby, we attain a hybrid image with the wavelength replacing the reciprocal space on the horizontal axis. Additionally, the entrance slit is closed to 300 µm to limit the detection to diffraction orders with $(k_x, k_y) = (0, n)$. With this changed operation mode we perform a measurement on the same structure and for the same fundamental wavelength as previously (see Figure 4.12b). The diffraction orders permitted into the spectrometer are still visible and extend to cover a small wavelength range as expected from a second-harmonic signal that is exited by fs-pulses. Extending to the long-wavelength side of these peaks, a broad fluourescence background is visible. We ascribe it to two-photon induced autofluorescence originating from the polymer templates that is still non-zero despite the photoresist recipe containing no photoinitiator (see Section 3.2). Interestingly, the fluorescence is barely visible when the structure is excited at a different fundamental wavelength, *e. g.*, $\lambda_F = 840\,\text{nm}$, even though, at the same time, the intensity of the generated second-harmonic is way larger (see Figure 4.12c). The scale for these two measurements is chosen such that it is saturated at the same intensity to allow for an easier comparison. Another difference shows in how the second-harmonic intensity is distributed among the different diffraction orders. Whereas the orders $(0, -1)$ and $(0, 1)$ are dominating for $\lambda_F = 964\,\text{nm}$, the main part of the intensity goes to the zeroth order, *i. e.*, $(0, 0)$, at $\lambda_F = 840\,\text{nm}$.

These findings align with our expectation to find a nonlinear response that strongly depends on the fundamental wavelength, λ_F, both in its intensity and the emission pattern. To further study this behavior, we perform 111 measurements like the ones shown in Figure 4.12b and c for fundamental wavelengths from 800 nm to 1020 nm. For the moment, the information on the distribution to different orders will be discarded by summing over the vertical reciprocal space axis. The resulting overlay of 111 3D nanolaminated photonic crystal spectra for a structure with a rod spacing of $a = 675\,\text{nm}$ and

a shrinkage corrected ratio of $c/a = 0.8$ is depicted in Figure 4.13a. Again the fluorescence is clearly visible towards long wavelengths. We separate the second-harmonic signal from the fluorescence background by fitting a Gaussian to the peak and linearly interpolating the background in the respective region. By integrating the spectral intensity in the fitted peak and dividing it by the value obtained for the plain nonlinear film at the same excitation wavelength, we, finally, derive the normalized second-harmonic intensity, $I_{2\omega}$, (blue dots) as a function of the fundamental wavelength, λ_F, (see Figure 4.13b). It describes the enhancement achieved by the complex arrangement of the second-order susceptibility tensor dictated by the 3D polymer template. The contribution of the integrated autofluorescence signal is given by the green curve and depicted in the same graph together with the linear transmittance spectrum (red curve) measured on the same structure. Figure 4.13c shows the same measurements performed on a structure with $a = 700\,\text{nm}$ and $c/a = 0.80$. As expected, both structures exhibit a strong spectral dependence of the nonlinear response. Increasing the rod spacing from $a = 675\,\text{nm}$ to $700\,\text{nm}$, results in a shift of both the linear and nonlinear features by approximately $40\,\text{nm}$ towards longer wavelengths. The enhancement of the generated second-harmonic is observed in coincidence with prominent features in the linear spectra of the 3D nanolaminated photonic crystals. On the long-wavelength side of the stop band this enhancement approaches values of 100.

An interesting observation can be made from the behavior of the fluorescence signal. Due to the limited data in the long-wavelength regime, the absolute value is not reliable and, especially, varies among structures with different geometrical parameters. The fluorescence signal is broadband, incoherent, and expected to be unpolarized. Nevertheless, in both the structures it follows the same behavior as the spectrally narrow, coherent second-harmonic signal. Therefore, we conclude that the enhancement of second-harmonic and two-photon induced autofluorescence signal must be based on similar effects. Consequently, phase matching cannot be the dominant mechanism. This finding rather points at reinforced light-matter interactions that influence both coherent second-harmonic generation and incoherent two-photon excited autofluorescence.

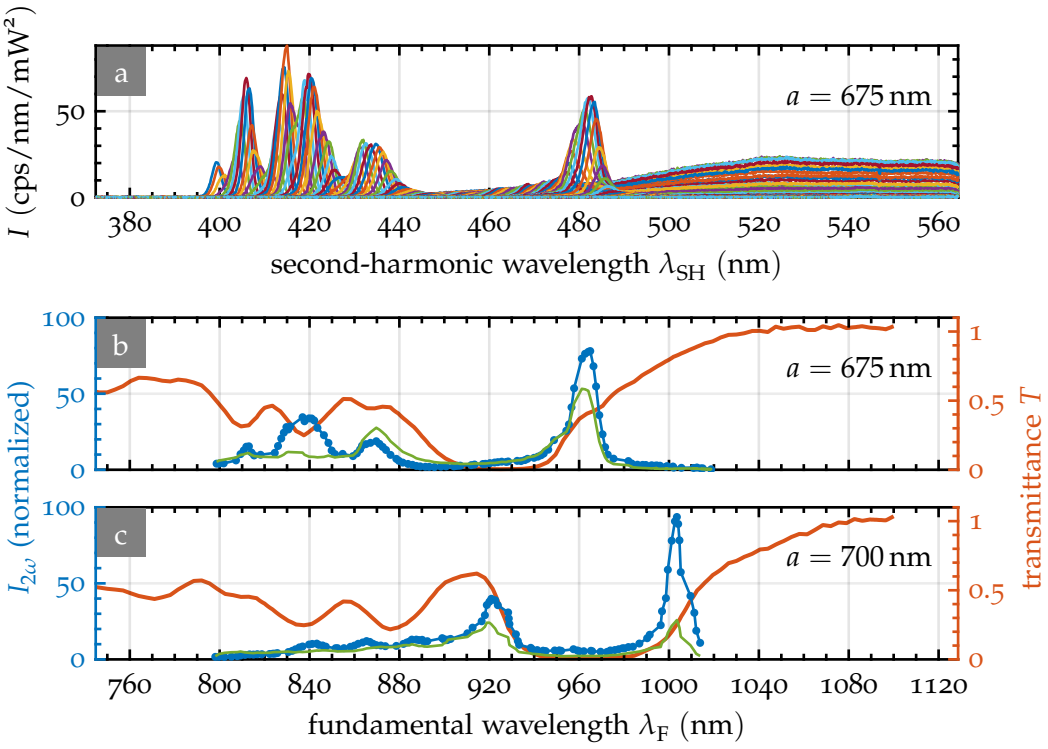

Figure 4.13: Measurements on 3D nanolaminated photonic crystals excited at 111 different fundamental wavelengths each. a) Overlay of 111 spectra showing the signal emitted from a structure with $a = 675\,\mathrm{nm}$. Each spectrum is derived by summing over the vertical reciprocal space axis in measurements of the type depicted in Figure 4.12b and c. The second-harmonic peak and the broad fluorescence background are clearly visible. b) Linear and nonlinear spectrum measured on a structure with a rod spacings of $a = 675\,\mathrm{nm}$ and $c/a = 0.8$. The nonlinear spectrum is derived from panel a) by separately integrating the spectral intensity of the second-harmonic and the fluorescence contribution. Subsequently, the second-harmonic intensity is normalized to the plain film measurement. c) Same measurement as in b), but for a structure with $a = 700\,\mathrm{nm}$. For both rod spacings, a, the second-harmonic intensity, $I_{2\omega}$, (blue dots) and the corresponding fluorescence (green curves) show a similar spectral behavior. The normalized second-harmonic intensity, $I_{2\omega}$, approaches enhancements of two orders of magnitude and is especially strong close to prominent features of the linear transmittance spectra (red curves). Adapted from Reference [176].

The measurements discussed so far suggest that both spectral position and strength of the enhancement of second-harmonic generation depends critically on the geometrical parameters of the photonic crystal template. This dependence is further investigated by varying the rod spacing, a, the filling fraction, f, and the ratio of axial lattice constant to rod spacing, c/a, in the following. Due to the mutual influence these parameters have on each other during fabrication, a systematic variation is not easily achieved. Nevertheless, we have performed the sweeps such that the change in the "deliberately"varied parameter is large as compared to the fluctuations of the parameters that are kept constant.

Figure 4.14a shows the measurements on structures with rod spacings of $a = 650\,\text{nm}$, $675\,\text{nm}$, and $700\,\text{nm}$. All other writing parameters and the ratio of $c/a = 0.8$ are fixed. Again the peak of the second-harmonic enhancement shifts towards longer wavelengths for larger rod spacing, a, following the shift in the linear spectra. As compared to the structures with nominally identical ratios of c/a and with $a = 675\,\text{nm}$ and $a = 700\,\text{nm}$ depicted in Figure 4.13b and c, respectively, these spectra show stop bands at considerably shorter wavelengths. Additionally, the maximum enhancement is way lower. We ascribe both observations to the fact that the measurements depicted in Figure 4.14a stem from structures that were fabricated at lower mean writing powers resulting in smaller dimensions of the rod semiaxes and, therefore, a smaller filling fraction, f.

The dependence of the maximum enhancement on the filling fraction is further studied in 3D nanolaminated photonic crystals fabricated at different DLW writing powers, P, and, hence, with different filling fractions, f, (see Figure 4.14b). We denote the structures written at values of $P = 1\,\text{mW}$, $1.2\,\text{mW}$, and $1.3\,\text{mW}$ by low, medium, and high filling fraction, f, respectively. The rod spacing and the ratio of axial lattice constant to rod spacing are nominally identical with $a = 675\,\text{nm}$ and $c/a = 0.8$, respectively. Just looking at the peak value of the enhancement that coincides with the long-wavelength side of the stop band, suggests that there is a sweet spot for

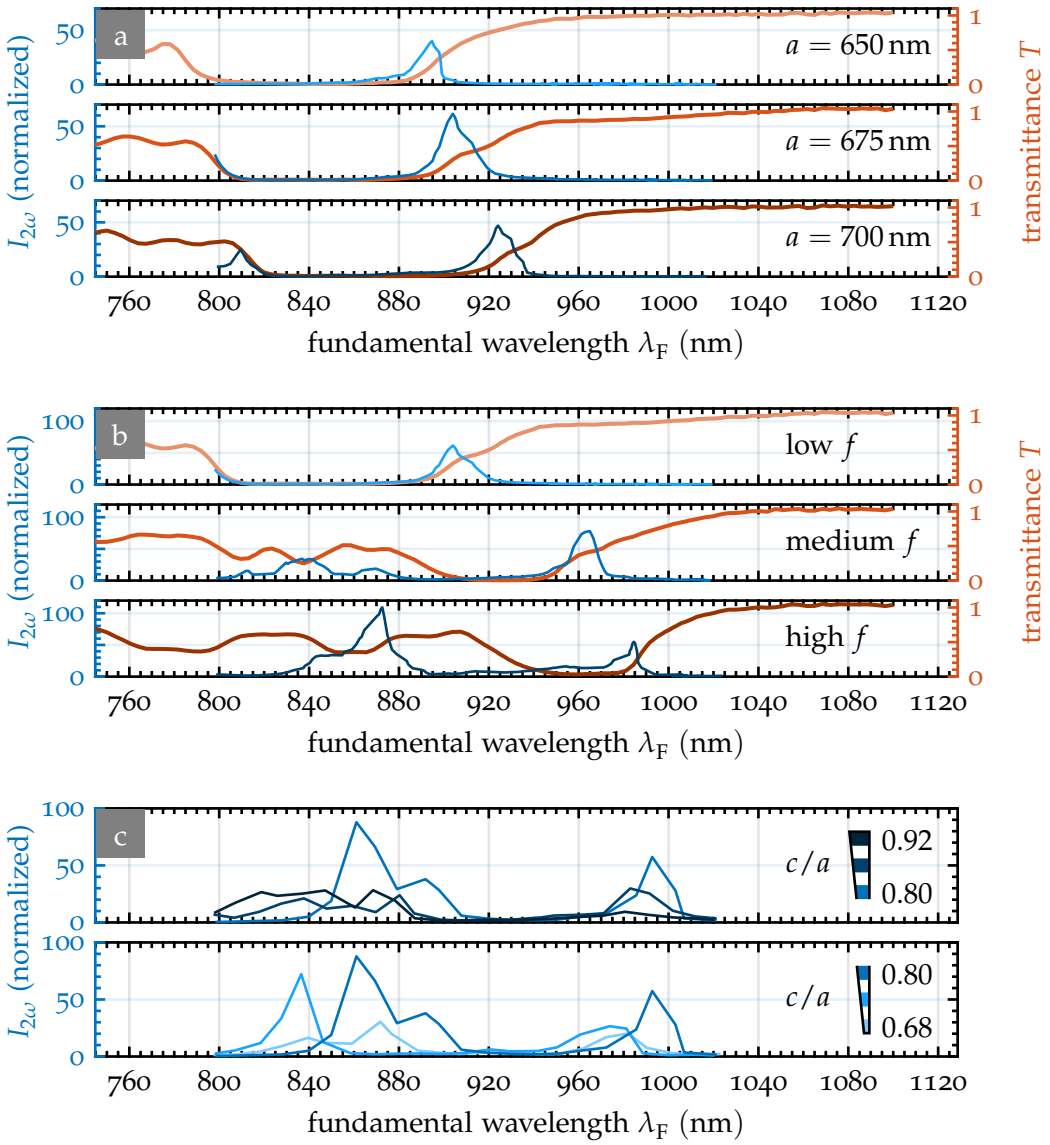

Figure 4.14: Measurements on 3D nanolaminated photonic crystals with different a) rod spacing, a, b) filling fraction, f, and c) ratio of c/a. The second-harmonic enhancement peaks shift with the linear spectra. Additionally, the maximum achievable enhancement varies for different geometrical parameters. This is particularly evident for different values of c/a (panel c). The enhancement decreases with increasing deviation from the optimal value of $c/a = 0.80$ towards both larger and smaller values.

the geometrical parameters. It also seems that these optimal parameter values are different for enhancements observed at different spectral positions with respect to the linear spectra: Whereas the maximum enhancement at the long-wavelength edge of the stop band is observed for medium f, the enhancement around the second pronounced transmittance dip reaches its maximum value, even exceeding a factor of 100, for high f.

Finally, we vary the ratio c/a from a shrinkage-corrected value of 0.68 to 0.92 for a given rod spacing of $a = 675\,\mathrm{nm}$ and otherwise presumably fixed parameters. The measurements depicted in Figure 4.14c reveal the critical influence the ratio of axial lattice constant to rod spacing, c/a, has on the second-harmonic enhancement. The linear spectra are not depicted for the sake of clarity. Again only looking at the peak at long wavelengths, the maximum enhancement increases with c/a and reaches an optimum for $c/a = 0.80$. For even larger ratios the performance decreases rapidly. After having excluded phase matching as the dominant mechanism leading to second-harmonic enhancement in our structures, this finding allows to further specify the responsible mechanism leading to reinforced light-matter interactions. Slow-light effects occurring at the edges of the stop band seem to be a valid assumption at first, but they do not agree with the observed behavior for varying values of c/a. The effect should persist for values both larger and smaller than $c/a = 0.8$. Therefore, we ascribe the second-harmonic enhancement in our structures to reinforced light-matter interactions due to the excitation of resonant 3D nanolaminated photonic crystal modes that lead to a strongly enhanced field strength. We will base the further discussion on this assumption and will confirm it using numerical calculations.

The measurements discussed so far have been performed without paying attention to the polarization of the generated second-harmonic signal. Using a polarizer and a half-wave plate as described in Section 3.4, we repeat the measurement depicted in Figure 4.12b. Figure 4.15a and b show the x- and y-polarized contributions to the generated intensity, respectively. The fundamental signal is polarized along the x-direction and normally

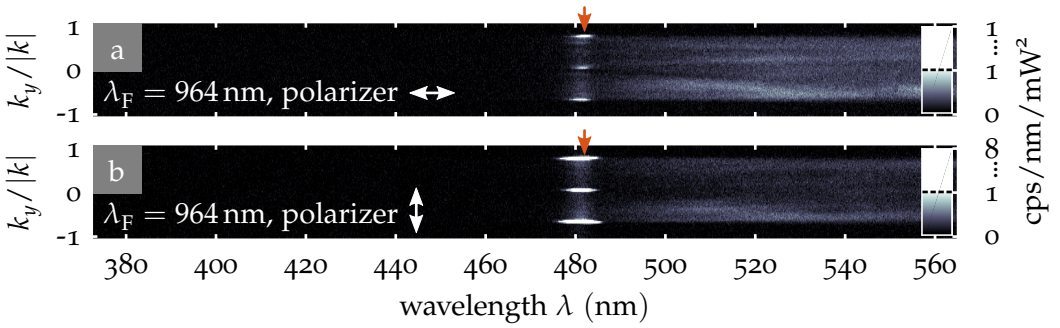

Figure 4.15: Polarization resolved version of the 3D nanolaminated photonic crystal measurements shown in Figure 4.12b. The fundamental beam at a wavelength of $\lambda_F = 964\,\text{nm}$ is polarized along the x-direction. The polarizer allows a) x- and b) y-polarized light into the spectrometer. In agreement with our expectations, the fluorescence is polarization independent. This is not true for the signal associated with the generated second-harmonic: Here, the y-polarized contribution is clearly dominant. Nevertheless, a small part of the second-harmonic is also polarized along the x-direction and shows a non-vanishing intensity in the zeroth diffraction order. In the ideal case this contribution is forbidden by symmetry. Adapted from Reference [176].

incident at a fundamental wavelength of $\lambda_F = 964\,\text{nm}$. The main part of the detected second-harmonic signal is polarized along the y-direction. As before the zeroth order is weaker as compared to the diffraction orders $(0,-1)$ and $(0,1)$. What is surprising is the contribution of x-polarized second-harmonic in the zeroth order: It is weak and just slightly stronger than the the fluorescent background, but, nevertheless, non-zero. Based on symmetry arguments there should be no second-harmonic emission into the zeroth order with the same polarization as the fundamental beam incident at an angle of 0° on a perfectly centrosymmetric 3D nanolaminated photonic crystal. Therefore, we will have to reconsider our assumptions for the numerical evaluation of the investigated 3D nanolaminated photonic crystals: Possible imperfections in the structures and slightly oblique incidence angles of the fundamental beam cause clearly measurable deviations from the ideal case and have to be taken into account to develop a thorough understanding.

4.2.4 Numerical Calculations

With the experimental results on the second-harmonic generation in 3D nanolaminated photonic crystals at hand, we will use numerical calculations to reproduce the findings, identify the responsible effects, and study the influencing factors in more detail. The FEM models for the individual calculations are set up as described in Section 3.6. Based on the experimental observations, we were already able to exclude phase matching and slow-light at the stop band edges as the dominant effects leading to enhanced second-harmonic generation. Therefore, we will focus our discussion on reinforced light-matter interactions due to resonantly excited 3D nanolaminated photonic crystal eigenmodes.

The lateral periodicity of the 3D nanolaminated photonic crystals leads to coupling of eigenmodes to radiation modes in both air and substrate just like in the case of 2D photonic crystal slabs and periodically modulated slab waveguides (see Section 2.5 and 2.6). We will make use of this analogy and develop a more intuitive understanding of the observed effects in our structures based on the resemblance to the behavior of modes in asymmetric slab waveguides. The eigenmodes that allow for coupling to radiation modes in air and substrate are usually referred to as guided resonances rather than as guided modes. We start by identifying these resonances using eigenmode calculations. Due to their finite lifetime, guided resonances are numerically described by a complex valued eigenfrequency, ω. From this eigenfrequency we can determine the quality factor, Q, according to Equation 2.32. To allow for a better comparison with experiments, we will discuss the numerical results in terms of the free-space wavelength given by $\lambda = c_0 2\pi/\mathrm{Re}\{\omega\}$. For the moment, we will limit the calculations to modes that can be excited by normally incident light mimicking the idealized experimental configuration. Therefore, we look for Bragg diffracted eigenmodes with the appropriate Floquet-Bloch periodic boundary conditions defined by $k_x = k_y = m \cdot 2\pi/a$ and integer m (see Section 3.6). If not specified otherwise, the calculations are performed for the following geometrical parameters based on the analysis of the actually fabricated structures: $N_z = 6$, $a = 675\,\mathrm{nm}$, $c/a = 0.8$, $r_x = 62\,\mathrm{nm}$, AR $= 2.5$, and $d_{\mathrm{ALD}} = 27\,\mathrm{nm}$. Additionally, we start by focusing

on the second-harmonic enhancement peak at the long-wavelength edge of the stop band that can be found in all measurements shown above.

The results of the eigenmode calculations show two guided resonances with a strong field confinement in the region of the 3D nanolaminated photonic crystal at a free-space wavelength of $\lambda = 964\,\mathrm{nm}$. The two nearly degenerate eigenmodes are almost the same if one exchanges the x- and y-axis along with the components of the electric field amplitude $\tilde{E}_x$ and $\tilde{E}_y$. The symmetry is only broken due to the finite extent of the structure in the z-direction. Nevertheless, based on symmetry considerations only one of these modes can be excited for light with x- (or y-)polarization incident on an ideal structure. We will consider the case of x-polarized incident light and call the eigenmode that can be coupled to "bright"and the other one "dark". The strong field confinement in the structure results in a high quality factor of the two guided resonances with $Q = 1379$ and $Q = 2162$ for bright and dark mode, respectively. The bright mode exhibits a standing-wave pattern with the field being concentrated in the domain of the nanolaminated photonic crystal (see Figure 4.16a). Nevertheless, a finite field amplitude is observed in both air and substrate allowing for coupling to this resonance. If this bright guided resonance is indeed excited, it would lead to a strongly enhanced field at the fundamental wavelength and, consequently, to an enhanced second-harmonic generation. It is worth noting that the bright mode field distribution shows resemblance with that of the fundamental mode of an asymmetric slab waveguide depicted in Figure 2.5a. Based on this resemblance we call this bright eigenmode the fundamental guided resonance of our structure. This analogy extends to higher order modes. From the eigenmode calculations we are able to identify a guided resonance similar to a waveguide mode with $m = 1$ (see Figure 4.16b). This mode is found at a wavelength of $\lambda = 965\,\mathrm{nm}$ and has a low quality factor of $Q = 70$. The photonic crystal slab seems to be to thin to properly support this mode that couples strongly to the air and substrate modes. Therefore, it is barely confined in the structure and of minor interest to us, at least, for the given number of axial unit cells, N_z.

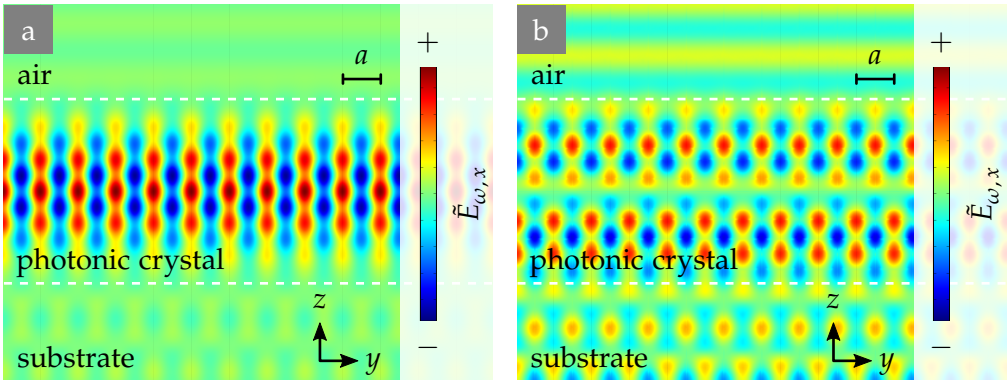

Figure 4.16: Electric field distribution of guided resonances in a 3D nanolaminated photonic crystal with $a = 675\,\text{nm}$ and $c/a = 0.8$ determined from eigenmode calculations. a) The bright eigenmode at $\lambda = 964\,\text{nm}$ has a quality factor of $Q = 1379$ and shows a strong field confinement in the photonic crystal. Its field distribution resembles the fundamental waveguide mode in an asymmetric slab waveguide, but with a finite field strength outside the guiding layer. b) The next higher order mode has a quality factor of $Q = 70$ and is found at $\lambda = 965\,\text{nm}$. It shows a weak field confinement and strong coupling to substrate and air modes. Adapted from Reference [176].

The observed position of the fundamental guided resonance is in excellent agreement with the position of the enhancement peak at the long-wavelength edge of the stop band measured on a structure with identical geometrical parameters (see Figure 4.13b). To confirm this correlation between guided resonance and second-harmonic enhancement, we perform eigenmode calculations for different geometrical parameters and compare them with the experimental findings. It was shown that the ratio of axial lattice constant to rod spacing, c/a, has a strong influence on the maximal achievable second-harmonic enhancement (see Figure 4.14c). To replicate this finding, we run eigenmode calculations for different values of c/a and extract the quality factor, Q, and the wavelength, λ, for the previously identified bright guided resonance depicted in Figure 4.16a. This parameter sweep shows a strong dependence of Q on the value of c/a (see Figure 4.17). For $r_x = 62\,\text{nm}$ the quality factor, Q, peaks for $c/a = 0.79$ at a value of Q exceeding 10^3. This result is in good agreement with the experimentally observed optimal value of $c/a = 0.8$. Deviations from this optimum value of c/a lead to a strongly

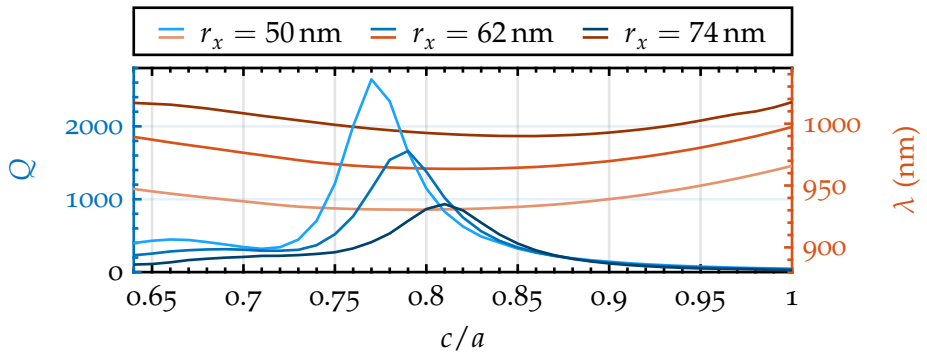

Figure 4.17: Quality factor, Q, and wavelength, λ of the fundamental guided resonance associated with the enhancement peak at the long-wavelength edge of the stop band for different values of the ratio c/a and a fixed rod spacing of $a = 675\,\mathrm{nm}$. The eigenmodes are calculated for $r_x = 50\,\mathrm{nm}$, 62 nm, and 74 nm with a maximum of Q observed at $c/a = 0.77$, 0.79, and 0.81, respectively. Both for larger and smaller values of c/a, the quality factor, Q, decreases rapidly. The wavelength, λ, of the guided resonance increases with r_x due to an increase of the effective refractive index. Adapted from Reference [176].

decreased quality factor, Q, of the guided resonance that goes hand in hand with a small second-harmonic enhancement observed in the experiments. The dependence of the quality factor, Q, on c/a can be understood as follows: For small ratios c/a, the structure is compressed in the axial direction. The mode in this thin 3D nanolaminated photonic crystal leaks strongly and, hence, has a small Q just as it would be the case for a slab waveguide. At the other end, for large values of c/a, the filling fraction, f, and, consequently, also the effective refractive index of the structure is greatly reduced. Once again this leads to poor guiding and a small value of Q.

Repeating the numerical parameter sweep for $r_x = 50\,\mathrm{nm}$ and $r_x = 74\,\mathrm{nm}$ reproduces this behavior (see Figure 4.17). The optimal values of c/a are slightly shifted due to the changed effective refractive index. Additionally, we find an increase of the maximum quality factor, Q, for decreasing values of r_x. We compare these results at a fixed value of c/a with the experimental findings on structures with a shrinkage-corrected value of $c/a = 0.8$ and

different filling fractions, f, shown in Figure 4.14b. In agreement with the measured position of the enhancement peak, the guided resonance shifts towards larger wavelengths with increasing rod semiaxis, r_x, and, consequently larger filling fraction, f. Additionally, in the experiments a second-harmonic enhancement peak value that is largest for medium f was observed. We want to neglects other effects for the moment and ascribe this behavior solely to different values of Q. In the calculations this experimental finding can only be reproduced if one assumes that the ratio c/a of the structures is slightly above the optimal value found for $r_x = 62\,\mathrm{nm}$. Taking for example $c/a = 0.8$, the quality factor, Q, of the guided resonance is largest for $r_x = 62\,\mathrm{nm}$ (corresponding to medium f) and, therefore, would allow for an explanation of the measured data.

The good agreement between experimental findings and eigenmode calculations suggests that a guided resonance is indeed responsible for the strong second-harmonic enhancement found at the long-wavelength edge of the stop band. To make sure this mode is actually excited and the source of the observed effects, we mimic the experiments using calculations that follow a perturbative approach. The involved steps are briefly summarized in the following and described in more detail in Section 3.6. These calculations are quite time consuming and will be discussed for the same parameters as given at the beginning of this section. Especially, we set $a = 675\,\mathrm{nm}$ and $c/a = 0.8$. In the first step, the field distribution and the linear transmittance, T, through the structure is determined for a plane wave at the fundamental wavelength, λ_F. The wave is incident from air and propagates along the $-z$-direction (see Figure 4.8). Next, we determine the second-order nonlinear polarization in the nonlinear nanolaminate based on the previously obtained fundamental field distribution and the properly rotated second-order susceptibility tensor. Finally, the amplitude of the electric field distribution, $\tilde{\boldsymbol{E}}_{2\omega}$, at the second-harmonic wavelength, λ_SH, is calculated. An example for $\lambda_\mathrm{F} = 964\,\mathrm{nm}$ is depicted in Figure 4.18a and b. It shows a second-harmonic field that exhibits a standing-wave pattern and radiates both into forward and backward direction, *i. e.* into substrate and air, respectively. We take the z-component of the time averaged Poynting vector as a measure for the second-harmonic intensity, $I_{2\omega}$, emitted into the forward direction. To allow

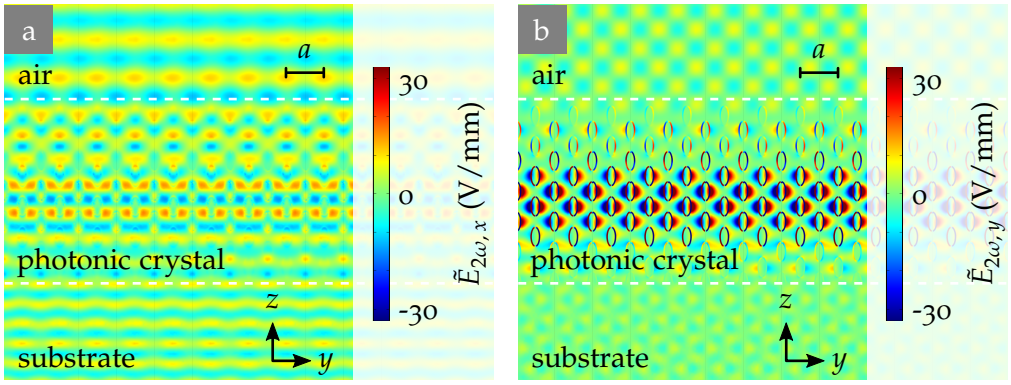

Figure 4.18: a) $\tilde{E}_{2\omega,x}$ and b) $\tilde{E}_{2\omega,y}$ component of the calculated electric field distribution at the second-harmonic wavelength in the yz-plane. The fundamental is a normally incident plane wave at $\lambda_F = 964\,\text{nm}$ that is polarized along the x-direction. The second-harmonic field radiates both into air and substrate and exhibits a standing-wave pattern. Adapted from Reference [176].

for a representation identical to the one used for the experimental data, we run the same calculations for a plane film of the nonlinear nanolaminate and a plane wave impinging at an angle of 45°. The resulting second-harmonic intensity is used to normalize the results calculated for the 3D nanolaminated photonic crystals.

Figure 4.19a depicts the obtained spectrum with the transmitted and reflected second-harmonic intensity denoted by $I_{2\omega,T}$ and $I_{2\omega,R}$, respectively. Both the linear transmittance and $I_{2\omega,T}$ show a good qualitative agreement with the experimental data for a structure with identical geometrical parameters (see Figure 4.13b). We find several peaks of the second-harmonic enhancement that are once again close to prominent features of the linear transmittance spectrum. At the long wavelength-edge of the stop band, an enhancement factor of close to 500 is determined in contrast to an experimentally observed value of around 100. We ascribe this discrepancy to angular and spectral averaging in the experiments that are caused by the both the finite opening angle of focusing and the finite bandwidth of the incident fs-pulses. Having a closer look at the transmittance at the long-wavelength edge of the stop

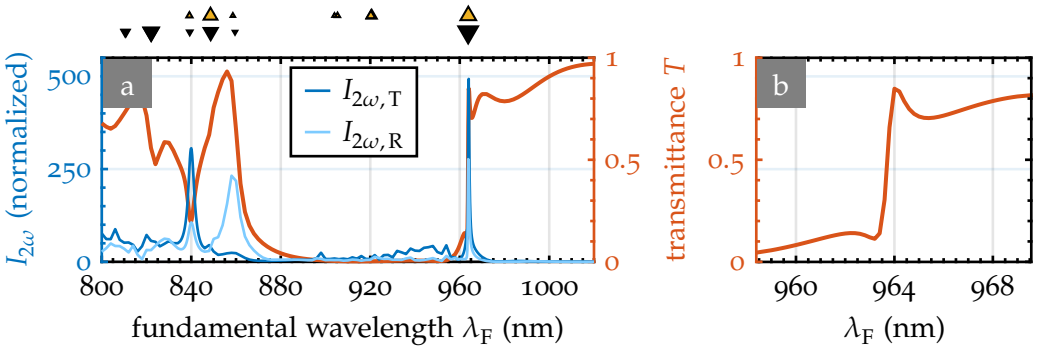

Figure 4.19: a) Calculated linear and nonlinear spectra of a 3D nanolaminated photonic crystal with $a = 675\,\mathrm{nm}$ and $c/a = 0.8$. The peaks of the transmitted and reflected second-harmonic intensity, $I_{2\omega,\mathrm{T}}$ and $I_{2\omega,\mathrm{R}}$, respectively, coincide with prominent features of the linear spectrum. Furthermore, $I_{2\omega,\mathrm{T}}$ reproduces the features observed in experiments on a structure with similar parameters (see Figure 4.13b). The upwards pointing yellow triangles and the downwards pointing black triangles indicate the calculated positions of bright and dark eigenmodes, respectively. The size of the triangles is proportional to the quality factor, Q, of the guided resonances. For the sake of clarity, only modes with $Q \geq 100$ are depicted. b) The zoom into the calculated linear transmittance (see panel a) at the long-wavelength edge of the stop band shows a sharp Fano-shaped feature. Adapted from Reference [176].

band, we find a sharp Fano-shaped feature (see Figure 4.19b) that arises as a consequence of coupling between a discrete mode (presumably the guided resonance) and a continuum of states [177]. Such sharp features are not observable in the measured data due to the angle averaging caused by the finite opening angle of focusing optics in the experiments. The field distribution at the second-harmonic peak for $\lambda_\mathrm{F} = 964\,\mathrm{nm}$ confirms the origin of the discrete state and our hypothesis on the role of the guided resonance: Both the position and the field distribution coincide with the guided resonance previously obtained from eigenmode calculations (see Figure 4.16a). Hence, the eigenmode is indeed excited. It leads to a fundamental field that is enhanced by a factor of 14 as compared to the incident field strength of $70\,\mathrm{V/\mu m}$ (not depicted).

Obviously, field enhancement at the fundamental wavelength is not the only factor determining the efficiency and, hence, the strength of second-harmonic generation. The coupling strength to the guiding resonance, the mode overlap between fundamental and second-harmonic mode, and, especially dealing with propagation lengths larger than the coherence length, the phase mismatch are of great importance [6]. All these factors are expected to vary with the geometrical parameters of the investigated structures. This is beautifully illustrated when comparing the second-harmonic intensity at the short-wavelength edge of the stop band in Figure 4.13b and c: Whereas no enhancement is observed for $a = 675\,\mathrm{nm}$, a well pronounced peak is found for $a = 700\,\mathrm{nm}$. In the calculations this additional influence becomes evident when looking at the position and quality factor, Q, of guided resonances and the actually calculated second-harmonic peaks in Figure 4.19a. The yellow triangles pointing upwards and the black triangles pointing downwards denote bright and dark eigenmodes, respectively. The triangle size encodes the quality factor, Q, of the respective eigenmode. Whereas a large Q results in a strong enhancement at $\lambda_\mathrm{F} = 964\,\mathrm{nm}$, this correlation is not always given for smaller wavelengths. Another interesting finding that is explained by the same reasoning is that some peaks show a strong enhancement in both transmitted and reflected second-harmonic intensity. In contrast, only the reflected intensity, $I_{2\omega,\mathrm{R}}$, is enhanced at the short-wavelength edge of the stop band.

At this point we can, finally, summarize the operation principle leading to the observed enhancement of second-harmonic generation in 3D nanolaminated photonic crystals: The structure acts as a leaky, asymmetric waveguide with the grating coupler functionality given by the periodicity of the underlying photonic crystal. Incident light is Bragg diffracted into the photonic crystal slab and is strongly enhanced if it resonates with a guided resonance of the structures. For the case of normal incidence a standing wave is formed. The reinforced light-matter interaction at the fundamental wavelength is, basically, a resonant cavity effect and leads to an enhanced nonlinear polarization. The actually observed second-harmonic intensity is additionally influenced by the mode overlap and the phase mismatch of the respective modes at the fundamental and second-harmonic wavelength. The generated

signal is emitted into directions that are dictated by the periodicity of the 3D nanolaminated photonic crystal.

The results discussed so far show a good overall agreement with the experimental data. Nevertheless, looking at the numerical results in more detail also reveals some important discrepancies that are still unexplained. Figure 4.20a and b shows the second-harmonic intensity emitted to different diffraction orders at $\lambda_F = 840\,\text{nm}$ as observed in calculations based on the perturbative approach and experiments, respectively. The former is derived by determining the Fourier transform of the generated second-harmonic field in a xy-plane in the far field. Only orders that are also detectable in the experiments are taken into account. Whereas the experimental data shows a dominant contribution to the zeroth diffraction order, the numerical results suggest that the main part of the signal goes to the orders $(-1, 0)$ and $(1, 0)$. It turns out that such delicate details in the numerical calculations are strongly influenced by the choice of geometrical parameters. Therefore, we cannot assume to hit the parameters that exactly replicate the experiments.

It is still worth discussing this issue a little longer to deepen our understanding of the involved mechanisms. As highlighted in the discussion of polarization-resolved measurements, there is a part of the second-harmonic signal polarized identical to the normally incident fundamental beam that is emitted into the zeroth diffraction order (see Figure 4.15a). We argued that this contribution is forbidden in an ideal centrosymmetric structure and that its existence hints at the significant influence structural imperfections and deviations from the idealized excitation conditions due to misalignment and the finite angle of incidence have on the measurements. Imperfections can lead to breaking of the selection rule for what we call bright and dark modes, thereby, leading to a mixing between the modes.

Taking the peak at $\lambda_F = 840\,\text{nm}$ detected transmission as an example, we want to demonstrate that mode mixing in combination with oblique incidence at an angle of up to 3° allows explaining the discrepancy between experiment and calculations. Obviously, it is hard to determine the exact circumstances

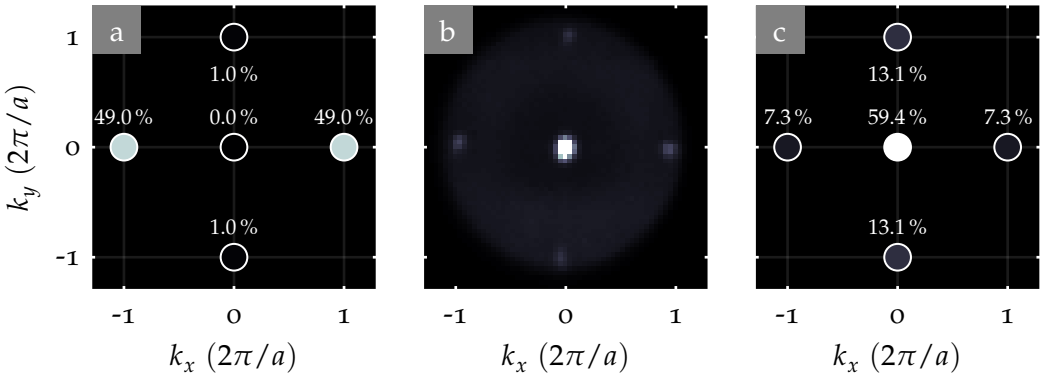

Figure 4.20: Contribution of the second-harmonic signal to different diffraction orders at a fundamental wavelength of 840 nm. a) Relative intensity calculated from the second-harmonic field distribution in the far field as derived from the perturbative approach. The main part goes to the orders $(-1, 0)$ and $(1, 0)$. b) The experimentally observed reciprocal space emission shows a totally different picture with the intensity mainly going into the zeroth order. c) Due to deviations of the structure and the excitation conditions from the assumed ideal case, mode mixing and slightly oblique angles of incidence have to be taken into account. A superposition of bright and dark eigenmodes that can be coupled to for an incidence angle of 3° (see Figure 4.21) is used to define the nonlinear source term. The resulting second-harmonic field distribution is again analyzed in the far field and the relative intensity shows a good agreement with the experimental findings. Adapted from Reference [176].

of mode mixing, but it turns out that it is sufficient to use the sum of the two eigenmodes that can be excited by a plane wave incident at an angle of 3° and are close to $\lambda = 840$ nm (see Figure 4.21a and b) to define the nonlinear polarization. The second-harmonic field generated for this configuration can be analyzed and gives the relative intensity distribution depicted in Figure 4.20c. It shows a very good agreement with the experimentally observed pattern and, therefore, confirms the need to incorporate effects due to imperfections in the structure and the excitation conditions to arrive at a complete picture of the second-harmonic generation in 3D nanolaminated photonic crystals.

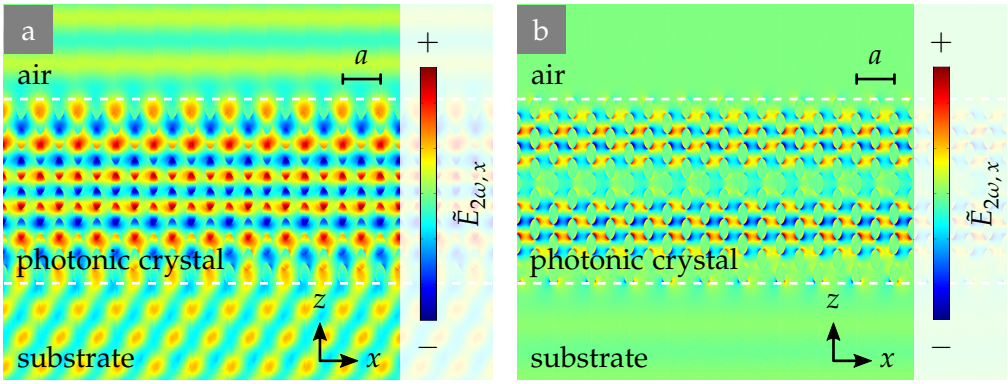

Figure 4.21: a) Bright and b) dark eigenmodes close to $\lambda = 840\,\text{nm}$ calculated for boundary conditions that allow for coupling to a plane wave incident at an angle of 3°. A linear combination of these modes is used to determine the nonlinear source term in order to account for experimental imperfections. Adapted from Reference [176].

4.2.5 Discussion

The experimental data and the numerical calculations presented in the previous sections have shown the expected interplay of woodpile photonic crystal templates and the conformally deposited second-order nonlinear nanolaminate. We have understood the origin of the observed second-harmonic enhancement of up to two orders of magnitude and demonstrated that deviations from the ideal numerical model are necessary to explain important aspects of the experimental data. Nevertheless, the performed study is just the first step to understand and profit from the complex and flexible spatial arrangement of the second-order nonlinear susceptibility made possible by the presented fabrication method.

Further experiments on 3D nanolaminated photonic crystals should investigate the influence of the number of axial unit cells, N_z, to demonstrate the fact that the observed effect is not limited to structures with $N_z = 6$ used in the presented measurements. In analogy to the behavior of a dielectric slab waveguide, we expect a stronger field confinement in the 3D nanolaminated photonic crystal and, therefore, a larger quality factor, Q. We have performed this parameter study in numerical calculations and find the

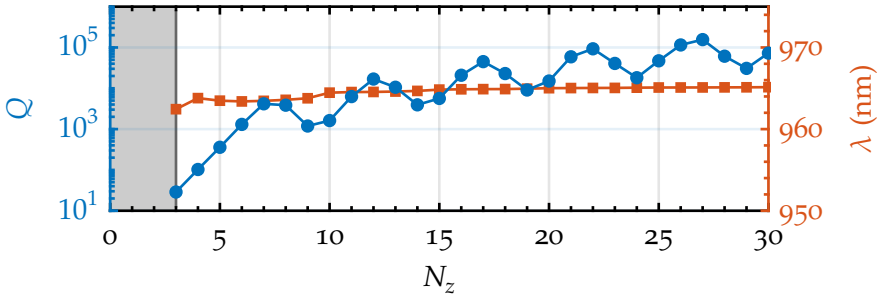

Figure 4.22: Quality factor, Q, and wavelength, λ, of the fundamental guided resonance versus the number of axial unit cells, N_z. The quality factor, Q, shows a strong increase with N_z that is ascribed to a stronger mode confinement in the structure. A similar behavior and the observed cutoff of the fundamental mode (gray line) are well-known for asymmetric slab waveguides.

results in agreement with our expectations (see Figure 4.22a). The quality factor, Q, of the fundamental guided resonance grows rapidly with N_z and exceeds values of 10^5. Additionally, we observe a cutoff of the fundamental mode that is well-known from asymmetric slab waveguides (see Section 2.6) for $N_z < 3$. The possibility to tune the quality factor is also found in 2D photonic crystal slabs albeit accomplished by reducing the modulation of the dielectric function instead of increasing N_z [55]. The oscillations of the quality factor, Q, are attributed to the spatial extent of the guided resonance that shows a nonlinear, step-wise growth with N_z. This leads to a strongly enhanced overlap with both substrate and air layer for certain values of N_z. Another aspect that has been neglected so far is the study of the mode at the second-harmonic wavelength. In 2D photonic crystal slabs it has been shown that a yet stronger enhancement of the nonlinear response can be achieved if both the fundamental and the second-harmonic modes are tuned to guided resonances of the structure [63, 64]. A detailed analysis of the eigenmodes at the second-harmonic wavelength and appropriate tuning of the geometrical parameters should enable doubly resonant second-harmonic interactions in 3D nanolaminated photonic crystals.

A variety of other ways to enhance and tailor the nonlinear response for a given application have been discussed in Section 2.5. Based on the fabrication

approach involving photonic crystal templates presented in this work, one could, for example, aim at achieving (quasi-)phase matched second-order interactions. For this purpose it is important to identify the modes that are excited at all interacting wavelengths and tune them appropriately. For second-harmonic generation an easy way would be to chose the second-harmonic wavelength such that it lies in the anomalous dispersion regime of the first stop band. In this case, the waves at both wavelengths are basically plane waves and only have to be matched in terms of their refractive indices. Another way is the fabrication of second-order nonlinear photonic crystals that show a tailored distribution of the second-order susceptibility but only minimal spatial variations in the linear susceptibility. This can be achieved by completely filling the air gaps in the ALD step. In case the contrast in the dielectric functions is still too large, one can implement more sophisticated approaches based on inversion or even double inversion using materials with a suitable linear and a vanishing second-order susceptibility [127].

5 Chapter 5 Conclusion

In the scope of this thesis, a second-order nonlinear nanolaminate was developed and characterized. Conformally depositing this nonlinear film on a "printed"3D photonic crystal, we were able to fabricate what we call 3D nanolaminated photonic crystals. The synergies arising from the interplay of nonlinear nanolaminates and 3D photonic crystals were studied and shown to result in an enhancement of second-harmonic generation. This chapter summarizes the main results and gives an outlook to possible future developments.

The two main fabrication methods central to this thesis were introduced in the first part of Chapter 3. Atomic-layer deposition was described in Section 3.1 and used for the growth of second-order nonlinear nanolaminates. Section 3.2 covered the basics of 3D direct laser writing. The features necessary to allow for "printing"of 3D photonic crystals with the desired geometrical parameters were highlighted. As compared to the conventional configuration, we used a greatly reduced excitation wavelength and, therefore, benefited from a substantial improvement in resolution.

The second part of Chapter 3 dealt with the methods used for sample characterization. The second-order nonlinear response was quantified based on the generated second-harmonic signal. Investigating the plain nonlinear nanolaminates, we were interested in optimizing and, finally, determining the full second-order susceptibility. In contrast, the focus in studying 3D nanolaminates photonic crystals, was on the directional and spectral characteristics of the second-harmonic emission at different fundamental wave-

lengths. The setups built and adjusted to meet the respective requirements were presented in Section 3.4. To supplement the optical measurements on nonlinear nanolaminates, we relied on structural information derived from X-ray diffraction measurements. The technique was described in Section 3.5 and allowed for correlating structural changes with the observed second-order nonlinear response. A deeper understanding on the dominating mechanisms in 3D nanolaminated photonic crystals was obtained through numerical calculations based on the finite element method. Its implementation was discussed in Section 3.6.

Chapter 4 covered the results obtained in the scope of this thesis. In Section 4.1 the design, fabrication, and characterization of second-order nonlinear ZnO/Al_2O_3 nanolaminates grown by atomic-layer deposition was presented. After having identified the main factors influencing the nonlinear response of ZnO thin films, we have studied the individual optical and structural effects by comparing the properties of three different types of samples. Pure ZnO films were shown to exhibit a nucleation delay and randomly oriented crystallites leading to cancellation of the second-harmonic signal generated in different domains. An Al_2O_3 seed layer was demonstrated to limit the influence of the substrate and enforce a preferential orientation of the ZnO crystallite growth. This structural change was found to be correlated with an increase of the generated second-harmonic power. The latter could be further enhanced to a factor of close to 40 as compared to the pure ZnO film by introducing additional intermediate Al_2O_3 layers. We have ascribed this observation to two effects: The intermediate Al_2O_3 layers cause an improved ZnO crystallite orientation throughout the entire film thickness. Additionally, they disrupt the ZnO crystallite growth and, thereby, maximize the second-order nonlinear contribution from grain boundaries and interfaces. Based on these findings, we have performed extensive parameter sweeps to optimize the individual layer thicknesses in the ZnO/Al_2O_3 nanolaminate. Finally, it was shown that the films are well-described by effective material parameters and the full second-order susceptibility tensor was determined. The largest tensor element was found to be $\chi^{(2)}_{zzz} = -4.0\,\frac{\mathrm{pm}}{\mathrm{V}}$ and is comparable to the elements of conventional bulk nonlinear crystals.

Section 4.2 dealt with 3D nanolaminated photonic crystals. These structures show a complex spatial distribution of the second-order susceptibility tensor as a consequence of the conformal deposition of second-order nonlinear nanolaminates on 3D photonic crystals. Measurements of the second-harmonic intensity emitted from 3D nanolaminated photonic crystals have shown a strong spectral dependence. Additionally, enhancements of up to two orders of magnitude as compared to the plain nanolaminates were found in coincidence with the spectral positions of prominent features in the linear spectra. Based on the detected two-photon induced autofluorescence stemming from the polymer template and sweeps of the 3D photonic crystal parameters, the mechanism responsible for the detected enhancement was narrowed down to reinforced light-matter interactions. The associated guided resonances at the fundamental wavelength were identified by means of numerical calculations and shown to result in a strongly enhanced electric field strength and, consequently, an enhancement of the second-order nonlinear polarization in the structure. Additionally, the influence of other mechanisms determining the observed second-harmonic enhancement was highlighted. The calculations were shown to be in good agreement with the experimental findings. Nevertheless, discrepancies were found in terms of the second-harmonic intensity emitted to different diffraction orders. To reproduce the experimentally detected emission pattern numerically, the effect of structural imperfections and a slightly oblique incidence of the fundamental beam had to be taken into account.

The crucial role light-matter interactions play in our everyday life was already stated in the introduction. By acquiring a certain understanding of these processes both in the linear and in the nonlinear regime, mankind has managed to make use of light-matter interactions for a variety of modern technologies. To further promote this development, it is important to provide materials and approaches that allow for tailored and efficient light-matter interactions not only in the linear, but also in the nonlinear regime. In this context, the results presented in this work can be seen as part of a tool box that facilitates the design and fabrication of integrated optical systems and photonic structures that rely on second-order nonlinear light-matter interactions. The nonlinear nanolaminates are easy to integrate in compact

optical systems and their fabrication by means of atomic-layer deposition is compatible with well-established semiconductor processes. Additionally, they can be combined with 3D printed templates, that are by no means limited to photonic crystals. The resulting structures are purely dielectric and posses a complex distribution of the second-order susceptibility tensor that introduces a high degree of flexibility. At the same time, this poses a challenge as one has to take the distribution and the interacting modes at all frequencies into account to tailor the light-matter interactions to ones needs.

Bibliography

[1] D. A. Bryant and N.-U. Frigaard, "Prokaryotic Photosynthesis and Phototrophy Illuminated", Trends in Microbiology **14**, 488 (2006) (Cited on page 3).

[2] D. Lindley, "Focus: Landmarks - Ruby Red Laser Light Becomes Ultraviolet", Physics **7** (2014) (Cited on pages 3, 10).

[3] T. H. Maiman, "Stimulated Optical Radiation in Ruby", Cah. Rev. The. **187**, 493 (1960) (Cited on pages 3, 10).

[4] E. Garmire, "Nonlinear Optics in Daily Life", Opt. Express **21**, 30532 (2013) (Cited on pages 3, 14).

[5] J. D. Joannopoulos, S. G. Johnson, J. N. Winn, and R. D. Meade, *Photonic Crystals: Molding the Flow of Light*, 2nd ed. (Princeton University Press, 2011) (Cited on pages 5, 22).

[6] P. N. Butcher and D. Cotter, *The Elements of Nonlinear Optics*, 1st ed. (Cambridge University Press, 1991) (Cited on pages 7, 9–11, 13, 19, 69, 131).

[7] J. C. Maxwell, *Treatise on Electricity and Magnetism, Vol. 1*, 3rd ed. (Dover Publications, 1954) (Cited on page 8).

[8] D. J. Griffiths, *Introduction to Electrodynamics*, 3rd ed. (TBS, 1999) (Cited on page 8).

[9] J. D. Jackson, *Classical Electrodynamics*, 3rd ed. (Wiley, 1999) (Cited on page 8).

[10] L. Novotny and B. Hecht, *Principles of Nano-Optics*, 1st ed. (Cambridge University Press, 2006) (Cited on page 8).

[11] R. W. Boyd, *Nonlinear Optics*, 3rd ed. (Academic Press, 2008) (Cited on pages 10, 12, 13, 18).

[12] C. Flytzanis, "Theory of Nonlinear Optical Susceptibilities", in *Quantum Electronics: A Treatise*, edited by H. Rabin and C. L. Tang (Academic Press, 1975), p. 9 (Cited on page 10).

[13] Y. R. Shen, *The Principles of Nonlinear Optics*, 1st ed. (Wiley, 1984) (Cited on pages 13, 19).

[14] P. N. Butcher, *Nonlinear Optical Phenomena*, 1st ed. (Engineering Experiment Station, Ohio State University, 1965) (Cited on page 13).

[15] P. A. Franken, A. E. Hill, C. W. Peters, and G. Weinreich, "Generation of Optical Harmonics", Phys. Rev. Lett. **7**, 118 (1961) (Cited on page 14).

[16] M. Tonouchi, "Cutting-Edge Terahertz Technology", Nat. Photonics **1**, 97 (2007) (Cited on page 14).

[17] C. Koos, J. Leuthold, W. Freude, M. Kohl, L. Dalton, W. Bogaerts, A. L. Giesecke, M. Lauermann, A. Melikyan, S. Koeber, S. Wolf, C. Weimann, S. Muehlbrandt, K. Koehnle, J. Pfeifle, W. Hartmann, Y. Kutuvantavida, S. Ummethala, R. Palmer, D. Korn, L. Alloatti, P. C. Schindler, D. L. Elder, T. Wahlbrink, and J. Bolten, "Silicon-Organic Hybrid (SOH) and Plasmonic-Organic Hybrid (POH) Integration", J. Lightwave Technol. **34**, 256 (2016) (Cited on page 14).

[18] W. Kaiser and C. G. B. Garrett, "Two-Photon Excitation in CaF_2: Eu^{2+}", Phys. Rev. Lett. **7**, 229 (1961) (Cited on page 15).

[19] M. Bass, C. DeCusatis, J. Enoch, V. Lakshminarayanan, G. Li, C. MacDonald, V. Mahajan, and E. V. Stryland, *Handbook of Optics, Third Edition Volume IV: Optical Properties of Materials, Nonlinear Optics, Quantum Optics*, 3rd ed. (McGraw-Hill Education, New York, 2009) (Cited on page 15).

[20] L. Mandelstam and I. Tamm, "The Uncertainty Relation Between Energy and Time in Non-Relativistic Quantum Mechanics", in *Selected Papers*, edited by I. E. Tamm, B. M. Bolotovskii, V. Y. Frenkel, and R. Peierls (Springer, Berlin, 1991), p. 115 (Cited on page 15).

[21] W. Denk, J. H. Strickler, and W. W. Webb, "Two-Photon Laser Scanning Fluorescence Microscopy", Science **248**, 73 (1990) (Cited on page 15).

[22] B. E. A. Saleh and M. C. Teich, *Fundamentals of Photonics*, 2nd ed. (John Wiley & Sons, 2007) (Cited on pages 17, 26).

[23] C. F. Klingshirn, *Semiconductor Optics*, 4th ed. (Springer Science & Business Media, 2012) (Cited on pages 17, 22).

[24] Beer, "Bestimmung Der Absorption Des Rothen Lichts in Farbigen Flüssigkeiten", Ann. Phys. (Berl.) **162**, 78 (1852) (Cited on page 18).

[25] D. A. Kleinman, "Nonlinear Dielectric Polarization in Optical Media", Phys. Rev. **126**, 1977 (1962) (Cited on page 19).

[26] P. D. Maker, R. W. Terhune, M. Nisenoff, and C. M. Savage, "Effects of Dispersion and Focusing on the Production of Optical Harmonics", Phys. Rev. Lett. **8**, 21 (1962) (Cited on page 21).

[27] J. A. Giordmaine, "Mixing of Light Beams in Crystals", Phys. Rev. Lett. **8**, 19 (1962) (Cited on page 21).

[28] J. A. Armstrong, N. Bloembergen, J. Ducuing, and P. S. Pershan, "Interactions between Light Waves in a Nonlinear Dielectric", Phys. Rev. **127**, 1918 (1962) (Cited on page 21).

[29] M. M. Fejer, G. A. Magel, D. H. Jundt, and R. L. Byer, "Quasi-Phase-Matched Second Harmonic Generation: Tuning and Tolerances", Ieee J. Quantum Elect. **28**, 2631 (1992) (Cited on page 21).

[30] D. B. Anderson and J. T. Boyd, "Wideband CO2 Laser Second Harmonic Generation Phase Matched in GaAs Thin-Film Waveguides", Appl. Phys. Lett. **19**, 266 (1971) (Cited on page 21).

[31] P. A. Cahill, K. D. Singer, and L. A. King, "Anomalous-Dispersion Phase-Matched Second-Harmonic Generation", Opt. Lett. **14**, 1137 (1989) (Cited on page 21).

[32] P. Dong, Y.-K. Chen, G.-H. Duan, and D. T. Neilson, "Silicon Photonic Devices and Integrated Circuits", P. Soc. Photo-opt. Ins. **3**, 215 (2014) (Cited on page 22).

[33] E. Yablonovitch, "Inhibited Spontaneous Emission in Solid-State Physics and Electronics", Phys. Rev. Lett. **58**, 2059 (1987) (Cited on page 23).

[34] S. John, "Strong Localization of Photons in Certain Disordered Dielectric Superlattices", Phys. Rev. Lett. **58**, 2486 (1987) (Cited on page 23).

[35] L. Rayleigh, "On the Maintenance of Vibrations by Forces of Double Frequency, and on the Propagation of Waves through a Medium Endowed with a Periodic Structure", Phil. Mag. S.5 **24**, 145 (1887) (Cited on page 23).

[36] D. W. Prather, A. Sharkawy, S. Shi, J. Murakowski, and G. Schneider, *Photonic Crystals, Theory, Applications and Fabrication*, 1st ed. (Wiley, Hoboken, N.J, 2009) (Cited on pages 23, 53, 56, 57, 108).

[37] V. Berger, "Nonlinear Photonic Crystals", Phys. Rev. Lett. **81**, 4136 (1998) (Cited on pages 23, 27, 28).

[38] E. Yablonovitch, T. J. Gmitter, R. D. Meade, A. M. Rappe, K. D. Brommer, and J. D. Joannopoulos, "Donor and Acceptor Modes in Photonic Band Structure", Phys. Rev. Lett. **67**, 3380 (1991) (Cited on page 26).

[39] T. Baba, N. Fukaya, and J. Yonekura, "Observation of Light Propagation in Photonic Crystal Optical Waveguides with Bends", Electron. Lett. **35**, 654 (1999) (Cited on pages 26, 28).

[40] C. J. M. Smith, H. Benisty, S. Olivier, M. Rattier, C. Weisbuch, T. F. Krauss, R. M. De La Rue, R. Houdré, and U. Oesterle, "Low-Loss Channel Waveguides with Two-Dimensional Photonic Crystal Boundaries", Appl. Phys. Lett. **77**, 2813 (2000) (Cited on page 26).

[41] M. Bertolotti, "Wave Interactions in Photonic Band Structures: An Overview", Journal of Optics A: Pure and Applied Optics **8**, S9 (2006) (Cited on page 27).

[42] N. Bloembergen and A. J. Sievers, "Nonlinear Optical Properties of Periodic Laminar Structures", Appl. Phys. Lett. **17**, 483 (1970) (Cited on page 27).

[43] M. Centini, C. Sibilia, M. Scalora, G. D'Aguanno, M. Bertolotti, M. J. Bloemer, C. M. Bowden, and I. Nefedov, "Dispersive Properties of Finite, One-Dimensional Photonic Band Gap Structures: Applications to Nonlinear Quadratic Interactions", Phys. Rev. E **60**, 4891 (1999) (Cited on page 27).

[44] Y. Dumeige, I. Sagnes, P. Monnier, P. Vidakovic, I. Abram, C. Mériadec, and A. Levenson, "Phase-Matched Frequency Doubling at Photonic Band Edges: Efficiency Scaling As the Fifth Power of the Length", Phys. Rev. Lett. **89**, 043901 (2002) (Cited on page 27).

[45] P. P. Markowicz, H. Tiryaki, H. Pudavar, P. N. Prasad, N. N. Lepeshkin, and R. W. Boyd, "Dramatic Enhancement of Third-Harmonic Generation in Three-Dimensional Photonic Crystals", Phys. Rev. Lett. **92**, 083903 (2004) (Cited on page 27).

[46] N. G. R. Broderick, G. W. Ross, H. L. Offerhaus, D. J. Richardson, and D. C. Hanna, "Hexagonally Poled Lithium Niobate: A Two-Dimensional Nonlinear Photonic Crystal", Phys. Rev. Lett. **84**, 4345 (2000) (Cited on page 28).

[47] S. Keren-Zur and T. Ellenbogen, "A New Dimension for Nonlinear Photonic Crystals", Nat. Photonics **12**, 575 (2018) (Cited on page 28).

[48] T. Xu, K. Switkowski, X. Chen, S. Liu, K. Koynov, H. Yu, H. Zhang, J. Wang, Y. Sheng, and W. Krolikowski, "Three-Dimensional Nonlinear Photonic Crystal in Ferroelectric Barium Calcium Titanate", Nat. Photonics **12**, 591 (2018) (Cited on page 28).

[49] D. Wei, C. Wang, H. Wang, X. Hu, D. Wei, X. Fang, Y. Zhang, D. Wu, Y. Hu, J. Li, S. Zhu, and M. Xiao, "Experimental Demonstration of a Three-Dimensional Lithium Niobate Nonlinear Photonic Crystal", Nat. Photonics **12**, 596 (2018) (Cited on page 28).

[50] T. F. Krauss, "Slow Light in Photonic Crystal Waveguides", J. Phys. D: Appl. Phys. **40**, 2666 (2007) (Cited on page 28).

[51] M. Soljačić, S. G. Johnson, S. Fan, M. Ibanescu, E. Ippen, and J. D. Joannopoulos, "Photonic-Crystal Slow-Light Enhancement of Nonlinear Phase Sensitivity", JOSA B **19**, 2052 (2002) (Cited on page 28).

[52] B. Corcoran, C. Monat, C. Grillet, D. J. Moss, B. J. Eggleton, T. P. White, L. O'Faolain, and T. F. Krauss, "Green Light Emission in Silicon through Slow-Light Enhanced Third-Harmonic Generation in Photonic-Crystal Waveguides", Nat. Photonics **3**, 206 (2009) (Cited on page 28).

[53] K. Rivoire, S. Buckley, F. Hatami, and J. Vučković, "Second Harmonic Generation in GaP Photonic Crystal Waveguides", Appl. Phys. Lett. **98**, 263113 (2011) (Cited on page 28).

[54] S. Hughes, L. Ramunno, J. F. Young, and J. E. Sipe, "Extrinsic Optical Scattering Loss in Photonic Crystal Waveguides: Role of Fabrication Disorder and Photon Group Velocity", Phys. Rev. Lett. **94**, 033903 (2005) (Cited on page 28).

[55] S. Fan and J. D. Joannopoulos, "Analysis of Guided Resonances in Photonic Crystal Slabs", Phys. Rev. B **65**, 235112 (2002) (Cited on pages 28, 35, 135).

[56] Y. Akahane, T. Asano, B.-S. Song, and S. Noda, "High-Q Photonic Nanocavity in a Two-Dimensional Photonic Crystal", Cah. Rev. The. **425**, 944 (2003) (Cited on page 28).

[57] K. Srinivasan, P. E. Barclay, O. Painter, J. Chen, A. Y. Cho, and C. Gmachl, "Experimental Demonstration of a High Quality Factor Photonic Crystal Microcavity", Appl. Phys. Lett. **83**, 1915 (2003) (Cited on page 28).

[58] T. V. Dolgova, A. I. Maidikovskii, M. G. Martem'yanov, G. Marovsky, G. Mattei, D. Schuhmacher, V. A. Yakovlev, A. A. Fedyanin, and O. A. Aktsipetrov, "Giant Second Harmonic Generation in Microcavities Based on Porous Silicon Photonic Crystals", J. Exp. Theor. Phys. Lett. **73**, 6 (2001) (Cited on page 29).

[59] M. Notomi, A. Shinya, S. Mitsugi, G. Kira, E. Kuramochi, and T. Tanabe, "Optical Bistable Switching Action of Si High-Q Photonic-Crystal Nanocavities", Opt. Express **13**, 2678 (2005) (Cited on page 29).

[60] M. W. McCutcheon, G. W. Rieger, J. F. Young, D. Dalacu, S. Frederick, P. J. Poole, G. C. Aers, and R. L. Williams, "Second Order Nonlinear Mixing of Two Modes in a Planar Photonic Crystal Microcavity", in Conference on Lasers and Electro-Optics (May 2006) (Cited on page 29).

[61] J. Bravo-Abad, A. Rodriguez, P. Bermel, S. G. Johnson, J. D. Joannopoulos, and M. Soljačić, "Enhanced Nonlinear Optics in Photonic-Crystal Microcavities", Opt. Express **15**, 16161 (2007) (Cited on page 29).

[62] L. C. Andreani, G. Guizzetti, M. Patrini, G. Vecchi, A. M. Malvezzi, L. Businaro, F. Romanato, E. D. Fabrizio, and A. Passaseo, "Resonant Second-Harmonic Generation and Mode Dispersion in Photonic Crystal Waveguides", Phys. Status Solidi B **238**, 428 (2003) (Cited on page 29).

[63] A. R. Cowan and J. F. Young, "Mode Matching for Second-Harmonic Generation in Photonic Crystal Waveguides", Phys. Rev. B **65**, 085106 (2002) (Cited on pages 29, 135).

[64] J. P. Mondia, H. M. v. Driel, W. Jiang, A. R. Cowan, and J. F. Young, "Enhanced Second-Harmonic Generation from Planar Photonic Crystals", Opt. Lett. **28**, 2500 (2003) (Cited on pages 29, 135).

[65] G. Vecchi, J. Torres, D. Coquillat, M. Le Vassor d'Yerville, and A. M. Malvezzi, "Enhancement of Visible Second-Harmonic Generation in Epitaxial GaN-Based Two-Dimensional Photonic Crystal Structures", Appl. Phys. Lett. **84**, 1245 (2004) (Cited on page 29).

[66] T. Tamir, *Guided-Wave Optoelectronics*, 2nd ed. (Springer Berlin Heidelberg, Berlin, 1990) (Cited on pages 30, 32).

[67] M. Kanskar, P. Paddon, V. Pacradouni, R. Morin, A. Busch, J. F. Young, S. R. Johnson, J. MacKenzie, and T. Tiedje, "Observation of Leaky Slab Modes in an Air-Bridged Semiconductor Waveguide with a Two-Dimensional Photonic Lattice", Appl. Phys. Lett. **70**, 1438 (1997) (Cited on page 35).

[68] C. M. Soukoulis and M. Wegener, "Past Achievements and Future Challenges in the Development of Three-Dimensional Photonic Metamaterials", Nat. Photonics **5**, 523 (2011) (Cited on pages 36, 37).

[69] W. Cai and V. Shalaev, *Optical Metamaterials: Fundamentals and Applications*, 1st ed. (Springer-Verlag, New York, 2010) (Cited on page 36).

[70] V. G. Veselago, "The Electrodynamics of Substances with Simultaneously Negative Values of E and M", Phys. Usp. **10**, 509 (1968) (Cited on page 36).

[71] D. R. Smith, W. J. Padilla, D. C. Vier, S. C. Nemat-Nasser, and S. Schultz, "Composite Medium with Simultaneously Negative Permeability and Permittivity", Phys. Rev. Lett. **84**, 4184 (2000) (Cited on page 36).

[72] J. B. Pendry, "Negative Refraction Makes a Perfect Lens", Phys. Rev. Lett. **85**, 3966 (2000) (Cited on page 36).

[73] E. Plum, V. A. Fedotov, A. S. Schwanecke, N. I. Zheludev, and Y. Chen, "Giant Optical Gyrotropy Due to Electromagnetic Coupling", Appl. Phys. Lett. **90**, 223113 (2007) (Cited on page 37).

[74] J. K. Gansel, M. Thiel, M. S. Rill, M. Decker, K. Bade, V. Saile, G. v. Freymann, S. Linden, and M. Wegener, "Gold Helix Photonic Metamaterial as Broadband Circular Polarizer", Science **325**, 1513 (2009) (Cited on page 37).

[75] J. Kaschke and M. Wegener, "Gold Triple-Helix Mid-Infrared Metamaterial by STED-Inspired Laser Lithography", Opt. Lett. **40**, 3986 (2015) (Cited on page 37).

[76] M. W. Klein, C. Enkrich, M. Wegener, and S. Linden, "Second-Harmonic Generation from Magnetic Metamaterials", Science **313**, 502 (2006) (Cited on pages 37, 38).

[77] A. Popov and V. Shalaev, "Negative-Index Metamaterials: Second-Harmonic Generation, Manley–Rowe Relations and Parametric Amplification", Appl. Phys. B **84**, 131 (2006) (Cited on page 37).

[78] J. B. Pendry, D. Schurig, and D. R. Smith, "Controlling Electromagnetic Fields", Science **312**, 1780 (2006) (Cited on page 37).

[79] D. Schurig, J. J. Mock, B. J. Justice, S. A. Cummer, J. B. Pendry, A. F. Starr, and D. R. Smith, "Metamaterial Electromagnetic Cloak at Microwave Frequencies", Science **314**, 977 (2006) (Cited on page 37).

[80] T. Ergin, N. Stenger, P. Brenner, J. B. Pendry, and M. Wegener, "Three-Dimensional Invisibility Cloak at Optical Wavelengths", Science, 1186351 (2010) (Cited on pages 37, 107).

[81] M. Kadic, T. Bückmann, R. Schittny, and M. Wegener, "Metamaterials beyond Electromagnetism", Rep. Prog. Phys. **76**, 126501 (2013) (Cited on page 37).

[82] R. Schittny, M. Kadic, S. Guenneau, and M. Wegener, "Experiments on Transformation Thermodynamics: Molding the Flow of Heat", Phys. Rev. Lett. **110**, 195901 (2013) (Cited on page 37).

[83] R. Schittny, M. Kadic, T. Bückmann, and M. Wegener, "Invisibility Cloaking in a Diffusive Light Scattering Medium", Science, 1254524 (2014) (Cited on page 37).

[84] T. A. Schaedler, A. J. Jacobsen, A. Torrents, A. E. Sorensen, J. Lian, J. R. Greer, L. Valdevit, and W. B. Carter, "Ultralight Metallic Microlattices", Science **334**, 962 (2011) (Cited on page 37).

[85] T. Bückmann, N. Stenger, M. Kadic, J. Kaschke, A. Frölich, T. Kennerknecht, C. Eberl, M. Thiel, and M. Wegener, "Tailored 3D Mechanical Metamaterials Made by Dip-in Direct-Laser-Writing Optical Lithography", Adv. Mater. **24**, 2710 (2012) (Cited on page 37).

[86] M. Kadic, T. Bückmann, N. Stenger, M. Thiel, and M. Wegener, "On the Practicability of Pentamode Mechanical Metamaterials", Appl. Phys. Lett. **100**, 191901 (2012) (Cited on page 37).

[87] T. Frenzel, M. Kadic, and M. Wegener, "Three-Dimensional Mechanical Metamaterials with a Twist", Science **358**, 1072 (2017) (Cited on page 37).

[88] J. Qu, M. Kadic, A. Naber, and M. Wegener, "Micro-Structured Two-Component 3D Metamaterials with Negative Thermal-Expansion Coefficient from Positive Constituents", Sci. Rep. **7**, 40643 (2017) (Cited on page 37).

[89] N. I. Zheludev, "The Road Ahead for Metamaterials", Science **328**, 582 (2010) (Cited on page 37).

[90] M. Lapine, I. V. Shadrivov, and Y. S. Kivshar, "Colloquium: Nonlinear Metamaterials", Rev. Mod. Phys. **86**, 1093 (2014) (Cited on page 38).

[91] I. V. Shadrivov, S. K. Morrison, and Y. S. Kivshar, "Tunable Split-Ring Resonators for Nonlinear Negative-Index Metamaterials", Opt. Express **14**, 9344 (2006) (Cited on page 38).

[92] F. B. P. Niesler, N. Feth, S. Linden, J. Niegemann, J. Gieseler, K. Busch, and M. Wegener, "Second-Harmonic Generation from Split-Ring Resonators on a GaAs Substrate", Opt. Lett. **34**, 1997 (2009) (Cited on pages 38, 39).

[93] A. A. Zharov, I. V. Shadrivov, and Y. S. Kivshar, "Nonlinear Properties of Left-Handed Metamaterials", Phys. Rev. Lett. **91**, 037401 (2003) (Cited on page 38).

[94] M. Lapine, I. V. Shadrivov, D. A. Powell, and Y. S. Kivshar, "Magnetoelastic Metamaterials", Nat. Mater. **11**, 30 (2012) (Cited on page 38).

[95] L. Alloatti, C. Kieninger, A. Froelich, M. Lauermann, T. Frenzel, K. Köhnle, W. Freude, J. Leuthold, M. Wegener, and C. Koos, "Second-Order Nonlinear Optical Metamaterials: ABC-Type Nanolaminates", Appl. Phys. Lett. **107**, 121903 (2015) (Cited on pages 38, 39, 67, 68, 70, 89, 105).

[96] H. Suchowski, K. O'Brien, Z. J. Wong, A. Salandrino, X. Yin, and X. Zhang, "Phase Mismatch–Free Nonlinear Propagation in Optical Zero-Index Materials", Science **342**, 1223 (2013) (Cited on page 38).

[97] A. Rose, D. Huang, and D. R. Smith, "Controlling the Second Harmonic in a Phase-Matched Negative-Index Metamaterial", Phys. Rev. Lett. **107**, 063902 (2011) (Cited on page 38).

[98] J. Lee, M. Tymchenko, C. Argyropoulos, P.-Y. Chen, F. Lu, F. Demmerle, G. Boehm, M.-C. Amann, A. Alù, and M. A. Belkin, "Giant Nonlinear Response from Plasmonic Metasurfaces Coupled to Intersubband Transitions", Cah. Rev. The. **511**, 65 (2014) (Cited on page 39).

[99] J. B. Khurgin and G. Sun, "Plasmonic Enhancement of the Third Order Nonlinear Optical Phenomena: Figures of Merit", Opt. Express **21**, 27460 (2013) (Cited on page 39).

[100] A. I. Kuznetsov, A. E. Miroshnichenko, M. L. Brongersma, Y. S. Kivshar, and B. Luk'yanchuk, "Optically Resonant Dielectric Nanostructures", Science **354**, aag2472 (2016) (Cited on page 39).

[101] S. Clemmen, A. Hermans, E. Solano, J. Dendooven, K. Koskinen, M. Kauranen, E. Brainis, C. Detavernier, and R. Baets, "Atomic Layer Deposited Second Order Nonlinear Optical Metamaterial for Back-End Integration with CMOS-Compatible Nanophotonic Circuitry", arXiv, 1508.05275 (2015) (Cited on pages 39, 89, 105).

[102] A. Hermans, C. Kieninger, K. Koskinen, A. Wickberg, E. Solano, J. Dendooven, M. Kauranen, S. Clemmen, M. Wegener, C. Koos, and R. Baets, "On the Determination of $\chi^{(2)}$ in Thin Films: A Comparison of One-Beam Second-Harmonic Generation Measurement Methodologies", Sci. Rep. **7**, 44581 (2017) (Cited on pages 41, 66).

[103] S. M. George, "Atomic Layer Deposition: An Overview", Chem. Rev. **110**, 111 (2010) (Cited on pages 44, 46, 95).

[104] R. W. Johnson, A. Hultqvist, and S. F. Bent, "A Brief Review of Atomic Layer Deposition: From Fundamentals to Applications", Mater. Today **17**, 236 (2014) (Cited on page 44).

[105] T. Tynell and M. Karppinen, "Atomic Layer Deposition of ZnO: A Review", Semicond. Sci. Technol. **29**, 043001 (2014) (Cited on pages 45, 89, 105, 106).

[106] D. M. King, X. Liang, C. S. Carney, L. F. Hakim, P. Li, and A. W. Weimer, "Atomic Layer Deposition of UV-Absorbing ZnO Films on SiO2 and TiO2 Nanoparticles Using a Fluidized Bed Reactor", Adv. Funct. Mater. **18**, 607 (2008) (Cited on page 45).

[107] S.-Y. Pung, K.-L. Choy, X. Hou, and C. Shan, "Preferential Growth of ZnO Thin Films by the Atomic Layer Deposition Technique", Acs. Sym. Ser. **19**, 435609 (2008) (Cited on pages 45, 90).

[108] J. Malm, E. Sahramo, J. Perälä, T. Sajavaara, and M. Karppinen, "Low-Temperature Atomic Layer Deposition of ZnO Thin Films: Control of Crystallinity and Orientation", Thin Solid Films **519**, 5319 (2011) (Cited on page 45).

[109] N. Y. Yuan, S. Y. Wang, C. B. Tan, X. Q. Wang, G. G. Chen, and J. N. Ding, "The Influence of Deposition Temperature on Growth Mode, Optical and Mechanical Properties of ZnO Films Prepared by the ALD Method", J. Cryst. Growth **366**, 43 (2013) (Cited on page 45).

[110] K.-M. Kang and H.-H. Park, "Effect of Atomic Layer Deposition Temperature on the Growth Orientation, Morphology, and Electrical, Optical, and Band-Structural Properties of ZnO and Fluorine-Doped ZnO Thin Films", J. Phys. Chem. C **122**, 377 (2018) (Cited on page 45).

[111] S. Kwon, S. Bang, S. Lee, S. Jeon, W. Jeong, H. Kim, S. C. Gong, H. J. Chang, H.-h. Park, and H. Jeon, "Characteristics of the ZnO Thin Film Transistor by Atomic Layer Deposition at Various Temperatures", Semicond. Sci. Tech. **24**, 035015 (2009) (Cited on page 45).

[112] T. Weckman and K. Laasonen, "Atomic Layer Deposition of Zinc Oxide: Diethyl Zinc Reactions and Surface Saturation from First-Principles", J. Phys. Chem. C **120**, 21460 (2016) (Cited on page 46).

[113] S. Jakschik, U. Schroeder, T. Hecht, M. Gutsche, H. Seidl, and J. W. Bartha, "Crystallization Behavior of Thin ALD-Al2O3 Films", Thin Solid Films **425**, 216 (2003) (Cited on page 46).

[114] A. C. Dillon, A. W. Ott, J. D. Way, and S. M. George, "Surface Chemistry of Al2O3 Deposition Using Al(CH3)3 and H2O in a Binary Reaction Sequence", Surf. Sci. **322**, 230 (1995) (Cited on page 46).

[115] R. L. Puurunen, "Random Deposition as a Growth Mode in Atomic Layer Deposition", Chem. Vapor Depos. **10**, 159 (2004) (Cited on page 49).

[116] H. C. Guo, E. Ye, Z. Li, M.-Y. Han, and X. J. Loh, "Recent Progress of Atomic Layer Deposition on Polymeric Materials", Mater. Sci. Eng. C., Recent Advances in Biomedical Materials **70**, 1182 (2017) (Cited on page 49).

[117] Z. Baji, Z. Lábadi, Z. E. Horváth, G. Molnár, J. Volk, I. Bársony, and P. Barna, "Nucleation and Growth Modes of ALD ZnO", Crystal Growth & Design **12**, 5615 (2012) (Cited on pages 49, 94).

[118] C. A. Wilson, R. K. Grubbs, and S. M. George, "Nucleation and Growth during Al2O3 Atomic Layer Deposition on Polymers", Chem. Mater. **17**, 5625 (2005) (Cited on page 49).

[119] A. Blanco, E. Chomski, S. Grabtchak, M. Ibisate, S. John, S. W. Leonard, C. Lopez, F. Meseguer, H. Miguez, J. P. Mondia, G. A. Ozin, O. Toader, and H. M. van Driel, "Large-Scale Synthesis of a Silicon Photonic Crystal with a Complete Three-Dimensional Bandgap near 1.5 Micrometres", Cah. Rev. The. **405**, 437 (2000) (Cited on page 54).

[120] A. Chelnokov, K. Wang, S. Rowson, P. Garoche, and J.-M. Lourtioz, "Near-Infrared Yablonovite-Like Photonic Crystals by Focused-Ion-Beam Etching of Macroporous Silicon", Appl. Phys. Lett. **77**, 2943 (2000) (Cited on page 54).

[121] S. Y. Lin, J. G. Fleming, D. L. Hetherington, B. K. Smith, R. Biswas, K. M. Ho, M. M. Sigalas, W. Zubrzycki, S. R. Kurtz, and J. Bur, "A Three-Dimensional Photonic Crystal Operating at Infrared Wavelengths", Cah. Rev. The. **394**, 251 (1998) (Cited on page 54).

[122] S. Noda, K. Tomoda, N. Yamamoto, and A. Chutinan, "Full Three-Dimensional Photonic Bandgap Crystals at Near-Infrared Wavelengths", Science **289**, 604 (2000) (Cited on page 54).

[123] S. Maruo, O. Nakamura, and S. Kawata, "Three-Dimensional Microfabrication with Two-Photon-Absorbed Photopolymerization", Opt. Lett. **22**, 132 (1997) (Cited on page 54).

[124] H.-B. Sun, S. Matsuo, and H. Misawa, "Three-Dimensional Photonic Crystal Structures Achieved with Two-Photon-Absorption Photopolymerization of Resin", Appl. Phys. Lett. **74**, 786 (1999) (Cited on page 54).

[125] M. Deubel, G. von Freymann, M. Wegener, S. Pereira, K. Busch, and C. M. Soukoulis, "Direct Laser Writing of Three-Dimensional Photonic-Crystal Templates for Telecommunications", Nat. Mater. **3**, 444 (2004) (Cited on pages 54, 107).

[126] J. Fischer and M. Wegener, "Three-Dimensional Direct Laser Writing Inspired by Stimulated-Emission-Depletion Microscopy", Opt. Mater. Express **1**, 614 (2011) (Cited on pages 54, 58, 80, 108).

[127] A. Frölich, J. Fischer, T. Zebrowski, K. Busch, and M. Wegener, "Titania Woodpiles with Complete Three-Dimensional Photonic Bandgaps in the Visible", Adv. Mater. **25**, 3588 (2013) (Cited on pages 54, 136).

[128] K.-S. Lee, D.-Y. Yang, S. H. Park, and R. H. Kim, "Recent Developments in the Use of Two-Photon Polymerization in Precise 2D and 3D Microfabrications", Polym. Advan. Technol. **17**, 72 (2006) (Cited on page 55).

[129] M. P. Stevens, *Polymer Chemistry: An Introduction*, 3rd ed. (Oxford University Press, New York, 1998) (Cited on page 55).

[130] S. Maruo and K. Ikuta, "Three-Dimensional Microfabrication by Use of Single-Photon-Absorbed Polymerization", Appl. Phys. Lett. **76**, 2656 (2000) (Cited on page 57).

[131] T. J. A. Wolf, J. Fischer, M. Wegener, and A.-N. Unterreiner, "Pump–Probe Spectroscopy on Photoinitiators for Stimulated-Emission-Depletion Optical Lithography", Opt. Lett. **36**, 3188 (2011) (Cited on page 57).

[132] Q. Shi, B. Sontheimer, N. Nikolay, A. W. Schell, J. Fischer, A. Naber, O. Benson, and M. Wegener, "Wiring Up Pre-Characterized Single-Photon Emitters by Laser Lithography", Sci. Rep. **6**, 31135 (2016) (Cited on page 57).

[133] M. D'Alagni, P. D. Santis, A. M. Liquori, and M. Savino, "A Comparison between the Far Ultraviolet Absorption Spectra of Isotactic and Syndiotactic Polymethyl Methacrylate in Solution", J. Polym. Sci. B **2**, 925 (1964) (Cited on page 57).

[134] W. Knolle, T. Scherzer, S. Naumov, and R. Mehnert, "Direct (222nm) Photopolymerisation of Acrylates. A Laser Flash Photolysis and Quantum Chemical Study", Radiat. Phys. Chem., 10th Tihany Symposium on Radiation Chemistry **67**, 341 (2003) (Cited on page 58).

[135] T. Scherzer, "Photopolymerization of Acrylates without Photoinitiators with Short-Wavelength UV Radiation: A Study with Real-Time Fourier Transform Infrared Spectroscopy", J. Polym. Sci., Part A: Polym. Chem. **42**, 894 (2004) (Cited on page 58).

[136] P. Mueller, M. Thiel, and M. Wegener, "3D Direct Laser Writing Using a 405 nm Diode Laser", Opt. Lett. **39**, 6847 (2014) (Cited on page 58).

[137] J. Fischer and M. Wegener, "Three-Dimensional Optical Laser Lithography beyond the Diffraction Limit: 3D Optical Lithography off Limits", Laser Photonics Rev. **7**, 22 (2013) (Cited on pages 58, 59).

[138] J. Fischer, "Three-Dimensional Optical Lithography beyond the Diffraction Limit", PhD thesis (KIT, 2012) (Cited on page 60).

[139] W. N. Herman and L. M. Hayden, "Maker Fringes Revisited: Second-Harmonic Generation from Birefringent or Absorbing Materials", J. Opt. Soc. Am. B **12**, 416 (1995) (Cited on pages 68, 71, 103).

[140] J. A. Giordmaine, "Nonlinear Optical Properties of Liquids", Phys. Rev. **138**, A1599 (1965) (Cited on page 70).

[141] V. G. Dmitriev, G. G. Gurzadian, and D. N. Nikogosian, *Handbook of Nonlinear Optical Crystals*, 3rd ed. (Springer, 1999) (Cited on pages 71, 105).

[142] C. Kittel, *Introduction to Solid State Physics*, 8th ed. (Wiley John + Sons, Hoboken, NJ, 2004) (Cited on page 76).

[143] M. Birkholz, *Thin Film Analysis by X-Ray Scattering*, 1st ed. (Wiley-VCH, Weinheim, 2005) (Cited on page 77).

[144] P. Scherrer, "Bestimmung der Größe und der inneren Struktur von Kolloidteilchen mittels Röntgenstrahlen", Nachrichten von der Gesellschaft der Wissenschaften zu Göttingen, Mathematisch-Physikalische Klasse **1918**, 99 (1918) (Cited on page 78).

[145] R. Jenkins, *Introduction to X-Ray Powder Diffractometry*, 1st ed. (Wiley, 2012) (Cited on page 78).

[146] A. Polycarpou, *Introduction to the Finite Element Method in Electromagnetics* (Morgan and Claypool Publishers, San Rafael, CA, 2006) (Cited on page 79).

[147] T. Gissibl, S. Wagner, J. Sykora, M. Schmid, and H. Giessen, "Refractive Index Measurements of Photo-Resists for Three-Dimensional Direct Laser Writing", Opt. Mater. Express **7**, 2293 (2017) (Cited on page 81).

[148] A. Wickberg, C. Kieninger, C. Sürgers, S. Schlabach, X. Mu, C. Koos, and M. Wegener, "Second-Harmonic Generation from ZnO/Al2O3 Nanolaminate Optical Metamaterials Grown by Atomic-Layer Deposition", Adv. Opt. Mater. **4**, 1203 (2016) (Cited on pages 88, 89, 94, 96, 101, 104).

[149] M. C. Larciprete and M. Centini, "Second Harmonic Generation from ZnO Films and Nanostructures", Appl. Phys. Rev. **2**, 031302 (2015) (Cited on page 88).

[150] Ü. Özgür, Y. I. Alivov, C. Liu, A. Teke, M. A. Reshchikov, S. Doğan, V. Avrutin, S.-J. Cho, and H. Morkoç, "A Comprehensive Review of ZnO Materials and Devices", J. Appl. Phys. **98**, 041301 (2005) (Cited on page 88).

[151] A. F. Kohan, G. Ceder, D. Morgan, and C. G. Van de Walle, "First-Principles Study of Native Point Defects in ZnO", Phys. Rev. B **61**, 15019 (2000) (Cited on page 88).

[152] G. Wang, G. K. L. Wong, and J. B. Ketterson, "Redetermination of Second-Order Susceptibility of Zinc Oxide Single Crystals", Appl. Opt. **40**, 5436 (2001) (Cited on page 88).

[153] M. C. Larciprete, D. Passeri, F. Michelotti, S. Paoloni, C. Sibilia, M. Bertolotti, A. Belardini, F. Sarto, F. Somma, and S. L. Mastro, "Second Order Nonlinear Optical Properties of Zinc Oxide Films Deposited by Low Temperature Dual Ion Beam Sputtering", J. Appl. Phys. **97**, 023501 (2005) (Cited on page 88).

[154] H. Cao, J. Y. Wu, H. C. Ong, J. Y. Dai, and R. P. H. Chang, "Second Harmonic Generation in Laser Ablated Zinc Oxide Thin Films", Appl. Phys. Lett. **73**, 572 (1998) (Cited on pages 88, 90).

[155] J. Ebothé, R. Miedzinski, V. Kapustianyk, B. Turko, B. Kulyk, W. Gruhn, and I. V. Kityk, "Optical SHG for ZnO Films with Different Morphology Stimulated by UV-Laser Thermotreatment", J. Phys. Conf. Ser. **79**, 012001 (2007) (Cited on page 88).

[156] U. Griebner, R. A. Kaindl, T. Elsaesser, and W. Seeber, "Frequency Doubling and Autocorrelation Studies of 20-fs Pulses Using Polycrystalline Zinc Oxide Thin Films", Appl. Phys. B **67**, 757 (1998) (Cited on page 88).

[157] C. Y. Liu, B. P. Zhang, N. T. Binh, and Y. Segawa, "Second Harmonic Generation in ZnO Thin Films Fabricated by Metalorganic Chemical Vapor Deposition", Opt. Commun. **237**, 65 (2004) (Cited on page 88).

[158] S. W. Liu, J. L. Weerasinghe, J. Liu, J. Weaver, C. L. Chen, W. Donner, and M. Xiao, "Reflective Second Harmonic Generation near Resonance in the Epitaxial Al-Doped ZnO Thin Film", Opt. Express **15**, 10666 (2007) (Cited on pages 88, 90).

[159] U. Neumann, R. Grunwald, U. Griebner, G. Steinmeyer, and W. Seeber, "Second-Harmonic Efficiency of ZnO Nanolayers", Appl. Phys. Lett. **84**, 170 (2004) (Cited on page 88).

[160] U. Neumann, R. Grunwald, U. Griebner, G. Steinmeyer, M. Schmidbauer, and W. Seeber, "Second-Harmonic Performance of a-Axis-Oriented ZnO Nanolayers on Sapphire Substrates", Appl. Phys. Lett. **87**, 171108 (2005) (Cited on pages 88, 90).

[161] G. Wang, G. T. Kiehne, G. K. L. Wong, J. B. Ketterson, X. Liu, and R. P. H. Chang, "Large Second Harmonic Response in ZnO Thin Films", Appl. Phys. Lett. **80**, 401 (2002) (Cited on pages 88, 90, 102).

[162] X. Q. Zhang, Z. K. Tang, M. Kawasaki, A. Ohtomo, and H. Koinuma, "Resonant Exciton Second-Harmonic Generation in Self-Assembled ZnO Microcrystallite Thin Films", J. Phys.: Condens. Matter **15**, 5191 (2003) (Cited on page 88).

[163] X. Q. Zhang, Z. K. Tang, M. Kawasaki, A. Ohtomo, and H. Koinuma, "Second Harmonic Generation in Self-Assembled ZnO Microcrystallite Thin Films", Thin Solid Films **450**, 320 (2004) (Cited on pages 88, 90, 102).

[164] H. Mohseni and T. W. Scharf, "Atomic Layer Deposition of ZnO/Al2O3/ZrO2 Nanolaminates for Improved Thermal and Wear Resistance in Carbon-Carbon Composites", J. Vac. Sci. Technol. A **30**, 01A149 (2012) (Cited on pages 90, 91).

[165] D. M. Hausmann and R. G. Gordon, "Surface Morphology and Crystallinity Control in the Atomic Layer Deposition (ALD) of Hafnium and Zirconium Oxide Thin Films", J. Cryst. Growth **249**, 251 (2003) (Cited on pages 91, 100).

[166] A. A. Chaaya, R. Viter, I. Baleviciute, M. Bechelany, A. Ramanavicius, Z. Gertnere, D. Erts, V. Smyntyna, and P. Miele, "Tuning Optical Properties of Al2O3/ZnO Nanolaminates Synthesized by Atomic Layer Deposition", J. Phys. Chem. C **118**, 3811 (2014) (Cited on page 91).

[167] L. Karvonen, A. Säynätjoki, Y. Chen, H. Jussila, J. Rönn, M. Ruoho, T. Alasaarela, S. Kujala, R. A. Norwood, N. Peyghambarian, K. Kieu, and S. Honkanen, "Enhancement of the Third-Order Optical Nonlinearity in ZnO/Al2O3 Nanolaminates Fabricated by Atomic Layer Deposition", Appl. Phys. Lett. **103**, 031903 (2013) (Cited on page 91).

[168] J. D. Dana, E. S. Dana, C. Palache, H. Berman, and C. Frondel, *Dana's System of Mineralogy, Vol. I: Elements, Sulfides, Sulfosalts, Oxides*, 7th ed. (Wiley, New York; London, 1944) (Cited on page 96).

[169] A. Hermans, A. Hermans, M. V. Daele, C. Kieninger, C. Kieninger, J. Dendooven, S. Clemmen, S. Clemmen, C. Detavernier, C. Koos, C. Koos, R. Baets, and R. Baets, "CMOS-Compatible ALD Zinc Oxide Coating for On-Chip Second-Order Nonlinear Optical Functionalities", in Conference on Lasers and Electro-Optics (May 2017) (Cited on page 105).

[170] A. Frölich and M. Wegener, "Spectroscopic Characterization of Highly Doped ZnO Films Grown by Atomic-Layer Deposition for Three-Dimensional Infrared Metamaterials [Invited]", Opt. Mater. Express **1**, 883 (2011) (Cited on page 105).

[171] S. Keun Kim, C. Seong Hwang, S.-H. Ko Park, and S. Jin Yun, "Comparison between ZnO Films Grown by Atomic Layer Deposition Using H2O or O3 As Oxidant", Thin Solid Films **478**, 103 (2005) (Cited on page 105).

[172] J. Fischer, T. Ergin, and M. Wegener, "Three-Dimensional Polarization-Independent Visible-Frequency Carpet Invisibility Cloak", Opt. Lett. **36**, 2059 (2011) (Cited on page 107).

[173] M. F. Schumann, S. Wiesendanger, J. C. Goldschmidt, B. Bläsi, K. Bittkau, U. W. Paetzold, A. Sprafke, R. B. Wehrspohn, C. Rockstuhl, and M. Wegener, "Cloaked Contact Grids on Solar Cells by Coordinate Transformations: Designs and Prototypes", Optica **2**, 850 (2015) (Cited on page 107).

[174] K. M. Ho, C. T. Chan, C. M. Soukoulis, R. Biswas, and M. Sigalas, "Photonic Band Gaps in Three Dimensions: New Layer-by-Layer Periodic Structures", Solid State Commun. **89**, 413 (1994) (Cited on page 108).

[175] Y. Lin and P. R. Herman, "Effect of Structural Variation on the Photonic Band Gap in Woodpile Photonic Crystal with Body-Centered-Cubic Symmetry", J. Appl. Phys. **98**, 063104 (2005) (Cited on page 108).

[176] A. Wickberg, A. Abass, H.-H. Hsiao, C. Rockstuhl, and M. Wegener, "Second-Harmonic Generation by 3D Laminate Metacrystals", unpublished, 2019 (Cited on pages 110, 111, 116, 119, 123, 126, 127, 129, 130, 133, 134).

[177] M. F. Limonov, M. V. Rybin, A. N. Poddubny, and Y. S. Kivshar, "Fano Resonances in Photonics", Nat. Photonics **11**, 543 (2017) (Cited on page 130).

Acknowledgments

At this point, it is my pleasure to thank all the people that contributed in one way or the other and, thereby, made this thesis possible. I want to thank Prof. Dr. Martin Wegener for the great opportunity to work in his group and for the outstanding supervision. Through his guidance he managed to steer my focus to the essentials and, at the same time, gave me the space necessary to develop my own ideas. Furthermore, I am thankful to my second reviewer Prof. Dr. Carsten Rockstuhl both for his contributions in our collaborations and for taking the time to review this thesis.

During my work I had the pleasure to learn a lot from and with my collaborators Clemens Kieninger, Dr. Aimi Abass, and Prof. Dr. Hui-Hsin Hsiao. The successful realization of our projects was made possible through the mutual effort and many fruitful discussions. Also, I want to thank Florian Graf, Johannes Fischer and Martin Krämer whom I could supervise in the scope of their student theses. I have learned a lot both professionally and personally during this time.

Work was always more fun when surrounded by my colleagues. I would like to thank all former and present members of the Wegener group. For the countless hours we have spent together both at work and in our free time, for the inspiring and also inspired scientific and non-scientific discussions, and for their constant willingness to help each other out. In particular, I am very grateful to Christian Kern with whom I spent a lot of time working on the atomic-layer deposition system. Difficulties always seemed way easier to solve with him. Special thanks also go to Dr. Tiemo Bückmann, Dr. Johannes Kaschke, Dr. Jonathan Müller, and Dr. Benjamin Richter. They have always been there with their advice and became more than just colleagues.

Keeping a focus on the research was made possible by the support of many people working in the background. I thank Johann Westhauser for his technical assistance, Michael Hippe, Helmuth Lay, and Werner Gilde for

their advice and manpower when it came to computer-related or electrical challenges, and Claudia Alaya, Ursula Mösle, and Monica Brenkmann for their administrative support.
Furthermore, I owe thanks to Dr. Aimi Abass, Tobias Frenzel, Vincent Hahn, Julia Haug, Clemens Kieninger, Julian Köpfler, Frederik Mayer, Patrick Müller, Alexander Münchinger, Dr. Benedikt Prunsche, Dr. Jingyuan Qu, and Heiner Zwickel for proof-reading and their critical questions.
Finally, I would like to thank my family. My parents who have invested a lot to make sure I could go my way and my siblings Natalie, Michael, and Alex. Things are way easier with people that always support you.